

APPLICATIONS OF FWM AND XPM INDUCED BY GROUND-STATE COHERENCE IN THERMAL ATOMIC VAPOR

By

SUSHREE SUBHADARSHINEE SAHOO
PHYS11201304013

National Institute of Science Education and Research
Bhubaneswar

A thesis submitted to the
Board of Studies in Physical Sciences
In partial fulfillment of requirements
For the Degree of

DOCTOR OF PHILOSOPHY
of
HOMI BHABHA NATIONAL INSTITUTE

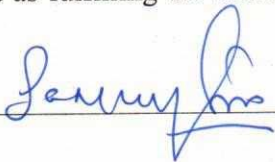


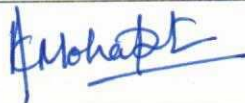
July, 2019

Homi Bhabha National Institute

Recommendations of the Viva Voce Committee

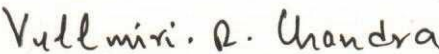
As members of the Viva Voce Committee, we certify that we have read the dissertation prepared by Sushree Subhadarshinee Sahoo entitled "Applications of FWM and XPM induced by ground state coherence in thermal atomic vapor" and recommend that it may be accepted as fulfilling the thesis requirement for the award of Degree of Doctor of Philosophy.

Chairman – Dr. Sanjay Swain  Date: 14/11/2019

Guide / Convener – Dr. Ashok K. Mohapatra  Date: 14/11/2019

Co-guide - Date:

Examiner – Dr. Umakant Rapol  Date: 14-Nov-2019

Member 1- Dr. V. Ravi Chandra  Date: 14-11-2019

Member 2- Dr. Himansu S. Biswal  Date: 14-11-2019

Final approval and acceptance of this thesis is contingent upon the candidate's submission of the final copies of the thesis to HBNI.

I/We hereby certify that I/we have read this thesis prepared under my/our direction and recommend that it may be accepted as fulfilling the thesis requirement.

Date: 14/11/2019

Place: Jatani


Dr. Ashok K Mohapatra
(Thesis supervisor)

STATEMENT BY AUTHOR

This dissertation has been submitted in partial fulfillment of requirements for an advanced degree at Homi Bhabha National Institute (HBNI) and is deposited in the Library to be made available to borrowers under rules of the HBNI.

Brief quotations from this dissertation are allowable without special permission, provided that accurate acknowledgment of source is made. Requests for permission for extended quotation from or reproduction of this manuscript in whole or in part may be granted by the Competent Authority of HBNI when in his or her judgment the proposed use of the material is in the interests of scholarship. In all other instances, however, permission must be obtained from the author.

Sushree Subhadarshinee Sahoo

(Sushree Subhadarshinee Sahoo)

DECLARATION

I, hereby declare that the investigation presented in the thesis has been carried out by me. The work is original and has not been submitted earlier as a whole or in part for a degree/diploma at this or any other Institution/University.

Sushree Subhadarshinee Sahoo

(Sushree Subhadarshinee Sahoo)

List of Publications arising from the thesis

Journal

1. "Mirrorless optical parametric oscillator inside an all-optical waveguide", S. S. Sahoo, S. S. Pati and A. K. Mohapatra, *Phy. Rev. A*, **2018**, 98, 063838.
2. "Polarization rotation of light propagating through a medium with efficient four wave mixing and cross phase modulation", S. S. Sahoo, A. Bhowmick and A. K. Mohapatra, *J. Phys. B: At. Mol. Opt. Phys.*, **2017**, 50, 055501.
3. "Study of dynamical phase transition in the threshold of mirrorless optical parametric oscillator", S. S. Sahoo, S. S. Nayak, S. R. Mishra and A. K. Mohapatra (Manuscript under preparation)

Chapters in Books

1. "Mirrorless laser inside an all-optical waveguide" accepted for "KIRAN: A bulletin of Indian Laser Association.

Conferences

1. Invited talk in Topical Advances in Photonics (TMAP-2019) (March 29th - 30th 2019), NISER India.
2. Invited talk in Frontier in light-matter interaction (FiLMI-2016) (March 4th - 5th 2016), IIT Ropar, India.
3. Poster presentation in Recent Trends in Cold and Ultracold Matter (March 27th - 29th, 2018), IIT Guwahati, India.
4. Poster presentation in Annual Condensed Matter Physics Meet (Feb 26th -27th, 2018), NISER, Jatni, India.
5. Poster presentation in National Laser Symposium (NLS-26) (Dec 20th -23rd, 2017), BARC, Mumbai, India.
6. Poster presentation in International Workshop on Complex Photonics, (Jan 22-24, 2017), TIFR Mumbai, India.

7. Poster presentation in Annual Condensed Matter Physics Meet (Feb 26th -27th, 2018), NISER, Jatni, India.
8. Poster presentation in Recent Trends in Cold and Ultracold Matter (March 27th - 29th, 2018), IIT Guwahati, India.

Sushree Subhadarshinee Sahoo

(Sushree Subhadarshinee Sahoo)

DEDICATIONS

I whole-heartedly dedicate this thesis to my beloved parents, **Mrs. Kamalinee Sahoo** and **Mr. Subash Chandra Sahoo**.

I dedicate this thesis also to all the teachers in my life, who have helped and inspired me to come this far.

ACKNOWLEDGEMENTS

First, I express my sincere gratitude to my research supervisor, Dr. Ashok K. Mohapatra for his continual encouragement and support throughout my Ph.D. life. I can not thank him enough for everything he has done for the betterment of my research and my academic development. I acknowledge his relentless effort, guidance, and advice, which are inevitable for the completion of this thesis. I shall remain ever grateful to him.

I extend my gratitude to my thesis monitoring committee members, Dr. Sanjay K. Swain, Dr. Ritwick Das, Dr. V. Ravi Chandra and Dr. Himanshu S. Biswal for their insightful suggestions in my research work. I am grateful to Prof. C. S. Unnikrishnan for providing me the lab facility at TIFR, Mumbai and for his support and useful discussions for the development of the photon counting module. I am thankful to Mr. P. V. Sudershanan and Mr. S. Pereira, the scientific officers at TIFR for their immense help in building the photon counting module. My sincere thanks go to Dr. T. N. Dey from IIT Guwahati his input in the theoretical models related to my thesis work. I am thankful to Dr. A. K. Nandy and Ms. Sabana From NISER and Ninad from TIFR for many useful discussions. I am grateful to all the faculty and staff members of NISER for their direct or indirect contribution to my thesis. I wish to acknowledge the Department of Atomic Energy, Govt. of India for the financial support for this research.

I am grateful to my present and former lab members Arup, Dushmant, Snigdha, Akshaya, Tanim, Soumya, Sujit, Satya and Ananya who have always extended their help whenever I needed and have maintained a friendly atmosphere in the lab. I especially thank Snigdha for her contribution in performing the experiments and data analysis. I whole-heartedly thank Dushmant for his constant support, humor and the delicious cooked food on many occasions. I am thankful to my seniors Kishore da, Mukesh, Avanendra and Vantari for their valuable advice and help in the time of need. I am grateful to Rita didi for accompanying me to the Odissi classes and thus inspiring me to rejuvenate an old hobby. I would like to thank my friends Mony, Debadeepti, Subrata, Vipul and Sagarika for their help and support. I am thankful to my MSc friends Rashmi, Anindita, Rupa, Sumitra and Abha for hearing me out with patience and for all the fun we had together.

I am thankful to my elder sister Mrs. Manjushree Sahoo and brother-in-law Dr. Brundaban Sahu for their unfailing support and constant encouragement. I wish to thank my younger brothers Uttam, Pritam and my nephew Krishu for their affection. And finally, but not the least I would like to thank Antarjami for his unceasing love and care!

CONTENTS

| | |
|--|-----------|
| SUMMARY | xi |
| LIST OF FIGURES | xii |
| LIST OF TABLES | xviii |
| 1 Introduction | 1 |
| 1.1 Introduction to the ground state coherence | 2 |
| 1.2 A review on enhanced XPM due to ground state coherence | 5 |
| 1.3 A review on enhanced FWM due to ground state coherence | 6 |
| 1.4 Thesis objective | 7 |
| 1.5 Thesis organization | 8 |
| 2 Basic theoretical and experimental tools | 15 |
| 2.1 Basics of nonlinear optical effects | 15 |
| 2.1.1 Tensor nature of $\chi^{(3)}$ | 16 |
| 2.1.2 Self-phase modulation | 16 |
| 2.1.3 Cross-phase modulation | 17 |
| 2.1.4 Four-wave mixing | 18 |
| 2.2 Wave equation for Nonlinear medium | 19 |
| 2.3 Transverse modes of light | 20 |
| 2.3.1 Gaussian mode | 21 |
| 2.3.2 Hermite-Gaussian modes | 21 |
| 2.3.3 Laguerre-Gaussian modes | 22 |
| 2.4 Semiclassical model of basic atom-light interaction (Two-level system) | 23 |
| 2.4.1 Rotating frame transformation | 24 |
| 2.4.2 Dressed states picture and Light shift | 25 |
| 2.4.3 Effect of Relaxation processes | 26 |

| | | |
|----------|--|-----------|
| 2.4.4 | The optical Bloch equations | 27 |
| 2.4.5 | Doppler broadening | 28 |
| 2.5 | Properties of rubidium | 29 |
| 2.5.1 | Zeeman effect on hyperfine states | 31 |
| 2.6 | Lasers | 32 |
| 2.7 | Saturated absorption spectroscopy | 32 |
| 2.8 | 4-f imaging technique | 35 |
| 3 | Polarization rotation of light with efficient FWM and XPM in thermal atomic vapor | 38 |
| 3.1 | Observation of FWM and XPM in rubidium thermal vapor | 39 |
| 3.1.1 | Experimental setup | 40 |
| 3.1.2 | Experimental Results and Discussion | 41 |
| 3.2 | Principle of Polarization rotation of light | 46 |
| 3.3 | Theoretical model: Probe propagation equations | 48 |
| 3.4 | Experimental setup | 54 |
| 3.4.1 | Experimental Results | 56 |
| 3.4.2 | Estimation of nonlinear susceptibilities of the medium | 58 |
| 3.5 | Conclusion | 60 |
| 4 | Mirrorless optical parametric oscillator inside an all-optical waveguide | 63 |
| 4.1 | Principle of FWM-based MOPO | 64 |
| 4.2 | Experimental details | 65 |
| 4.3 | Preliminary experimental results | 66 |
| 4.4 | Theoretical model | 69 |
| 4.4.1 | XPM of the generated fields due to the pump and the control fields | 69 |
| 4.4.2 | Experimental verification of the model | 72 |
| 4.4.3 | Wave-equations for the generated fields | 74 |
| 4.4.4 | Observation of spatial modes of the generated fields in the single-mode regime of MOPO | 78 |
| 4.4.5 | Multimode regime of MOPO | 84 |
| 4.4.6 | Observation of higher order spatial modes | 85 |
| 4.5 | Conclusion | 86 |

| | | |
|----------|---|------------|
| 5 | MOPO-based optical bistability | 90 |
| 5.1 | Principle of MOPO-based optical bistability | 91 |
| 5.1.1 | Threshold condition for MOPO using plane-wave approximation | 91 |
| 5.1.2 | Effect of Gaussian nature of the beams | 93 |
| 5.2 | Experimental arrangement | 96 |
| 5.3 | Experimental observation of the optical bistability | 97 |
| 5.4 | Experimental verification of the role of coherence in the optical bistability | 99 |
| 5.5 | Study of switch-on time of Stokes generation | 102 |
| 5.6 | Conclusion | 103 |
| 6 | FPGA-based photon counting module | 106 |
| 6.1 | Principle of operation | 106 |
| 6.1.1 | Pulse shaping | 107 |
| 6.1.2 | Coincidence Logic | 108 |
| 6.1.3 | Counting principle | 108 |
| 6.1.4 | FIFO | 110 |
| 6.1.5 | Data transfer using Labview | 110 |
| 6.2 | Implementation and Performance of the module | 111 |
| 6.2.1 | Pulse-shaping | 111 |
| 6.2.2 | Periodic and Pseudo-random pulses counting | 113 |
| 7 | Future prospectives | 115 |
| | Appendix A Fundamental Physical Constants | 117 |
| | Appendix B Rubidium cell housing | 119 |

SUMMARY

Using thermal rubidium vapor as the nonlinear medium, we have demonstrated different effects arising due to ground-state-coherence enhanced four wave mixing and cross phase modulation.

In a two-level system with Zeeman coherence, we demonstrate the polarisation rotation of an input elliptically polarised light. A theoretical model based on the propagation of light through the nonlinear medium is used to explain the effect and from the theoretical fitting of the experimental data, the nonlinear susceptibilities induced in the medium are estimated. Exploiting the hyperfine coherence in a double- Λ system, the phenomenon of mirrorless optical parametric oscillation (MOPO) with a pump conversion efficiency $\sim 30\%$ is demonstrated. Due to strong XPM in the system, the generated beams via MOPO experience transverse refractive index potentials leading to the excitation of correlated spatial modes. We report the generation of Gaussian and Laguerre-gaussian modes with symmetric Gaussian pump beam and generation of Hermite-Gaussian modes with asymmetric Gaussian pump beam as a result of the waveguiding effect. A semi-classical model of four-level atomic system interacting with four light fields is used to evaluate the induced XPM in the medium and the propagation equations of the light fields are used to understand the generation of the spatial modes. A bistability in the threshold of the MOPO is experimentally observed. This effect is a result of the hyperfine coherence induced between the ground states and the role of coherence is experimentally verified in the system. We have also investigated the possibility of a phase transition at the threshold of MOPO by studying the switch-on time of the generated beams. The critical exponent (c) in this case is found to be -0.854 ± 0.015 unlike for the cases of bistability observed with a saturable absorber inside a cavity, where the typical value of c is -0.5 . A photon counter module based on an FPGA card has been designed to study different nonlinear effects such as MOPO at few photon level and generation of vacuum squeezed state. The module, which consists of different parts such as pulse shaping, coincidence logic, counter, FIFO and data transfer to PC has been verified using electrical signals from a function generator.

List of Figures

| | | |
|------|---|----|
| 1.1 | Illustration of configurations with (a) Zeeman coherence and (b) Hyperfine coherence for the D_2 line of ^{85}Rb ($5^2S_{1/2} \rightarrow 5^2P_{3/2}$ transition). | 2 |
| 2.1 | Schematic of the SPM process in a two-level system. | 17 |
| 2.2 | Schematic of the XPM process in a two-level system. | 18 |
| 2.3 | a) Schematic of the FWM process in a two-level system. b) Forward geometry and c) backward geometry of FWM. | 19 |
| 2.4 | a) HG modes with index (l,m). | 22 |
| 2.5 | a) LG modes with index (l,m). | 23 |
| 2.6 | Schematic of two-level atomic system coupled by a laser field of optical frequency ω detuned by Δ from the atomic transition. The spontaneous decay rate of the excited state, $ e\rangle$ to the ground state, $ g\rangle$ is Γ | 24 |
| 2.7 | Energy level diagram for bare and dressed atomic states. The dotted lines correspond to the energies corresponding to the bare states whereas the red solid lines refer to the energies corresponding to the dresses states. | 26 |
| 2.8 | a) $\text{Im}(\chi)$ and b) $\text{Re}(\chi)$ for two-level system for atoms at rest. The parameters used are, $\Gamma = 2\pi \times 6$ MHz, $\Omega = 2\pi \times 0.1$ MHz and $N = 10^{13}\text{cm}^{-3}$ | 29 |
| 2.9 | Schematic diagram of electronic energy level configuration for D_1 and D_2 lines of ^{85}Rb | 30 |
| 2.10 | Schematic diagram of electronic energy level configuration for D_1 and D_2 lines of ^{87}Rb | 31 |
| 2.11 | Experimental setup for saturated absorption spectroscopy. M: Mirror, PBS: Polarising beam splitter, PD: Photodetector. | 33 |
| 2.12 | Experimentally recorded saturation absorption spectroscopy. | 34 |

| | | |
|------|---|----|
| 2.13 | a) Schematic of 4-f imaging technique. L1, L2: Lens, f : Focal length of lens. b) Image of the imprinted glassplate. c) CCD image of the laser beam profile with the imprinted image at the image plane. | 36 |
| 3.1 | (a) Schematic of degenerate FWM for orthogonal linearly-polarized pump and probe fields. (b) Illustration of a basic process of FWM using Zeeman degenerate hyperfine sublevels. | 40 |
| 3.2 | Experimental setup for the observation of FWM and XPM. M: Mirror, PBS: Polarising beam splitter, AOM: Acousto-optic modulator, A: Aperture, L: Lens, PD: Photo-detector. | 41 |
| 3.3 | a) Rubidium spectroscopy reference b) 2δ beat signal while scanning the laser detuning. Expanded beat signals for A) ^{87}Rb and B) ^{85}Rb | 42 |
| 3.4 | Observation of FWM beat signal. spectrum analyzer showing the beat amplitude as a result of the interference between probe and the newly generated fields recorded (a) without magnetic field compensation and (b) with magnetic field compensation. The insets show the corresponding beat signals. | 42 |
| 3.5 | Observation of nonlinear magneto-optic rotation. blue line denotes the transmission in the orthogonal direction of the pump beam in presence of a finite magnetic field and red line denotes the transmission after field compensation. | 43 |
| 3.6 | a) 2δ -peak height as a function of the frequency offset δ . b) Visibility of the 2δ beat signal as a function of δ | 44 |
| 3.7 | Observation XPM in the system. The probe transmission measured (a) with phase-matching and, (b) without phase-matching condition. | 45 |
| 3.8 | a) Scheme of FWM process showing non-conservation of angular momentum and b) Probe transmission showing non-existence of FWM process for the case when pump and probe light fields are of $\sigma^+ - \sigma^-$ Polarizations. | 45 |
| 3.9 | Bloch sphere representation of polarization states. | 47 |
| 3.10 | (a) Normalized output probe intensity as a variation of the relative phase of the pump and the probe fields. (b) Contour plot of visibility in the parameter space of $\Delta k z$ and $\kappa_s z$. The red solid lines refers to the visibility for $\Delta k = -\kappa_s$ and $\Delta k = \kappa_s$ | 51 |

| | | |
|------|---|----|
| 3.11 | Variation of visibility with z for $\Delta k = 0$ (red dashed line), $\Delta k = \kappa_s$ (black dash-dotted line), $\Delta k = 2\kappa_s$ (blue dotted line) and $\Delta k = 20\kappa_s$ (orange solid line). The value of κ_s used is 57 m^{-1} | 53 |
| 3.12 | Schematic of the experimental arrangement to measure the Polarization rotation. M: Mirror, PBS: Polarizing beam splitter, NPBS: Non-Polarizing beam splitter, CCR: Corner cube retro-reflector, $P(\theta)$: Polarizer aligned at θ w.r.t $ V\rangle$, P: Glan-Thompson polariser, PD: Photo-detector. | 55 |
| 3.13 | a) Schematic of piezo actuator attached to Corner cube retro-reflector (CCR). b) A typical interference signal between the pump and probe when the phase difference between them is varied using the piezo. The black circles represent the experimental data whereas the red line shows its fitting with a sinusoidal function. | 56 |
| 3.14 | Bloch sphere representation showing the polarization rotation of light field. The solid line (blue) represents the input polarization states and points (red) denote the output polarization states. | 57 |
| 3.15 | Output Bloch sphere parameters (a) ϕ_{out} and (b) θ_{out} as a function of ϕ_{in} . The open circles are the experimental data and the red solid curves are the theoretical fitting. | 58 |
| 3.16 | Variation of (a) $ \chi_{FWM}^{eff} $ and (b) $\text{Re}(\chi_{XPM}^{eff})$ as a function of pump intensity, I_p . The open circles denote the experimental data and the solid lines represent the fittings to quadratic functions. | 59 |
| 4.1 | Schematic of energy level diagram with the coupling of the input pump and control laser fields (solid lines) and the generated Stokes and anti-Stokes fields (dashed lines). | 64 |
| 4.2 | Schematic of the experimental setup. PBS: Polarising beam splitter, P: Polariser, M: Mirror, NPBS: Non-polarising beam splitter, PD: Photo-detector, SA: Spectrum analyser, FPI: Fabry-Perot Interferometer. | 65 |
| 4.3 | The frequencies of the input as well as the generated beams depicted in Rb absorption spectrum. The Stokes beam being generated outside the Doppler linewidth does not undergo absorption and hence is used for analysis. | 66 |

| | | |
|-----|---|----|
| 4.4 | a) Fabry-Perot cavity signal, which shows the frequency difference of about 35 MHz between the pump and the Stokes beam. b) Spectrum analyzer signal showing the beat frequency between the pump and the Stokes beam. Black circles denote the experimental data and the red lines correspond to the Lorentzian fitting with a width of 14 kHz. | 67 |
| 4.5 | a) Stokes power variation with input pump power, where the control power is fixed at 54 mW b) Stokes power variation with input control power. The pump power is fixed at 1.6 mW. | 67 |
| 4.6 | a) Energy level configuration with four levels used for the theoretical model. b) Transmission and nonlinear refractive index (Δn) of the generated beams. The red solid line corresponds to the anti-Stokes beam and the black solid line corresponds to the Stokes beam. We present the scaling for the anti-Stokes and Stokes beam in the left-axis and right axis of the graph respectively. The blue dotted line represents the line of null refractive index. | 70 |
| 4.7 | Schematic of the experimental setup for probe transmission in N-type system. M: Mirror, L: Lens, PBS: Polarising beam splitter, PD: Photo-detector. | 72 |
| 4.8 | a) Matching of the experimentally measured and the theoretically calculated transmission of the external probe beam. The black circles denote the experimental data and the red solid line represents the data from the theoretical model. The CCD images of the probe beam for b) lower and c) higher value of Δ . The scales of both the images are same. | 73 |
| 4.9 | Nonlinear refractive index (Δn) as a function of the two-photon detuning, a) δ_a for anti-Stokes and d) δ_s for Stokes fields. Approximate Gaussian potentials experienced by the b) anti-Stokes and e) Stokes fields. The black circles denote the potentials evaluated from the theoretical model and the red solid line represents the functional fitting of the form, $c_1(-e^{-x^2/(\Delta x_c)^2} + c_2e^{-x^2/(\Delta x_p)^2})$ and $c_3(-e^{-x^2/(\Delta x_p)^2})$ for the anti-Stokes and Stokes beams respectively. Here, $c_1 = 2.4 \times 10^3 \text{ m}^{-1}$, $c_2 = 0.065$, $c_3 = 3.5 \times 10^2 \text{ m}^{-1}$, $\Delta x_c = 680 \text{ }\mu\text{m}$ and $\Delta x_p = 142 \text{ }\mu\text{m}$. The horizontal blue solid lines on the potentials refers to the corresponding theoretically calculated eigenvalues. The normalized ground-state eigenfunction of the waveguide for the case of c) anti-Stokes field and f) Stokes fields. | 75 |

| | | |
|------|--|----|
| 4.10 | Experimental setup for observation of correlated spatial modes. PBS: Polarising beam splitter. | 78 |
| 4.11 | CCD images of the symmetric Gaussian mode for a) Stokes and b) anti-Stokes beam. The corresponding transverse intensity patterns for c) Stokes and d) anti-Stokes fields. CCD images of the first-order Laguerre-Gaussian (LG01) mode in the generated e) Stokes and f) anti-Stokes fields. The corresponding transverse intensity profiles for the g) Stokes and h) anti-Stokes fields. The intensity profiles are normalized to the peak value of intensities and are fitted with corresponding Gaussian or Laguerre-Gaussian (LG01) distribution functions. | 79 |
| 4.12 | Experimental arrangement for determining handedness of the generated LG beams. CL: Cylindrical lens. | 80 |
| 4.13 | Experimental observation of the LG modes in the generated a) Stokes and b) anti-Stokes beams at the focal plane of the cylindrical lens. | 81 |
| 4.14 | CCD images of the asymmetric gaussian mode in the generated a) Stokes and b) anti-Stokes fields. The first-order Hermite-Gaussian (HG01) mode in the generated c) Stokes and d) anti-Stokes fields. | 82 |
| 4.15 | Multimode frequency comb signal with pump power a) 1.2 mW and b) 2.5 mW. The inset shows the corresponding transverse profiles of the generated beams. | 84 |
| 4.16 | CCD images of higher order modes in the generated a), c) Stokes beam and b), d) anti-Stokes beam. | 85 |
| 5.1 | Schematic of energy level diagram for MOPO process. | 91 |
| 5.2 | Variation of the pump conversion efficiency (η) with different values of $\kappa_0\Omega_i l$ | 94 |
| 5.3 | Gaussian nature of the Rabi-frequency with peak value Ω_m with the radius of MOPO generation being highlighted. | 95 |
| 5.4 | Schematic of experimental setup for the observation of MOPO-based optical bistability. PBS: Polarising beam splitter, PD: Photodetector. | 96 |
| 5.5 | Variation of bistability width with modulation frequency for a) 50 Hz, b) 5 kHz and c) 50 kHz. The black line refers to forward direction and the red line refers to the backward direction of the pump power variation. | 97 |

| | | |
|------|---|-----|
| 5.6 | Variation of the forward threshold (black circles) and backward threshold (blue circles) as a function of the width with modulation frequency. The solid red line refers to the theoretical fitting. | 98 |
| 5.7 | a)Variation of Stokes power with input pump power. The blue open circles (red squares) shows experimentally measured variation in the increasing (decreasing) pump power direction and the black points show the theoretical fitting. b) Variation of the forward threshold Rabi frequency with the pump beam waist (w_0). | 99 |
| 5.8 | Illustration of the pump modulation function. | 100 |
| 5.9 | Experimental evidence of atomic coherence based bistability. The Red line shows the input pump power variation and the blue line shows the generated Stokes power variation. Highlighted area of a) is expanded and presented in b). | 101 |
| 5.10 | Coherence time measured with different beam waists of pump beam. The black circles are experimental data and the red line shows the linear fitting. | 101 |
| 5.11 | a) Output pump power, b) Stokes power (red line) and anti-Stokes power (blue line) in response to a pulsed input pump. | 102 |
| 5.12 | a) Variation of switch-on time of Stokes beam generation with input pump power. b) Critical exponent measured with different control powers and different densities of the vapor cell. The red circles (black squares) represent the data corresponding to vapor density of $6 \times 10^{12} \text{ cm}^{-3}$ (10^{13} cm^{-3}). | 103 |
| 6.1 | Block diagram of the multi-photon coincidence counting module | 107 |
| 6.2 | Architecture of pulse shaping | 107 |
| 6.3 | Block diagram of Coincidence logic | 109 |
| 6.4 | Block diagram of counting principle | 109 |
| 6.5 | Block diagram of FIFO | 110 |
| 6.6 | Photograph of FPGA board with daughter card | 111 |
| 6.7 | a) Input pulse with 100 ns and pulse-shaped output with widths b) 8.2 ns c) 17.5 ns and d) 45 ns respectively. | 112 |
| 6.8 | Screen shot of the Labview display showing counting and coincidence in different channels | 113 |
| B1 | Schematic of Rubidium cell housing. | 119 |

List of Tables

| | | |
|----|--|-----|
| A1 | Fundamental physical constants. Adapted from: https://physics.nist.gov/cuu/Constants | 117 |
| A2 | Properties of ^{85}Rb . Adapted from: Steck, D. A. Rubidium 85 d line data, http://steck.us/alkalidata | 118 |

Chapter 1

Introduction

With the advent of the laser as a coherent intense source of light in the 1960s, the field of nonlinear optics gained momentum and it has been continuously growing ever since. Nonlinear optical effects are a consequence of the nonlinear susceptibility induced in the medium in response to an intense light field. The first experimentally demonstrated nonlinear phenomenon was the second harmonic generation by Franken *et al.* [1]. Other interesting nonlinear optical effects include optical parametric oscillation, sum and difference frequency generation, self-phase modulation, cross-phase modulation, four-wave mixing, etc.

Four-wave mixing (FWM) is a well-known phenomenon, which has been extensively investigated leading to a wide range of applications. FWM has been used for phase conjugation [2], spectroscopy [3, 4], squeezed state generation [5, 6] and formation of entangled images [7]. Strong relative intensity squeezing [8] and the strong quantum correlation between the generated beams [9] using FWM in a three-level system has been demonstrated in thermal Rubidium vapor. A pulse storage scheme using FWM is demonstrated by Camacho *et al.* [10]. There is recent work on the study of FWM in a double- Λ system regarding phase correlation between the FWM process and the optical fields [11].

On the other hand, cross-phase modulation (XPM) is the phenomenon of change of phase of a weak beam by the intensity of another beam through nonlinear interaction, which results in the intensity-dependent refractive index in the medium. XPM has promising application towards quantum non-demolition measurement [12], quantum teleportation [13], slow-light propagation [14–16] and all-optical waveguiding [17, 18].

Atomic vapors are widely used for the study of different nonlinear phenomena because of their exceptionally large resonant nonlinearities. They are the simplest experimental approach for the study of atom-light interaction and hence are the workhorse for the demonstration of

many interesting phenomena. The works undertaken in the thesis are based on the applications of two basic nonlinear phenomena i.e. FWM and XPM enhanced by ground-state coherence in thermal atomic vapor.

This chapter reviews the past research on the ground state coherence induced nonlinear optical processes to extend the effects towards interesting applications as presented in the thesis. First, a brief introduction to the ground state coherence is presented. Then past works of literature based on the enhanced nonlinear processes due to ground state coherence are reviewed. The objective of the thesis is presented followed by a brief outline of the thesis.

1.1 Introduction to the ground state coherence

Atomic coherence is the coherence developed between the states of an atom due to its interaction with an electromagnetic field. Mathematically, it refers to the off-diagonal elements in the density matrix given as $\rho_{n,n'}$, where $|n\rangle$ and $|n'\rangle$ are the energy states of the atomic system with $n \neq n'$. When atomic coherence is created between the ground states of a multi-level atomic system, it is known as the ground-state coherence. The ground state coherence can be Zeeman coherence when the energy levels are two Zeeman sublevels belonging to the same hyperfine state or it can be Hyperfine coherence when the energy levels belong to two different hyperfine states of the atom.

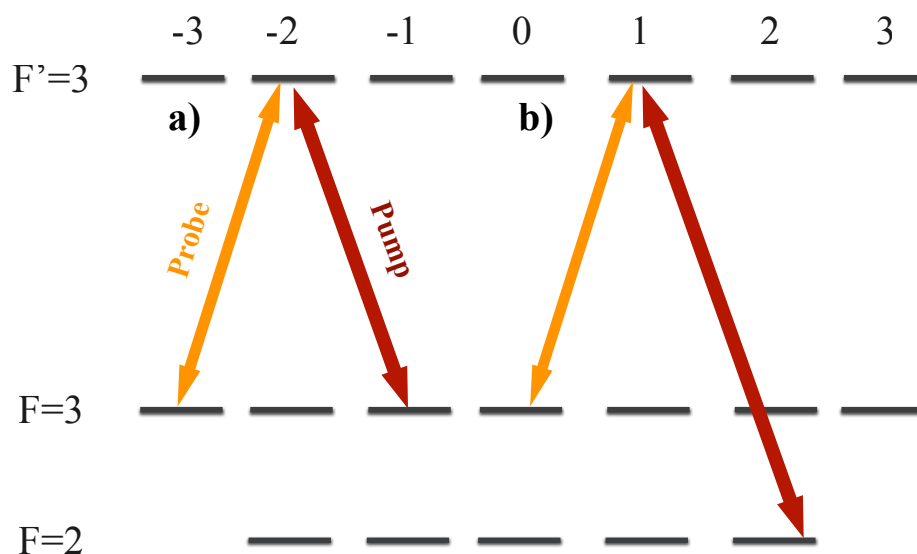


Figure 1.1: Illustration of configurations with (a) Zeeman coherence and (b) Hyperfine coherence for the D_2 line of ^{85}Rb ($5^2S_{1/2} \rightarrow 5^2P_{3/2}$ transition).

The configurations for achieving ground state coherence are shown in Fig. 1.1. It has been illustrated for atoms with hyperfine spin F such that there are $2F + 1$ possible Zeeman sublevels. Here, we have considered two hyperfine ground states ($F = 2, 3$) and one excited state ($F' = 3$) with their corresponding magnetic sublevels. In this case, one excited state is coupled to two ground states using two coherent lasers called as the probe and pump fields with opposite circular polarisation in a lambda-type scheme. The configurations for achieving Zeeman coherence and Hyperfine coherence are presented in Fig. 1.1 (a) and (b) respectively. These coherences are usually limited by the spin-exchange collision and the transit time of atoms through the laser beams. To suppress the ground state decoherence in the vapor cells, the cell walls are paraffin-coated to reduce the spin-exchange collision or the cells are filled with buffer gas, which increases the transit time by virtually immobilizing the vapor. The use of magnetic shields reduces the magnetic field noise and hence the corresponding decoherence.

Hanle *et al.* [19] proposed the idea of interference between different atomic states and its evolution in the presence of an external magnetic field. Another of the earliest experimental evidence of atomic coherence is the work by Guiochon-Bouchiat *et al.* [20]. They observed a decrease in the width of double resonance in mercury vapor with increasing temperature, which was later confirmed to be due to coherent multiple scattering. Gao *et al.* [21] and Lezama *et al.* [22] theoretically studied the effect of Zeeman coherence on the two-level atomic system. The generation of an arbitrary quantum state in a cavity via Zeeman coherence has been proposed by Parkins *et al.* [23].

Atomic coherence can be prepared by many different methods. Few techniques include coherent population trapping, Electromagnetically induced transparency, Stimulated Raman adiabatic passage and Raman scattering.

For the case of a generic Λ -system with two ground states $|1\rangle$, $|2\rangle$ and a excited-state $|3\rangle$ resonantly interacting with two laser fields, one of the eigenstates of the Hamiltonian in a suitable rotating frame reads as, $|\psi\rangle = c_1 |1\rangle - c_2 |2\rangle$. Here c_1 and c_2 are functions of the field amplitudes. In this case, the transition dipole moment, $\langle 3|\mu|\psi\rangle$ vanishes and hence, the state becomes decoupled from the input laser fields. This is known as the dark state as it suppresses the resonant fluorescence. The state is maximally coherent when $c_1 = c_2$. As the dark state has no excitation probability, all the populations are trapped in this state by spontaneous decay. This effect is called a coherent population trapping (CPT) [24]. The first experimental work on CPT dates back to 1976 by Alzetta *et al.* [25] observed as suppression in the fluorescent emission in

a three-level Λ -system. Few of the earliest theoretical analyses include the works by Whitley *et al.* [26], Arimondo *et al.* [27]. Gray *et al.* [28] demonstrated CPT based on Zeeman coherence using a dye laser. CPT has found diverse applications like precision spectroscopy [29,30], slow light [31,32], laser cooling [33], magnetometry [34,35] and atomic clocks [36,37].

Another interesting phenomenon arising from dark resonance is electromagnetically induced transparency (EIT) [38,39], in which one of the bare states (ground states in case of Λ -system) becomes the dark state. It is achieved when one of the input fields is stronger (coupling) than the other (probe). The medium, in this case, becomes transparent to the weak probe field in the presence of the strong field under resonance condition. After being termed as EIT by Harris *et al.* [40], the phenomenon was first experimentally observed by Bollinger *et al.* [41]. EIT has been utilised for atomic clocks [42], slow light propagation [14,43], generation and storage of single-photon pulses [44,45] and magnetometry [46]. The probe light while propagating through an EIT medium, experiences atomic coherence and leads to the formation of dark state polariton [47], which is a mixture of light and atomic excitation. Using dark-state polaritons, there are proposals on the transfer of quantum correlations between light and atom [48,49] leading to the controlled storage and retrieval of light [16,50] as well as transport and time-reversal of light [51].

Stimulated Raman adiabatic passage (STIRAP) is a technique based on atomic coherence to efficiently transfer population between the ground states, which are coupled by two driving pulses via an intermediate level [52,53]. STIRAP is robust against losses due to radiative decays and is only limited by the lifetime of ground-state coherence. Oberst *et al.* have studied the preparation and time-resolved probing of ground-state coherence using STIRAP [54].

Raman scattering in a Λ -type atomic system is a consequence of three-wave mixing of a strong pump field, a weak Stokes field and the atomic spin-wave due to the ground state coherence. The idea of quantum communication using Raman scattering in the atomic ensemble is proposed by Duan *et al.* [55]. Enhanced Raman scattering in atomic vapor due to the atomic spin wave is proposed by Yuan *et al.* [56].

1.2 A review on enhanced XPM due to ground state coherence

The ground state coherence in the multi-level atomic system is found to enhance different nonlinear optical processes. In general, the efficiency of the nonlinear processes depends on the interplay between the linear and nonlinear susceptibility. Since coherent phenomena like EIT and CPT are characterized by the suppression of linear susceptibility and enhancement of nonlinear susceptibility [40], these processes can lead to efficient nonlinear processes even at low light level [57].

The proposal to achieve a large index of refraction using atomic coherence was predicted [58]. Steep dispersion with $dn/dv = -2 \times 10^{-11} \text{Hz}^{-1}$ and enhanced Kerr nonlinearity for the case of Zeeman degenerate two-level system is reported by Akulshin *et al.* [59, 60]. The narrow transmission window for the case of EIT results in the dramatic modification of the dispersive properties of the medium [61]. The enhanced refractive index via EIT [62] leads to the decrease in the group velocity (v_g) and hence the slowing down of a probe pulse. There are theoretical studies on dispersive properties of EIT by Harris *et al.* [63], who noted an optical delay of 83 ns i.e. $c/v_g = 250$. The value of v_g pertaining to the largest XPM measured in an atomic medium is 17 m s^{-1} demonstrated for the case of BEC [14] and 8 m s^{-1} demonstrated for the case of thermal vapor [64]. There are also reports on storing the probe pulse for up to 1 ms using the giant Kerr nonlinearity due to EIT [15, 16]. A review of EIT-based quantum memory is presented in [65].

The nonlinearity associated with EIT can be enhanced using a double- Λ configuration [66]. In this case, the transparency occurs when the ratio of Rabi frequencies in each Λ -channel is equal [67]. Storage of a pair of pulses using EIT in a double- Λ system is proposed [68]. Large cross-phase modulation is reported at a few photon levels in a double- Λ system by Liu *et al.* [69]. Enhanced XPM between two weak fields in a four-level tripod system is demonstrated by Li *et al.* [70]. A four-level system is proposed by Schmidt *et al.* [71] and a five-level system with double-dark resonances is proposed by Niu *et al.* [72] for enhanced Kerr nonlinearity using EIT. A giant Kerr-nonlinearity in a four-level system is reported in [73, 74]. With laser-cooled atoms, Chen *et al.* have demonstrated low-light-level XPM [75]. EIT assisted large XPM is also observed in an inverted Y-system [76]. The enhanced cross-Kerr nonlinearity due to EIT also leads to spatial beam displacements of FWM beams [77]. Low light level XPM has been

observed using an N-type system [78] as well as an M-type system [79].

1.3 A review on enhanced FWM due to ground state coherence

CPT being an optical pumping process, can lead to a large optical gain for wave mixing at lower input intensity than that required to saturate an optical transition. Hemmer *et al.* [80] have reported high phase conjugate gain ($\simeq 50$) with a pump intensity as low as 1 W/cm^2 in sodium vapor. FWM in a double Λ system involves the interaction of two strong beams and amplification of two weak beams such that the enhancement of FWM is based on the hyperfine coherence in each Λ channel. Using a double- Λ system, efficient non-degenerate FWM was achieved under the effect of CPT [81, 82]. Zeeman coherence induced four-wave mixing in the two-level scheme has also been demonstrated [83, 84].

The phenomenon of EIT was proposed to greatly enhance the FWM process by reducing the absorption by Harris *et al.* [40]. An Enhancement of four-wave mixing based on EIT with rubidium atoms has been reported [85]. Jain *et al.* have demonstrated EIT based phase-matching for four frequency mixing [86] as well as frequency conversion from 425 to 293 nm with an efficiency of 40% [87]. Seeded FWM [88] as well as unseeded FWM [18] assisted by EIT is achieved with low light in the cold atomic ensemble. Deng *et al.* [90] proposed a four-level scheme for FWM and showed that EIT leads to the enhancement of the generated field by many orders of magnitude. A quantum analysis of resonant FWM based on EIT is noted by Johnsson *et al.* [91]. A five-level atomic system is proposed for large enhancement of FWM using dark resonances by Wu *et al.* [92] and Yang *et al.* [93]. Highly efficient FWM process in a Y-type system assisted by EIT is studied by Zhang *et al.* [94]. Using a double- Λ system with the strong input beams sharing a common excited state, there is a demonstration on FWM with conversion efficiency more than 30% by Merriam *et al.* [95]. Payne *et al.* also proposed to achieve a 100% conversion efficiency of FWM leading to quantum entanglement of Fock states [96]. Backward FWM of near 100% conversion efficiency was proposed using a four-level system with EIT by Kang *et al.* [97].

Hakuta *et al.* noted improvement of FWM by maximal coherence achieved through stimulated Raman scattering [98] in molecular Hydrogen (H_2). Sautenkov *et al.* [99] and Wang *et al.* [100] have demonstrated enhanced field generation via fractional STIRAP.

1.4 Thesis objective

The objective of the thesis is to address the various applications due to the enhanced nonlinear processes as a result of ground-state coherence in the system. The applications include polarisation rotation of light, the mirrorless optical parametric oscillator (MOPO) inside an all-optical waveguide and optical bistability in the threshold of MOPO demonstrated in thermal atomic vapor. Using a system with Zeeman degenerate ground states, we report the rotation of an input elliptically polarized light due to efficient FWM and XPM. We use a theoretical analysis of the propagation of light through the nonlinear medium to explain the polarisation rotation. From the fitting of the experimental data, we determine the values of third-order non-linear susceptibilities associated with the nonlinear processes in the system. In further experiments with a double-lambda system exhibiting enhanced FWM and XPM due to hyperfine ground state coherence, a phenomenon known as MOPO is investigated. The spontaneous four-wave mixing process in the counter-propagating configuration of pump and control fields interacting with a multilevel atomic system facilitates the generation of mirrorless Stokes and anti-Stokes fields, which are counter-propagating to each other. Here, an efficient MOPO is demonstrated under the effect of an all-optical waveguide. We report the maximum generated Stokes power up to mW with pump conversion efficiency more than 30%. We show that the nonlinear propagation equations of the generated light fields under the effect of the cross-phase modulation due to the input strong fields resembles Schrodinger's equation with a two-dimensional Gaussian potential. This all-optical waveguide results in different spatial modes in both the generated fields. We report correlated Gaussian mode as well as Laguerre-Gaussian mode for both the generated fields with suitable experimental parameters. In the further measurement of the threshold condition, optical bistability is observed in the MOPO process i.e. the pump threshold value for increasing pump power direction is different from the value for decreasing pump power direction. The experimental observation of a discontinuity of the generated field at the threshold implies the presence of a first-order phase transition with the generated field being the order parameter. An FPGA-based photon counting module was also designed within the span of the Ph.D. project to study MOPO in the single-photon regime.

1.5 Thesis organization

In this section, a brief layout of the thesis is presented. The chapter breakdown for the thesis is as follows;

Chapter 2 includes a discussion on the theoretical background and experimental tools that are used in the works presented in the thesis. The chapter contains the basics of nonlinear processes like FWM and XPM, properties of the rubidium and a detailed derivation of Maxwell's propagation equation inside the nonlinear medium.

Chapter 3 outlines the study of polarisation rotation of light due to Zeeman coherence induced enhanced FWM and XPM in thermal rubidium vapor. The detailed experimental setup is discussed along with the theoretical model giving estimates of the nonlinearities induced in the medium.

Chapter 4 contains the demonstration of the mirrorless optical parametric oscillator (MOPO) assisted by the enhanced nonlinearity due to the hyperfine coherence. The experimental setup and the results of different parameter regimes are discussed. The chapter also presents the theoretical model of the four-level system and the derivation of propagation equations to explain the experimental data.

Chapter 5 outlines the experimental observation of optical bistability in the threshold of MOPO. The corresponding experimental setup and the results are presented. The role of atomic coherence for the process is discussed along with the experimental evidence. The possibility of first-order phase transition at the threshold is discussed and the measured critical exponent is presented.

The discussion on the development of FPGA-based single-photon counting module is presented in chapter 6. The different parts of the module such as pulse shaping, coincidence logic, and counting procedure are explained in detail. The preliminary data recorded using signal pulses from function generators are presented as a verification of the module.

Finally, the future scope of the research is discussed in chapter 7.

Bibliography

- [1] P. A. Franken, A. E. Hill, C. W. Peters, and G. Weinreich *Phys. Rev. Lett.* **7**, 118 (1961).
- [2] R. W. Hellwarth, *J. Opt. Soc. Am.* **67**, 1 (1977).
- [3] J.-L. Oudar and Y. R. Shen, *Phys. Rev. A* **22**, 1141 (1980).
- [4] M. Schmitt, G. Knopp, A. Materny, and W. Kiefer, *Chem. Phys. Lett.* **280**, 339 (1997).
- [5] R. E. Slusher, L. W. Hollberg, B. Yurke, J. C. Mertz, and J. F. Valley, *Phys. Rev. Lett.* **55**, 2409 (1985).
- [6] M. D. Lukin, A. B. Matsko, M. Fleischhauer, and M. O. Scully *Phys. Rev. Lett.* **82**, 1847 (1999).
- [7] V. Boyer *et al.* *Science* **321**, 544 (2008).
- [8] C. F. McCormick, V. Boyer, E. Arimondo, and P. D. Lett, *Opt. Lett.* **32**, 178 (2007).
- [9] C. F. McCormick, A. M. Marino, V. Boyer, and P. D. Lett *Phys. Rev. A* **78**, 043816 (2008).
- [10] Ryan M. Camacho, Praveen K. Vudiyasetu and John C. Howell, *Nat. Phot.* **3**, 103–106 (2009).
- [11] T. Jeong and H. S. Moon, *Opt. Express* **24**, 28774-28783 (2016).
- [12] J. Ph. Poizat and P. Grangier, *Phys. Rev. Lett.* **70** 271 (1993).
- [13] D. Vitali, M. Fortunato and P. Tombesi, *Phys. Rev. Lett.*, **85** 445 (2000).
- [14] L. V. Hau, S. E. Harris, Z. Dutton, and C. H. Behroozi, *Nature* **397**, 594 (1999).
- [15] C. Liu, Z. Dutton, C. H. Behroozi, and L. V. Hau, *Nature* **409**, 490 (2001).

- [16] D. F. Phillips, A. Fleischhauer, A. Mair, R. L. Walsworth, and M. D. Lukin, *Phys. Rev. Lett.* **86**, 783 (2001).
- [17] H. Shpaisman, A. D. Wilson-Gordon, and H. Friedmann, *Phys. Rev. A* **71**, 043812 (2005).
- [18] P. K. Vudyasetu, D. J. Starling, and J. C. Howell, *Phys. Rev. Lett.* **102**, 123602 (2009).
- [19] W. Hanle, *Z. Phys.* **30**, 93 (1924).
- [20] M.-A. Guiochon-Bouchiat, J.-E. Blamont, J. Brossel, *C. R. Acad. Sci* **243**, 1859 (1956).
- [21] B. Gao *Phys. Rev. A* **49** 3391 (1994).
- [22] A. Lezama, S. Barreiro, A. Lipsich, and A. M. Akulshin *Phys. Rev. A* **61** 013801 (1999).
- [23] A. S. Parkins, P. Marte, P. Zoller, and H. J. Kimble, *Phys. Rev. Lett.* **71**, 3095 (1993).
- [24] E. Arimondo, *Progress in Optics*, **35**, 257-354 (1996).
- [25] G. Alzetta, A. Gozzini, L. Moi, and G. Orriols, *Nuovo Cimento Soc. Ital. Fis.*, **B 36**, 5 (1976).
- [26] R. M. Whitley, and C. R. Stroud, *Phys. Rev. A* **14**, 1498, (1976).
- [27] E. Arimondo, and G. Orriols, *Lett. Nuovo Cimento Soc. Ital. Fis.* **17**, 333, (1976).
- [28] H. R. Gray, R. M. Whitley, and C. R. Stroud, *Opt. Lett.* **3**, 218 (1978).
- [29] P.R. Hemmer, S. Ezekiel, C.C. Leiby, *Opt. Lett.* **8**, 440 (1983).
- [30] R. Wynands, A. Nagel, *Applied Physics B*, **68(1)**, 1-25 (1999).
- [31] O. Schmidt, R. Wynands, Z. Hussein, and D. Meschede, *Phys. Rev. A*, **53(1)** R27—R30 (1996).
- [32] V. Shah and J. Kitching *Adv. At., Mol., Opt. Phys.* **59** 21-74 (2010).
- [33] A. Aspect, E. Arimondo, R. Kaiser, N. Vansteenkiste, C. Cohen-Tannoudji, *Phys. Rev. Lett.* **61**, 826 (1988).
- [34] A. Nagel, L. Graf, A. Naumov, E. Mariotti, V. Biancalana, D. Meschede, R. Wynands, *Europhys. Lett.* **44**, 31 (1998).

- [35] P.D. Schwindt, S. Knappe, V. Shah, L. Hollberg, J. Kitching, L. A. Liew *et al. Appl. Phys. Lett.* **85**(26) 6409-6411 (2004).
- [36] J. Vanier, *Appl. Phys. B*, **81**(4), 421-442, (2005).
- [37] J. Kitching, S. Knappe, and L. Hollberg, *Appl. Phys. Lett.*, **81**(3), 553-555, (2002).
- [38] S. E. Harris *Physics Today* **50**, 36 (1997).
- [39] M. Fleischhauer, A. Imamoglu, and J. P. Marangos, *Rev. Mod. Phys.* **77**, 633 (2005).
- [40] S. E. Harris, J. E. Field and A. Imamoglu *Phys. Rev. Lett.* **64**, 1107 (1990).
- [41] K. J. Boller, A. Imamoglu, and S. E. Harris, *Phys. Rev. Lett.* **66**, 2593 (1991).
- [42] R. Santra, E. Arimondo, T. Ido, C. H. Greene, and J. Ye. *Phys. Rev. Lett.* **94**, 173002 (2005).
- [43] A. B. Matsko, O. Kocharovskaya, Y. Rostovtsev, A. S. Z. G. R. Welch, and M. O. Scully, *Adv. At., Mol., Opt. Phys.* **46**, 191 (2001).
- [44] M. D. Eisaman *et al.*, *Nature* **438**, 837 (2005).
- [45] T. Chaneliere *et al.*, *Nature* **438**, 833 (2005).
- [46] V. I. Yudin, A. V. Taichenachev, Y. O. Dudin, V. L. Velichansky, A. S. Zibrov, and S. A. Zibrov, *Phys. Rev. A* **82**, 033807 (2010).
- [47] M. Fleischhauer and M. D. Lukin, *Phys. Rev. Lett.* **84**, 5094 (2000).
- [48] M. D. Lukin, S. F. Yelin, and M. Fleischhauer, *Phys. Rev. Lett.* **84**, 4232 (2000).
- [49] A. E. Kozhokin, K. Mølmer, and E. Polzik, *Phys. Rev. A* **62**, 033809 (2000).
- [50] A. Mair, J. Hager, D. F. Phillips, R. L. Walsworth, and M. D. Lukin, *Phys. Rev. A* **65**, 031802 (2002).
- [51] A. S. Zibrov, A. B. Matsko, O. Kocharovskaya, Y. V. Rostovtsev, G. R. Welch, and M. O. Scully, *Phys. Rev. Lett.* **88**, 103601 (2002).
- [52] K. Bergmann, H. Theuer, and B. W. Shore, *Rev. Mod Phys.* **70**, 1003 (1998).

- [53] N. V. Vitanov, A. A. Rangelov, B. W. Shore, and K. Bergmann, *Rev. Mod. Phys.* **89**, 015006 (2017).
- [54] M. Oberst, F. Vewinger, and A. I. Lvovsky, *Opt. Lett.* **32**, 1755 (2007).
- [55] L.-M. Duan, M. D. Lukin, J. I. Cirac and P. Zoller *Nature* **414**, 413–418 (2001).
- [56] C. -H. Yuan, L. Q. Chen, J. Jing, Z. Y. Ou, and W. Zhang *Phys. Rev. A* **82**, 013817 (2010).
- [57] D. A. Braje, V. Balic, G. Y. Yin, and S. E. Harris *Phys. Rev. A* **68** 041801 (R) (2003).
- [58] M. O. Scully, *Phys. Rev. Lett.* **67**, 1855 (1991).
- [59] A. M. Akulshin, S. Barreiro, and A. Lezama *Phys. Rev. Lett.* **83**, 4277 (1999).
- [60] A. M. Akulshin, A. I. Sidorov, R. J. McLean and P. Hannaford *J. Opt. B: Quantum Semi-class. Opt.* **6** 491–494 (2004).
- [61] M. Xiao, Y. -Q. Li, S. -Z. Jin, and J. Gea-Banacloche, *Phys. Rev. Lett.* **74**, 666-669 (1995).
- [62] A. S. Zibrov *et al.*, *Phys. Rev. Lett.* **76**, 3935 (1996).
- [63] S. E. Harris, J. E. Field, and A. Kasapi *Phys. Rev. A* **46**, R29(R) (1992).
- [64] D. Budker, D. F. Kimball, S. M. Rochester, and V. V. Yashchuk, *Phys. Rev. Lett.* **83**, 1767 (1999).
- [65] L. Ma, O. Slattery and X. Tang, *J. Opt.* **19** 043001 (2017).
- [66] M. D. Lukin, P. R. Hemmer, and M. O. Scully, *Advances In Atomic, Molecular, and Optical Physics*, **42** 347–386 (2000).
- [67] S. E. Harris *Phys. Rev. Lett.* **70**, 552 (1993).
- [68] A. Raczynski, J. Zaremba, S. Zielinska-Kaniasty, *Phys. Rev. A* **69** 043801 (2004).
- [69] Z. -Y. Liu *et al.*, *Phys. Rev. Lett.* **117**, 203601 (2016).
- [70] S. Li *et al.*, *Phys. Rev. Lett.* **101**, 073602 (2008).
- [71] H. Schmidt and A. Imamoglu, *Opt. Lett.* **21**, 1936–1938 (1996).

- [72] Y. P. Niu, S. Q. Gang, R. X. Li, Z. Z. Xu, and X. T. Liang, *Opt. Lett.* **30**, 3371 (2005).
- [73] H. Kang and Y. Zhu, *Phy. Rev. Lett.* **91**, 093601 (2003).
- [74] Z.-B. Wang, K.-P. Marzlin, and B. C. Sanders *Phy. Rev. Lett.* **97**, 063901 (2006).
- [75] Y.-F. Chen, C.-Y. Wang, S.-H. Wang, and I. A. Yu *Phy. Rev. Lett.* **96**, 043603 (2006).
- [76] J. Kou, R. G. Wan, Z. H. Kang, H. H. Wang, L. Jiang, X. J. Zhang, Y. Jiang, and J. Y. Gao, *J. Opt. Soc. Am. B* **27**, 2035-2039 (2010).
- [77] Y. Zhang, Z. Nie, H. Zheng, C. Li, J. Song, and M. Xiao, *Phys. Rev. A* **80**, 013835 (2009).
- [78] H. -Y. Lo, P. -C. Su, and Y. -F. Chen, *Phys. Rev. A.* **81**, 053829 (2010).
- [79] B. -W. Shiau *et al.*, *Phy. Rev. Lett.* **106**, 193006 (2011).
- [80] P. R. Hemmer, D. P. Katz, J. Donoghue, M. Cronin-Golomb, M. S. Shahriar, and P. Kumar, *Opt. Lett.* **20**, 982-984 (1995).
- [81] Baolong Lü, W. H. Burkett, and Min Xiao, *Opt. Lett.* **23**, 804-806 (1998).
- [82] B. Lu, W. H. Burkett, and M. Xiao, *Opt. Lett.* **23**, 804 (1998).
- [83] X. W. Xia, D. Hsiung, P. S. Bhatia, M. S. Shahriar, T. T. Grove, and P. R. Hemmer, *Opt. Commun.* **191**, 347 (2001).
- [84] A. M. Akulshin, R. J. McLean, A. I. Sidorov and P. Hannaford *J. Phys. B: At. Mol. Opt. Phys.* **44** 175502 (2011).
- [85] Y. Li and M. Xiao *Opt. Lett.* **21**, 1064 (1996).
- [86] M. Jain, G. Y. Yin, J. E. Field, and S. E. Harris, *Opt. Lett.* **18**, 998 (1993).
- [87] M. Jain, H. Xia, G. Y. Yin, A. J. Merriam, and S. E. Harris, *Phys. Rev. Lett.* **77**, 4326 (1996).
- [88] H. Kang, G. Hernandez, and Y. Zhu *Phys. Rev. A* **70**, 061804(R) (2004).
- [89] D. A. Braje, V. Balic, S. Goda, G. Y. Yin, and S. E. Harris, *Phy. Rev. Lett.* **93**, 183601 (2004).

- [90] L. Deng, M. Kozuma, E.W. Hagley, and M.G. Payne, *Phys. Rev. Lett.* **88**, 143902 (2002).
- [91] M. T. Johnsson and M. Fleischhauer *Phys. Rev. A* **66**, 043808 (2002).
- [92] Y. Wu, J. Saldana, and Y. Zhu *Phys. Rev. A* **67**, 013811 (2003).
- [93] T. Yang *et al.* *J. Phys. B: At. Mol. Opt. Phys.* **38** 2657–2663 (2005).
- [94] Y. Zhang, A. W. Brown, and M. Xiao *Phys. Rev. Lett.* **99**, 123603 (2007).
- [95] A.J. Merriam, S.J. Sharpe, M. Shverdin, D. Manuszak, G.Y. Yin, S.E. Harris, *Phys. Rev. Lett.* **84**, 5308 (2000).
- [96] M. G. Payne and L. Deng, *Phys. Rev. Lett.* **91**, 123602 (2003).
- [97] H. Kang, G. Hernandez, J. Zhang, and Y. Zhu, *J. Opt. Soc. Am. B* **23**, 718 (2006).
- [98] Hakuta, K., M. Suzuki, M. Katsuragawa, and J. Z. Li, *Phys. Rev. Lett.* **79**, 209 (1997).
- [99] V. A. Sautenkov, C. Y. Ye, Y. V. Rostovtsev, G. R. Welch, and M. O. Scully, *Phys. Rev. A* **70**, 033406 (2004).
- [100] Hai-Hua Wang *et al.* *Appl. Phys. Lett.* **93**, 231107 (2008).

Chapter 2

Basic theoretical and experimental tools

This chapter gives an overview of the basic theoretical background and experimental tools employed in the thesis. A brief review of different nonlinear optical processes is discussed. Starting with Maxwell's equation, the propagation equation for a light field inside a nonlinear medium is derived in detail. Different transverse modes of light are discussed followed by a discussion on the semiclassical model of basic atom-light interaction. The properties of rubidium is discussed, which is relevant to the experiments presented in the thesis. This is then followed by a brief discussion on lasers and saturation absorption spectroscopy. Finally, the chapter concludes with a description of the 4-f imaging technique.

2.1 Basics of nonlinear optical effects

In the regime of nonlinear optics, the polarisation $P(t)$, induced in the dielectric medium due to an external applied electric field is given by a power series in the field amplitude $E(t)$.

$$P(t) = \epsilon_0(\chi^{(1)}E(t) + \chi^{(2)}E(t)^2 + \chi^{(3)}E(t)^3 + \dots).$$

Here ϵ_0 is the permittivity of the free space, $\chi^{(1)}$ is the linear optical susceptibility and $\chi^{(2)}$, $\chi^{(3)}$ are the second and third-order nonlinear optical susceptibilities respectively. Here we have assumed that the dielectric medium is lossless and dispersionless.

For the case of a centrosymmetric medium like glass, liquid or vapor, let's consider the possibility of a $\chi^{(2)}$ process given by the nonlinear polarization,

$$P^{(2)}(t) = \epsilon_0\chi^{(2)}E(t)^2.$$

Now a change of sign of the applied electric field requires the sign of the polarisation to change due to the presence of inversion symmetry in the vapor.

$$-P^{(2)}(t) = \epsilon_0 \chi^{(2)}[-E(t)]^2 = \epsilon_0 \chi^{(2)}[E(t)]^2 = P^{(2)}(t).$$

which is true only if $\chi^{(2)} = 0$. Similarly, all other higher-order even susceptibility terms vanish for centrosymmetric media like atomic vapor.

Different nonlinear processes due to third-order optical nonlinearity, $\chi^{(3)}$ include four-wave mixing, cross-phase modulation, self-phase modulation, etc. The tensor nature of $\chi^{(3)}$ and the basics of few relevant nonlinear processes are described briefly in the next sections.

2.1.1 Tensor nature of $\chi^{(3)}$

For the case of a nonlinear medium with dispersion and/or loss, the nonlinear susceptibility becomes a complex quantity. In general, $\chi_{ijkl}^{(3)}$ is a fourth-rank tensor, whose elements are the coefficients of the expression for nonlinear polarisation given by,

$$P_i^{(3)}(\omega_q) = \epsilon_0 \sum_{jkl} \chi_{ijkl}^{(3)}(\omega_q, \omega_m, \omega_n, \omega_p) E_j(\omega_m) E_k(\omega_n) E_l(\omega_p).$$

Here ijk denote the cartesian components of the fields, which define their polarisation directions. For a crystalline solid, all the 81 elements of $\chi_{ijkl}^{(3)}$ can be independent. However, the symmetry property of isotropic material reduces the number of independent components. Any component with odd number of indices under inversion transformation leads to, $T(\chi_{ijkl}^{(3)}) = -\chi_{ijkl}^{(3)}$. But isotropic material requires that the susceptibility should be the same before and after the inversion transformation. This suggests that $\chi_{ijkl}^{(3)}$ with the odd number of indices should vanish and therefore results in 21 nonzero elements for this case. Now, since all the co-ordinates are equivalent in an isotropic material, the 21 elements reduce to 4 independent components namely, $\chi_{iiii}^{(3)}$, $\chi_{iijj}^{(3)}$, $\chi_{ijij}^{(3)}$ and $\chi_{ijji}^{(3)}$. Furthermore, the rotation symmetry around k -axis implies that,

$$\chi_{iiii}^{(3)} = \chi_{iijj}^{(3)} + \chi_{ijij}^{(3)} + \chi_{ijji}^{(3)}.$$

This shows that $\chi_{ijkl}^{(3)}$ has three independent elements for the isotropic medium.

2.1.2 Self-phase modulation

Self-phase modulation (SPM) is a nonlinear optical process, in which the refractive index experienced by a light field is modified by its own intensity. A schematic of the process for a

two-level system is presented in Fig 2.1. It involves the absorption of two photons and stimulated emission of two photons from the input field. The corresponding induced polarisation due to SPM for a light field with amplitude E_s and optical frequency ω_s is given by,

$$P_{SPM}^{(3)}(\omega_s) = 3\epsilon_0\chi_{SPM}^{(3)}(\omega_s - \omega_s + \omega_s)|E_s|^2E_s.$$

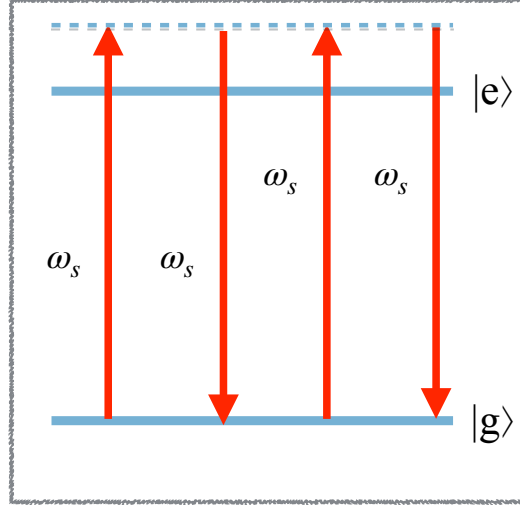


Figure 2.1: Schematic of the SPM process in a two-level system.

SPM leads to the intensity dependent refractive index given by, $n = n_0 + n_2I_s$ with n_0 being the linear refractive index, n_2I_s being the nonlinear refractive index due to SPM, $n_2 = \frac{3}{2n_0^2\epsilon_0c}\chi_{SPM}^{(3)}$ and I_s being the input light intensity.

2.1.3 Cross-phase modulation

XPM basically refers to the change in phase of a weak beam through its interaction with a strong beam in a nonlinear medium. The basic process of XPM for the case of a two-level system is presented in Fig. 2.2. The induced polarisation experienced by a weak field, $E_s e^{i(k_s z - \omega_s t)}$ due to XPM by a pump field, $E_p e^{i(k_p z - \omega_p t)}$ is given by,

$$P_{XPM}^{(3)}(\omega_s) = 3\epsilon_0\chi_{XPM}^{(3)}(\omega_p - \omega_p + \omega_s)|E_p|^2E_s.$$

It is a phase-insensitive process, unlike FWM. It leads to nonlinear gain or absorption and the intensity-dependent refractive index termed as the optical cross-Kerr effect. Here, the refractive index of the weak field depends on the frequency and intensity of the strong field and

can be mathematically expressed as, $n = n_0 + n_2 I_p$ where n_0 is the linear refractive index, $n_2 = \frac{3}{4n_0^2 \epsilon_0 c} \chi_{XPM}^{(3)}$ and I_p is the intensity of the pump beam.

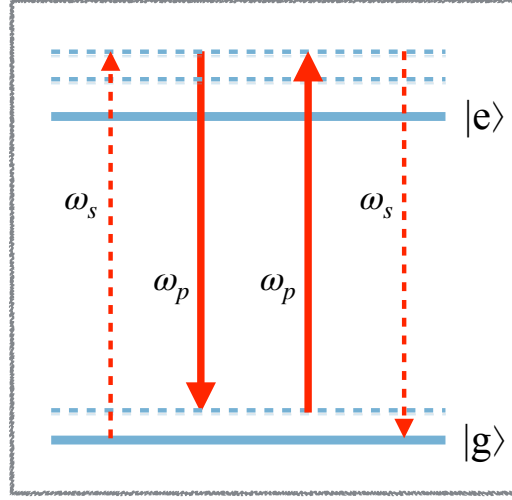


Figure 2.2: Schematic of the XPM process in a two-level system.

2.1.4 Four-wave mixing

It is a parametric third-order process, which involves the interaction of four waves in a nonlinear medium. It includes the absorption of photons from two strong fields called pump and emission of photons from two weak fields called signal fields. FWM transfers energy from the pump to the weak fields. It can be described graphically by the diagram shown in the Fig 2.3(a) demonstrated for the case of a two-level system. The process can be seeded or unseeded. In the case of seeded or stimulated FWM process, three input beams interact to generate the fourth beam. On the other hand, unseeded FWM involves the spontaneous generation of two weak fields with the input of two pump fields into the medium. In this case, vacuum fluctuation acts as a seed for the process.

Since it is a parametric process i.e. the initial and final state of the atom is same, the energy and momentum conservation are satisfied by the photons only. In general, if the interacting pump fields are $E_{pi} e^{i(k_{pi}z - \omega_{pi}t)}$ and signal fields are $E_{si} e^{i(k_{si}z - \omega_{si}t)}$ $i = 1, 2$, then the polarisation induced due to FWM process is given by,

$$P_{FWM}^{(3)}(\omega_{s2}) = 3\epsilon_0 \chi_{FWM}^{(3)}(\omega_{p1} - \omega_{s1} + \omega_{p2}) E_{p1} E_{p2} E_{s1}^* e^{i(k_{p1} + k_{p2} - k_{s1})z}.$$

The energy conservation implies $\omega_{p1} + \omega_{p2} = \omega_{s1} + \omega_{s2}$ and momentum conservation or phase matching condition implies $\vec{k}_{p1} + \vec{k}_{p2} = \vec{k}_{s1} + \vec{k}_{s2}$.

When the frequencies of all the interacting fields are different, it is called non-degenerate FWM whereas it is termed as degenerate when two of the four frequencies coincide. There are two geometries of FWM, i.e. forward and backward geometries as illustrated in Fig 2.3(b) and (c). In backward geometry, both the pump fields are counterpropagating to each other and phase-matching implies the weak fields also to be counter-propagating to each other. In the forward geometry, all the waves travel in the same forward direction and a single pump provides two photons for the process (degenerate FWM).

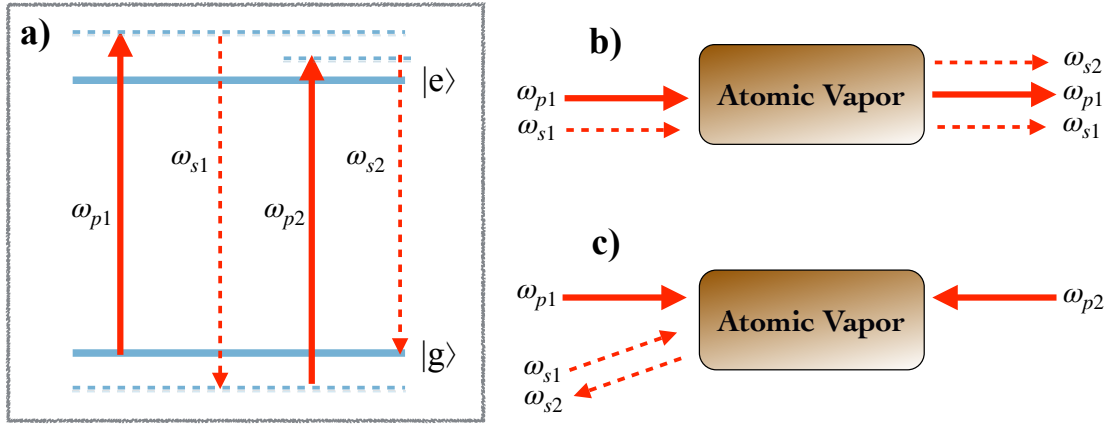


Figure 2.3: a) Schematic of the FWM process in a two-level system. b) Forward geometry and c) backward geometry of FWM.

2.2 Wave equation for Nonlinear medium

To derive the propagation equations of light through a nonlinear medium, let's consider the Maxwell's equations for a medium with no free charge and free current given as,

$$\nabla \cdot \mathbf{D} = 0, \quad (2.1)$$

$$\nabla \cdot \mathbf{B} = 0, \quad (2.2)$$

$$\nabla \times \mathbf{E} = -\frac{\partial \mathbf{B}}{\partial t}, \quad (2.3)$$

$$\nabla \times \mathbf{H} = \frac{\partial \mathbf{D}}{\partial t}. \quad (2.4)$$

Here \mathbf{E} , \mathbf{D} , \mathbf{B} and \mathbf{H} are electric field, electric displacement, magnetic field and magnetic induction respectively, where $\mathbf{B} = \mu_0 \mathbf{H}$ for the case of non-magnetic medium. Here, ϵ_0 and μ_0

are the electric permittivity and magnetic permeability of free space such that $c = \frac{1}{\sqrt{\epsilon_0\mu_0}}$.

Taking curl of equation (2.3) and replacing $\nabla \times \mathbf{B}$ by $\mu_0 \frac{\partial \mathbf{D}}{\partial t}$, we get

$$\nabla \times \nabla \times \mathbf{E} + \mu_0 \frac{\partial^2 \mathbf{D}}{\partial t^2} = 0. \quad (2.5)$$

From vector calculus, $\nabla \times \nabla \times \mathbf{E} = \nabla(\nabla \cdot \mathbf{E}) - \nabla^2 \mathbf{E}$ and $\nabla \cdot \mathbf{E}$ vanishes when \mathbf{E} is of the form of a transverse, infinite plane wave in nonlinear optics regime. So, equation (2.5) reduces to

$$\nabla^2 \mathbf{E} - \frac{1}{\epsilon_0 c^2} \frac{\partial^2 \mathbf{D}}{\partial t^2} = 0 \quad (2.6)$$

The electric displacement \mathbf{D} is related to \mathbf{E} by $\mathbf{D} = \epsilon_0 \mathbf{E} + \mathbf{P}$ with \mathbf{P} being the polarisation induced in the medium, which has both linear and nonlinear parts, i.e. $\mathbf{P} = \mathbf{P}^{(1)} + \mathbf{P}^{NL}$. So equation (2.6) can be rewritten as,

$$\nabla^2 \mathbf{E} - \frac{1}{\epsilon_0 c^2} \frac{\partial^2 \mathbf{D}^{(1)}}{\partial t^2} = \frac{1}{\epsilon_0 c^2} \frac{\partial^2 \mathbf{P}^{NL}}{\partial t^2}. \quad (2.7)$$

Here $\mathbf{D}^{(1)} = \epsilon_0 \mathbf{E} + \mathbf{P}^{(1)} = \epsilon_0 \epsilon^{(1)} \cdot \mathbf{E}$ with $\epsilon^{(1)}$ being the complex dielectric tensor for the general case of dissipative system. Further writing \mathbf{E} and \mathbf{P}^{NL} in terms of the amplitude and frequency i.e. $\mathbf{E}(r, t) = \mathbf{E}(r)e^{-i\omega t} + c.c$ and $\mathbf{P}^{NL}(r, t) = \mathbf{P}^{NL}(r)e^{-i\omega t} + c.c$, the wave equation becomes

$$\nabla^2 \mathbf{E}(r) - \frac{\omega^2}{c^2} \epsilon^{(1)} \cdot \mathbf{E}(r) = \frac{\omega^2}{\epsilon_0 c^2} \mathbf{P}^{NL}(r). \quad (2.8)$$

The nonlinear polarization acts as a source term in the wave equation and its effect on the propagation of the light fields can be studied by solving the above equation by incorporating nonlinear polarisation terms due to relevant processes.

2.3 Transverse modes of light

Modes of light are the orthogonal solutions of the light propagation equation and can be categorized into i) spatial modes, which are transverse to the direction of propagation of light and ii) temporal modes along the propagation of light. Transverse modes are a result of light confined to a waveguide such as optical fiber or laser resonator, where the shape of the modes is determined by diffraction and boundary condition.

2.3.1 Gaussian mode

Gaussian mode is the fundamental transverse electromagnetic mode (TEM_{00}) and is a solution to the paraxial Helmholtz equation. The complex amplitude of the Gaussian mode is given by [4],

$$U_{l,m}(\rho, \phi, z) = A_0 \left[\frac{w_0}{w(z)} \right] e^{-\frac{\rho^2}{w^2(z)}} e^{-ikz - ik\frac{\rho^2}{2R(z)} + i\zeta(z)}. \quad (2.9)$$

Here, A_0 is a constant, w_0 is the beam waist (minimum beam radius at $z = 0$), $w(z) = w_0 \sqrt{1 + \left(\frac{z}{z_0}\right)^2}$, $z_0 = \frac{\pi w_0^2}{\lambda}$ is the Rayleigh range, $R(z) = z \left[1 + \left(\frac{z_0}{z}\right)^2\right]$ is the radius of curvature and $\zeta(z) = \tan^{-1} \frac{z}{z_0}$ is the Guoy phase.

The intensity pattern follows a Gaussian function with its peak at $\rho = 0$. The FWHM (Full width half maxima) is related to the beam radius as, $w(z)\sqrt{2 \ln 2}$. Since Gaussian mode can be focused as the minimum spot size, it is usually the desirable output mode of most of the lasers.

2.3.2 Hermite-Gaussian modes

If the resonator has rectangular symmetry, then the solutions of the Paraxial Helmholtz equation gives Hermite-Gaussian (HG) modes. These modes form a complete set of solutions i.e. any other solution can be expressed as linear superposition of these modes. The complex amplitude of the HG beam is given by,

$$U_{l,m}(\rho, \phi, z) = A_{l,m} \left[\frac{w_0}{w(z)} \right] G_l \left(\frac{\sqrt{2}x}{w(z)} \right) G_m \left(\frac{\sqrt{2}y}{w(z)} \right) e^{-ikz - ik\frac{x^2+y^2}{2R(z)} + i(l+m+1)\zeta(z)}. \quad (2.10)$$

Here, $G_l(u) = H_l(u)e^{-\frac{u^2}{2}}$ with H_l being the Hermite polynomial of order l and $A_{l,m}$ is a constant.

Fig. 2.4 depicts the intensity patterns of a few low-order HG modes. A Gaussian mode is the lowest order mode and the only circularly symmetric mode among the HG modes which have otherwise rectangular symmetry about the propagation axis.

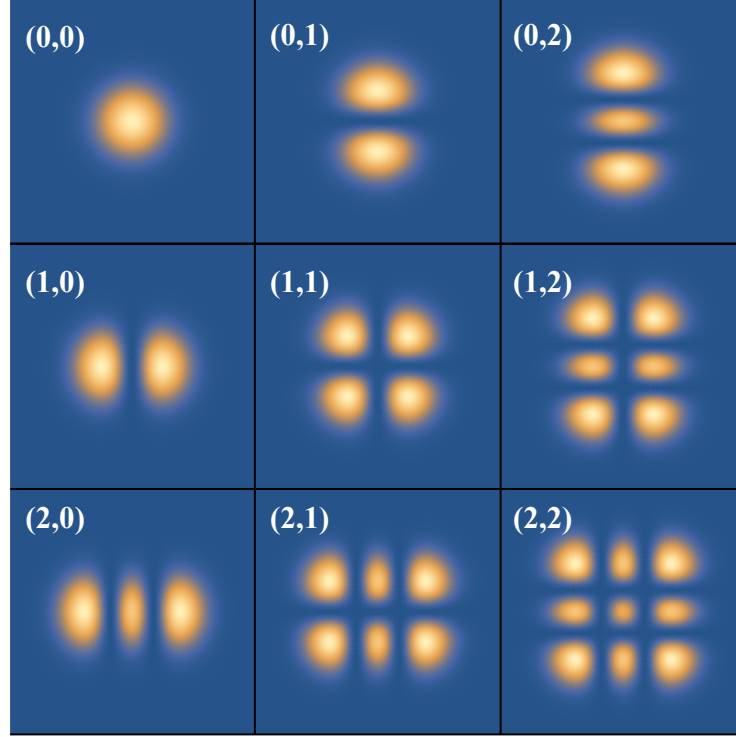


Figure 2.4: a) HG modes with index (l,m) .

2.3.3 Laguerre-Gaussian modes

The modes of a circularly symmetric resonator are described by the Laguerre-Gaussian (LG) modes. Similar to HG modes, LG modes also form a complete set of solutions. These modes exhibit cylindrical symmetry about the propagation axis and carry orbital angular momentum intrinsically. The LG modes can be generated by modulating the phase of a Gaussian beam and it is typically done using spiral phase plate, holographic plate or vortex retarder. The complex amplitude of the LG beam is given by,

$$U_{l,m}(\rho, \phi, z) = A_{l,m} \left[\frac{w_0}{w(z)} \right] \left(\frac{\rho}{w(z)} \right)^l L_m^l \left(\frac{2\rho^2}{w^2(z)} \right) e^{-\frac{\rho^2}{w^2(z)}} e^{-ikz - ik\frac{\rho^2}{2R(z)} - il\phi + i(l+2m+1)\zeta(z)}. \quad (2.11)$$

Here L_m^l is the generalised Laguerre-Gaussian function. The lowest order LG mode ($l = 0, m = 0$) is a Gaussian mode. The intensity patterns of several LG modes are presented in Fig. 2.5.

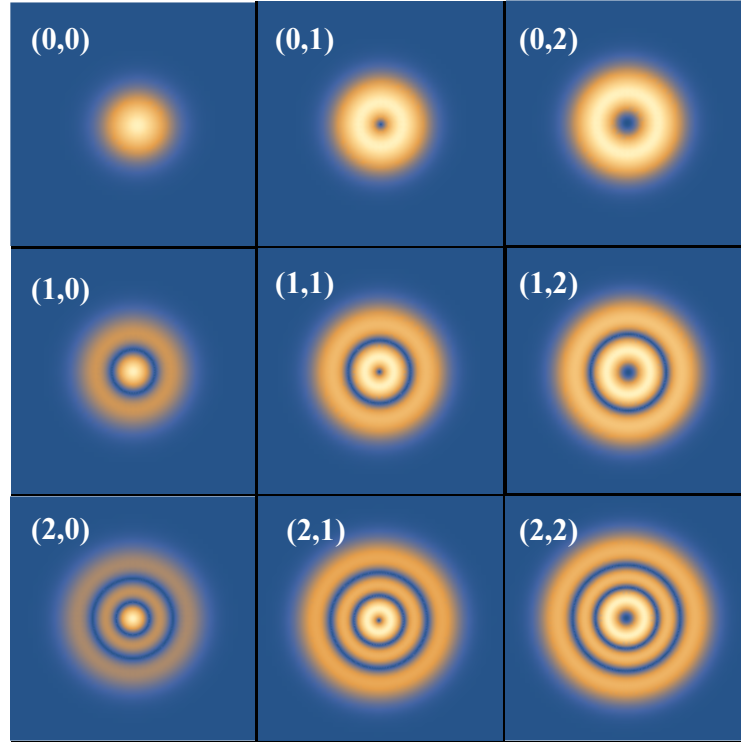


Figure 2.5: a) LG modes with index (l,m) .

2.4 Semiclassical model of basic atom-light interaction (Two-level system)

The results presented in the thesis due to the interaction of Rubidium atoms with laser can be well understood with a semiclassical model. In this case, the atom is treated quantum mechanically whereas the laser is treated as a classical electromagnetic field.

We start with the simplest case of a two-level system interacting with a laser field, which has been extensively studied [1]. This system, being largely dominated by the linear optical response, is not suitable to study nonlinear effects at the low light level.

The schematic of the two-level system is shown in Fig. 2.6. It consists of a ground state with energy E_g and an excited state with energy E_e such that $E_e - E_g = \hbar\omega_0$. The system is acted upon by a laser of frequency ω , which is detuned from the atomic transition frequency by Δ . The bare Hamiltonian (\hat{H}_0) is thus given as, $\hbar\omega_0|e\rangle\langle e|$. Within the dipole approximation i.e. when the electric field (E) does not vary rapidly over the length scale of the atom, the laser couples the states via the dipole moment operator $\hat{\mu}$ with elements, $\langle i|\hat{\mu}|j\rangle$. The interaction Hamiltonian is given by, $\hat{H}_{\text{int}} = -\hat{\mu} \cdot \mathbf{E}$, where \mathbf{E} is the applied electric field amplitude. Since

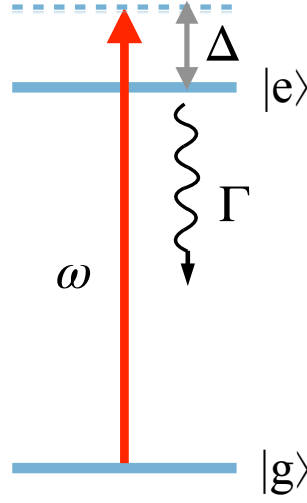


Figure 2.6: Schematic of two-level atomic system coupled by a laser field of optical frequency ω detuned by Δ from the atomic transition. The spontaneous decay rate of the excited state, $|e\rangle$ to the ground state, $|g\rangle$ is Γ .

$\hat{\mu}$ is the dipole moment induced by the applied electric field, it would be in the same direction as E leading to $\hat{H}_{\text{int}} = -\hat{\mu}E$ with $E = E_0e^{-i\omega t} + c.c.$ So, the total Hamiltonian of the coupled system is $\hat{H} = \hat{H}_0 + \hat{H}_{\text{int}}$. In matrix form,

$$\hat{H} = \begin{pmatrix} 0 & -\mu_{ge}(E_0e^{-i\omega t} + c.c.) \\ -\mu_{eg}(E_0e^{-i\omega t} + c.c.) & -\hbar\Delta \end{pmatrix}.$$

2.4.1 Rotating frame transformation

It corresponds to a unitary transformation of the system into a rotating frame such that the Hamiltonian becomes stationary and time-independent in the rotating frame. In this case, the rapidly oscillating terms in the Hamiltonian are neglected, which is valid when the applied laser is near resonance to the atomic transition i.e. $\Delta \ll \omega + \omega_0$. For two-level system, the corresponding unitary operator is given by,

$$\hat{U} = \begin{pmatrix} 1 & 0 \\ 0 & e^{-i\omega t} \end{pmatrix}.$$

The transformed Hamiltonian in the rotating frame is given by,

$$\begin{aligned} \hat{\hat{H}} &= \hat{U}^\dagger \hat{H} U - i\hbar \hat{U}^\dagger \frac{dU}{dt} \\ &= \frac{1}{2} \begin{pmatrix} 0 & -\mu_{ge}E_0^*(1 + e^{-2i\omega t}) \\ -\mu_{eg}E_0(1 + e^{2i\omega t}) & -2\hbar\Delta \end{pmatrix}. \end{aligned}$$

Neglecting the rapidly oscillating terms and using the definition of Rabi frequency, $\Omega = \frac{2\mu_{eg}E_0}{\hbar}$, the time-independent Hamiltonian reads as,

$$\hat{H} = -\frac{\hbar}{2} \begin{pmatrix} 0 & \Omega^* \\ \Omega & 2\Delta \end{pmatrix}.$$

2.4.2 Dressed states picture and Light shift

The dressed states are the eigenstates of the Hamiltonian corresponding to the coupled atom-light system. This implies that the probability to be in any of the atomic states is constant in time. In case of two-level system, the energy eigenvalues of the coupled Hamiltonian, \tilde{H} are $E_{\pm} = -\frac{\hbar}{2}(\Delta \pm \Omega')$, where $\Omega' = \sqrt{\Delta^2 + |\Omega|^2}$ is the effective Rabi frequency. The corresponding eigenstates are given by,

$$|+\rangle = \sin \frac{\theta}{2} e^{-i\phi} |g\rangle + \cos \frac{\theta}{2} |e\rangle, \quad (2.12)$$

$$|-\rangle = \cos \frac{\theta}{2} e^{-i\phi} |g\rangle - \sin \frac{\theta}{2} |e\rangle. \quad (2.13)$$

Here, we have used $\Delta = \Omega' \cos \theta$, $|\Omega| = \Omega' \sin \theta$ and ϕ is the phase associated with the Rabi frequency. These eigenstates are called as the dressed states and they are superpositions of the uncoupled bare states. The probability of finding the atom in the state $|g\rangle$ is given by, $|\langle g|\pm\rangle|^2 = \frac{\Omega' \pm \Delta}{2\Omega'}$, which is indeed constant in time. The energy eigenvalues for different laser detunings for bare and dressed states are presented in Fig. 2.7. The bare atomic eigenvalues without coupling are represented by the dotted lines with a crossing whereas the red solid lines in Fig. 2.7 refer to the eigenvalues of the coupled system. The energy shift in the case of the coupled system is known as the AC stark shift [2]. The excited state shift is equal in magnitude and opposite in sign of the ground state shift.

Consider the case of exact resonance ($\Delta = 0$), the states are degenerate without coupling. However, in the presence of coupling to a laser field, the energy levels are shifted with eigenvalues $E_{\pm} = \mp \frac{\hbar|\Omega|}{2}$. The light shift, in this case, is $\frac{\hbar|\Omega|}{2}$ as shown in Fig. 2.7. The eigenstates are found to be equal superpositions of the bare states given by,

$$|+\rangle = \frac{1}{\sqrt{2}}(|g\rangle + |e\rangle), \quad (2.14)$$

$$|-\rangle = \frac{1}{\sqrt{2}}(|g\rangle - |e\rangle). \quad (2.15)$$

For far detuned case i.e. $\Delta \gg |\Omega|$, the effective Rabi frequency, Ω' is approximated as,

$$\Omega' = \sqrt{\Delta^2 + |\Omega|^2} = |\Delta| \left(1 + \frac{|\Omega|^2}{\Delta^2}\right)^{1/2} \approx |\Delta| \left(1 + \frac{|\Omega|^2}{2\Delta^2}\right). \quad (2.16)$$

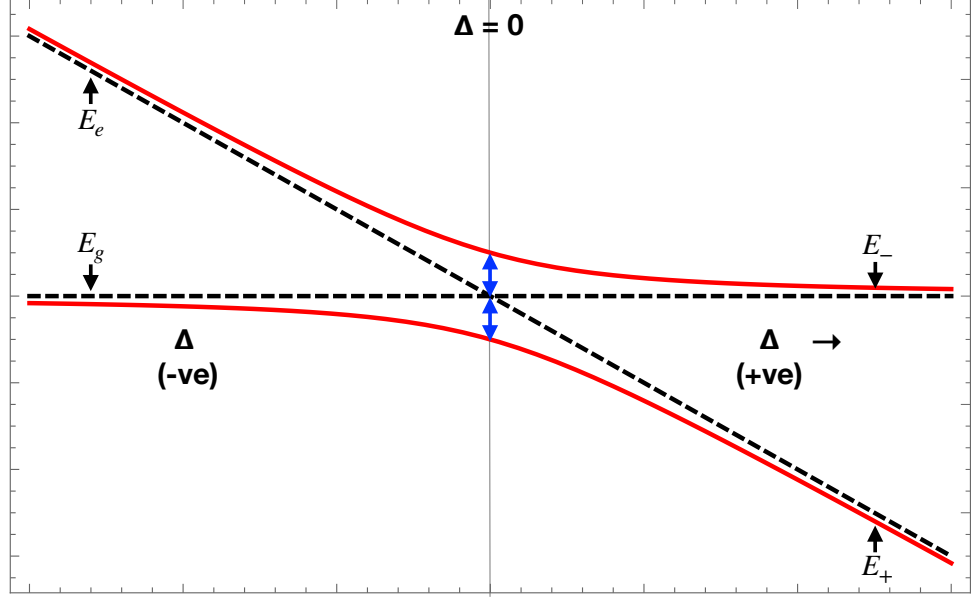


Figure 2.7: Energy level diagram for bare and dressed atomic states. The dotted lines correspond to the energies corresponding to the bare states whereas the red solid lines refer to the energies corresponding to the dressed states.

Hence, the energy eigenvalues are approximated to, $E_+ = -\hbar(\Delta + \frac{|\Omega|^2}{4\Delta})$ and $E_- = \hbar\frac{|\Omega|^2}{4\Delta}$. The energy shifts of the states are given by, $\Delta E_g = E_- - E_g = \frac{\hbar|\Omega|^2}{4\Delta}$ and $\Delta E_e = E_+ - E_e = -\frac{\hbar|\Omega|^2}{4\Delta}$. The shifts being proportional to the light intensity are termed as the light shifts. The dressed states in this case approximate to the bare atomic states as shown in Fig. 2.7 and are mathematically represented as,

$$|+\rangle \approx (|e\rangle + \frac{|\Omega|}{2\Delta}|g\rangle), \quad (2.17)$$

$$|-\rangle \approx (|g\rangle - \frac{|\Omega|}{2\Delta}|e\rangle). \quad (2.18)$$

2.4.3 Effect of Relaxation processes

The Hamiltonian \tilde{H} describes the interaction of the atom with applied electromagnetic field. However, the atom also couples with the vacuum field leading to spontaneous emission. This process further results in decoherence in the system by dipole dephasing. The time evolution of the system with relaxation processes is governed by the Lindblad master equation as,

$$\frac{d\hat{\rho}}{dt} = -\frac{i}{\hbar}[\hat{H}, \hat{\rho}] + \hat{\mathcal{L}}_D. \quad (2.19)$$

Here $\hat{\mathcal{L}}_D$ contains the terms related to population decays and dephasing present in the system. Mathematically, $\hat{\mathcal{L}}_D$ is given by,

$$\hat{\mathcal{L}}_D = \sum_{if} \Gamma_{if} [\hat{C}_{if} \hat{\rho} \hat{C}_{if}^\dagger - \frac{1}{2} (\hat{\rho} \hat{C}_{if} \hat{C}_{if}^\dagger + \hat{C}_{if} \hat{C}_{if}^\dagger \hat{\rho})],$$

where $\hat{C}_{if} = |f\rangle\langle i|$ and Γ_{if} is the decay rate of the state from $|i\rangle$ to $|f\rangle$. Since for two-level system, we have a single decay channel Γ_{eg} , the expression for \mathcal{L}_D becomes,

$$\hat{\mathcal{L}}_D = \begin{pmatrix} \Gamma_{eg} \tilde{\rho}_{ee} & -\frac{\Gamma_{eg}}{2} \tilde{\rho}_{ge} \\ -\frac{\Gamma_{eg}}{2} \tilde{\rho}_{eg} & -\Gamma_{eg} \tilde{\rho}_{ee} \end{pmatrix}.$$

2.4.4 The optical Bloch equations

Using the Lindblad master equation, the optical Bloch equations for the two-level system can be expressed as,

$$\dot{\tilde{\rho}}_{ee} = \frac{i}{2} (\Omega \tilde{\rho}_{ge} - \Omega^* \tilde{\rho}_{eg}) - \Gamma_{eg} \tilde{\rho}_{ee}, \quad (2.20)$$

$$\dot{\tilde{\rho}}_{eg} = \frac{i}{2} [\Omega (\tilde{\rho}_{gg} - \Omega^* \tilde{\rho}_{ee}) + 2\Delta \tilde{\rho}_{ge}] - \frac{\Gamma_{eg}}{2} \tilde{\rho}_{eg}. \quad (2.21)$$

Here, $\tilde{\rho}_{gg} + \tilde{\rho}_{ee} = 1$ and $\tilde{\rho}_{ge} = \tilde{\rho}_{eg}^*$. The solution of the equations under steady state condition ($t \rightarrow \infty$) is given by,

$$\tilde{\rho}_{ee} = \frac{|\Omega|^2}{4\Delta^2 + 2|\Omega|^2 + \Gamma_{eg}^2}, \quad (2.22)$$

$$\tilde{\rho}_{eg} = -\frac{2\Omega(2\Delta - i\Gamma_{eg})}{4\Delta^2 + 2|\Omega|^2 + \Gamma_{eg}^2}. \quad (2.23)$$

Now, in the rotating frame, the induced polarization or dipole moment ($\hat{\mu}$) per unit volume in the medium is related to $\tilde{\rho}_{eg}$, $\tilde{\mu}$ and number density of atoms (N) as,

$$\tilde{P} = N \langle \hat{\mu} \rangle = N \text{Tr}(\hat{\rho} \hat{\mu}). \quad (2.24)$$

In the lab frame, the polarization can be written as,

$$P(t) = \tilde{P} e^{-i\omega t} + c.c. = N(\mu_{ge} \rho_{eg} e^{-i\omega t} + c.c.). \quad (2.25)$$

The polarization can also be expressed in terms of susceptibility (χ) as,

$$P(t) = \epsilon_0 \chi E_0 (e^{-i\omega t} + c.c.). \quad (2.26)$$

Comparing the complex amplitudes in equations 2.25 and 2.26,

$$\chi = \frac{2N|\mu_{ge}|^2}{\epsilon_0\hbar\Omega} \tilde{\rho}_{eg}. \quad (2.27)$$

Using the definition of complex refractive index, $n = n_R + in_I = \sqrt{(1 + \chi)} \approx 1 + \frac{1}{2}(\chi_R + i\chi_I)$, we get, $n_R = 1 + \frac{\chi_R}{2}$ and $n_I = \frac{\chi_I}{2}$. So, the real part of the susceptibility provides information about the dispersion induced in the medium due to atom-light interaction. The electric field amplitude in terms of the complex n becomes, $E(z) = E_0 e^{i(n_R kz - \omega t)} e^{n_I kz}$, where a positive $n_I (= \frac{\chi_I}{2})$ leads to an exponential decay of amplitude. Hence, the imaginary part of susceptibility gives information about the absorption of input light in the medium by the relation $I = I_0 e^{-\chi_I kz}$, where I_0 and I are the input and transmitted intensity of light. $\text{Re}(\chi)$ and $\text{Im}(\chi)$ for two level system for the case of cold atomic ensemble are presented in Fig. 2.8 (a) and (b) respectively.

2.4.5 Doppler broadening

The experiments of the thesis are performed in thermal atomic vapor, in which the atoms can not be considered to be stationary. The atoms, in this case, follow the Maxwell-Boltzmann velocity distribution. Mathematically, the distribution of velocities along z direction can be expressed as, $P(v_z) = \frac{1}{\sqrt{2\pi}v_p} e^{-v_z^2/2v_p^2}$ with $\int_{-\infty}^{\infty} P(v_z) dv_z = 1$, where $v_p = \sqrt{k_B T/m}$ is the most probable velocity of the atoms and it defines the width of the distribution function. Here, k_B is the Boltzmann constant, T is the temperature of the vapor and m is the atomic mass.

To include the effect of velocities of the atoms, the laser frequency for the case of a two-level system is Doppler shifted by, $\omega' = \omega + kv_z$. The susceptibility then becomes a function of v_z and it is averaged over all velocities of the distribution. Mathematically, it is expressed as, $\int_{-\infty}^{\infty} \chi(v_z) P(v_z) dv_z$. The Doppler width for the case of a two-level system interacting with one laser is found to be much larger as compared to the natural linewidth of the system. However, for systems with multiple atomic levels and laser beams, the Doppler broadening plays a more complex role.

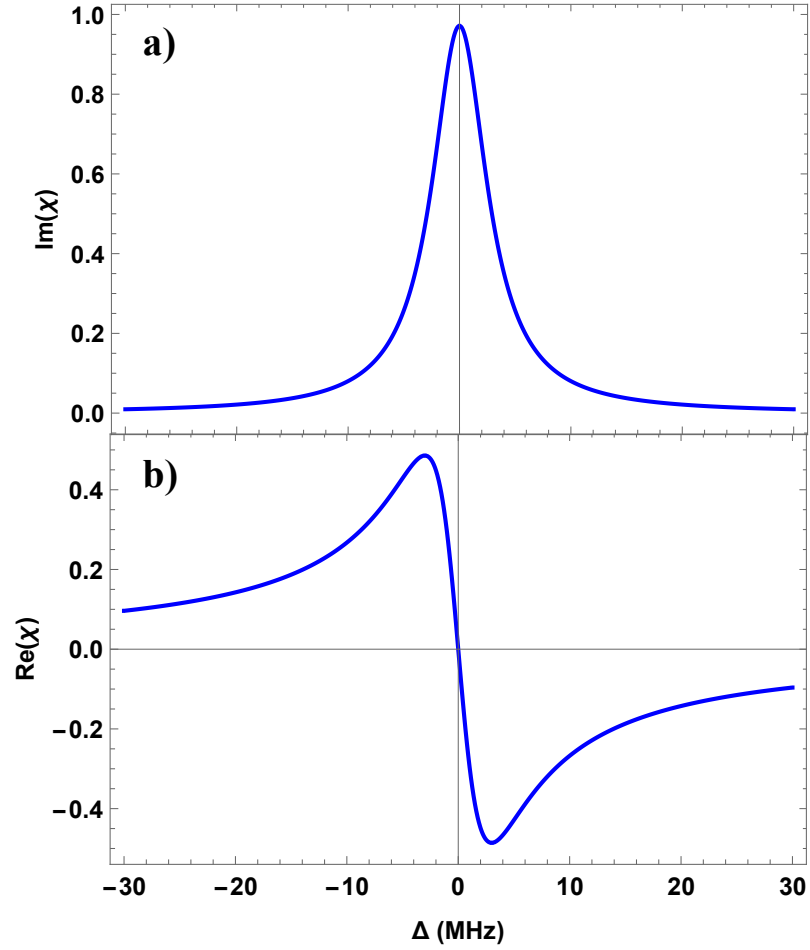


Figure 2.8: a) $\text{Im}(\chi)$ and b) $\text{Re}(\chi)$ for two-level system for atoms at rest. The parameters used are, $\Gamma = 2\pi \times 6$ MHz, $\Omega = 2\pi \times 0.1$ MHz and $N = 10^{13}\text{cm}^{-3}$.

2.5 Properties of rubidium

Rubidium is chosen for our experiments as the diode lasers corresponding to the optical transition frequencies of rubidium are readily available. It is an alkali metal with a single valence electron and a hydrogen-like atomic structure. It has two isotopes, ^{85}Rb and ^{87}Rb with 72% and 28% of relative abundance respectively.

A schematic diagram of the energy level structure of ^{85}Rb and ^{87}Rb are presented in Fig.2.9 and Fig.2.10 respectively. The coupling of the electron orbital angular momentum \mathbf{L} with the electron spin \mathbf{S} leads to the fine structure splitting, where the energy eigen states are determined by the quantum number $\mathbf{J} = |\mathbf{J}| = |\mathbf{L} + \mathbf{S}|$. The coupling of the spin-orbit angular momentum, \mathbf{J} with the nuclear spin, \mathbf{I} of the atom gives rise to the hyperfine splitting with total angular

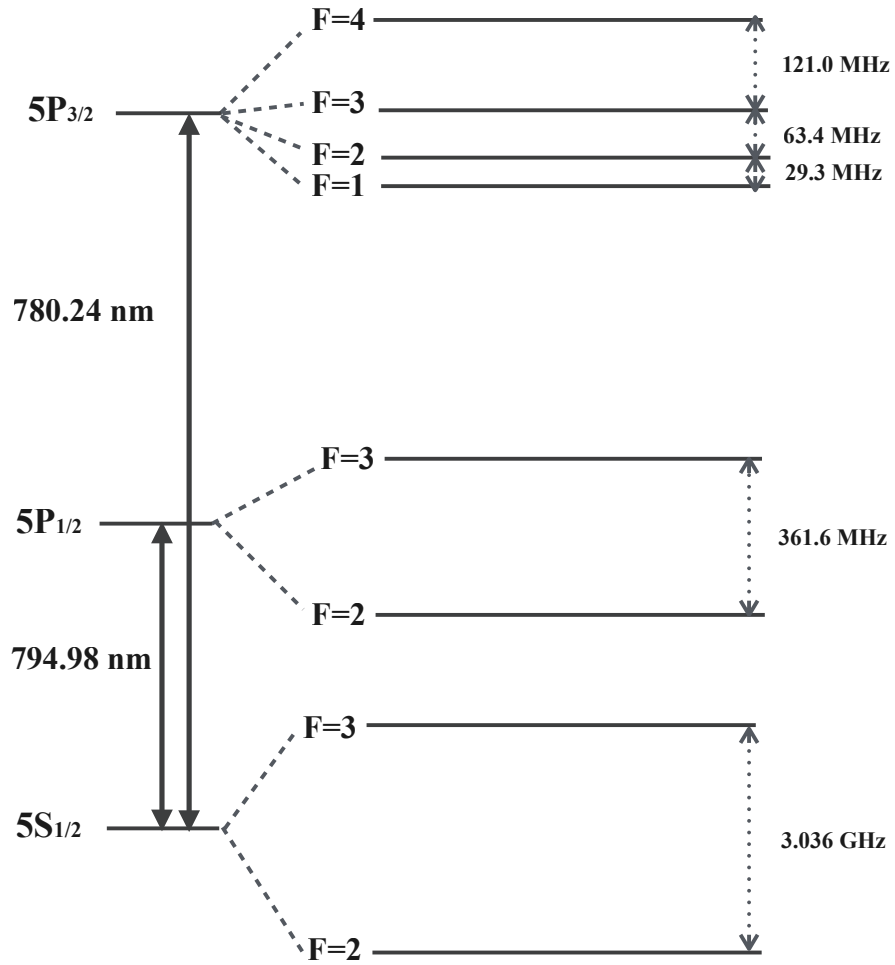


Figure 2.9: Schematic diagram of electronic energy level configuration for D_1 and D_2 lines of ^{85}Rb .

momentum, $\mathbf{F} = \mathbf{J} + \mathbf{I}$. Here the energy levels are identified by the quantum number $F = |\mathbf{F}|$ and the projection of \mathbf{F} onto the quantisation axis, m_F . For D_1 -line of ^{85}Rb with nuclear spin $I = \frac{5}{2}$, ground state ($J = \frac{1}{2}$) is split into two hyperfine states ($F = 2, 3$) and the excited state ($J = \frac{3}{2}$) is split into four hyperfine states ($F = 1, 2, 3, 4$). Similarly for ^{87}Rb with $I = \frac{3}{2}$, the hyperfine interaction leads to two ground states ($F = 2, 3$) and four excited states ($F = 0, 1, 2, 3$). For D_2 -line of ^{85}Rb with nuclear spin $I = \frac{5}{2}$, ground state ($J = \frac{1}{2}$) is split into two hyperfine states ($F = 2, 3$) and the excited state ($J = \frac{3}{2}$) is split into four hyperfine states ($F = 1, 2, 3, 4$). Similarly for ^{87}Rb with $I = \frac{3}{2}$, the hyperfine interaction leads to two ground states ($F = 2, 3$) and four excited states ($F = 0, 1, 2, 3$).

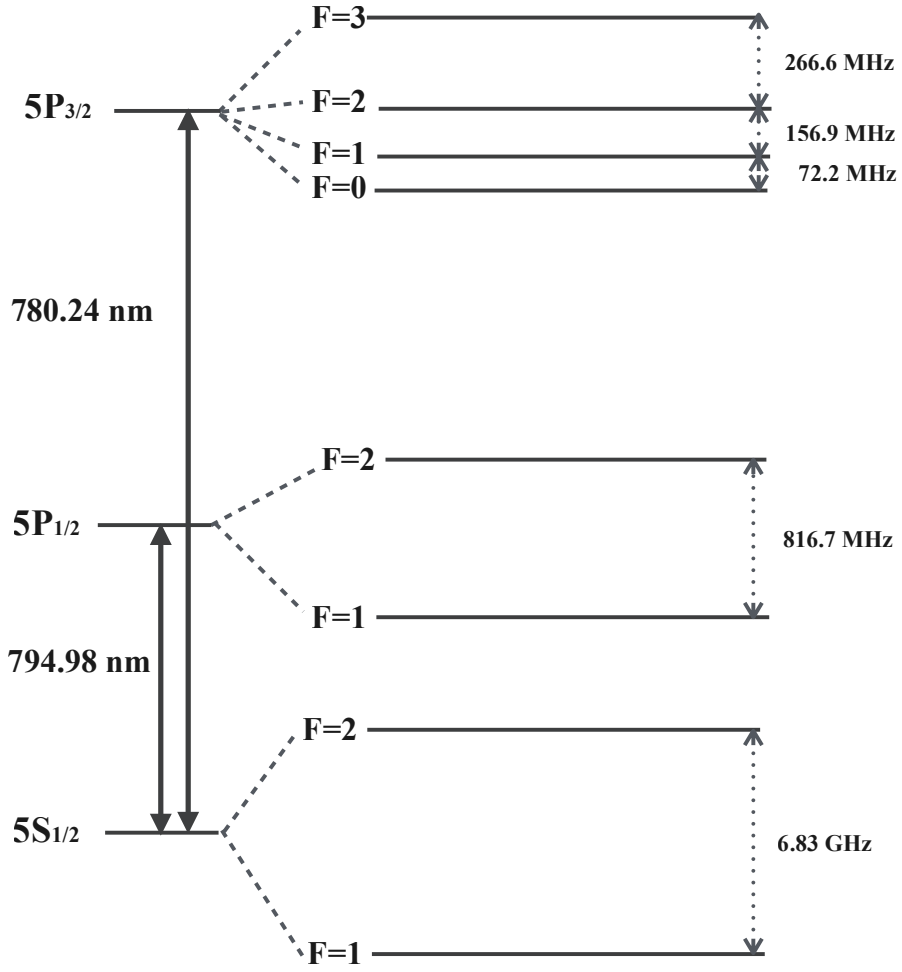


Figure 2.10: Schematic diagram of electronic energy level configuration for D_1 and D_2 lines of ^{87}Rb .

2.5.1 Zeeman effect on hyperfine states

Each hyperfine energy level characterized by the quantum number F consists of $2F + 1$ magnetic sublevels. If no external magnetic field is applied, the Zeeman sublevels of the hyperfine states are degenerate. However, in the presence of a magnetic field, the degeneracy of the Zeeman sublevels is broken. The interaction Hamiltonian, in this case, is given by,

$$\mathbf{H}_{\text{int}} = -\boldsymbol{\mu}_m \cdot \mathbf{B} = -\mu_B g_F \mathbf{F} \cdot \mathbf{B}. \quad (2.28)$$

If the magnetic field (B_z) is considered to be along z -direction, H_{int} becomes, $-\mu_B g_F F_z B_z$. Here, $\mu_B = \frac{e\hbar}{2m_e c}$ is the Bohr magneton and g_F is the hyperfine Lande g -factor given by,

$$g_F = g_J \frac{F(F+1) + J(J+1) - I(I+1)}{2F(F+1)}, \quad (2.29)$$

where g_J is the gyromagnetic ratio (Lande g-factor) defined by, $g_J = 1 + \frac{J(J+1)+S(S+1)-L(L+1)}{2J(J+1)}$. For a weak magnetic field, the energy shift in the lowest order due to the Zeeman effect is given by the expression,

$$\Delta E_{|F, m_F\rangle} = \mu_B g_F m_F B_z. \quad (2.30)$$

The splitting of the states in this regime is termed as the anomalous Zeeman effect.

2.6 Lasers

The lasers used for the experiments are solid-state lasers, which can be tuned in the range 780-785 nm. The typical linewidth of the lasers is about 100 kHz-1 MHz with a mod-hop free tuning range up to 20 GHz. For DL-Pro (TOPTICA) laser, the diode current is set to 250 mA, which delivers optical power of 150 mW. The laser beam profile, in this case, is an asymmetric Gaussian and we use a pair of anamorphic prism pairs to make it symmetric. Another laser used for the experiment is a Tapered Amplifier laser (TA-Pro, TOPTICA), which delivers a maximum optical power of 3 W. The laser beam profile of TA-Pro is not Gaussian and to improve the spatial profile, we initially used a method called spatial filtering. For this, we require a combination of lens and an aperture such that the aperture is placed at the focus of the lens to filter out the contribution from the higher-order spatial modes. In this case, the output mode is a mixture of the Gaussian and the higher-order spatial modes. Furthermore, the efficiency of the process is very low and the high intensity of the laser at the focus leads to damage to the aperture.

Since we got very little efficiency in spatial filtering, hence we use optical fiber for mode cleaning. The polarization in the fiber is maintained using a combination of a half-wave plate and a quarter-wave plate as mentioned in reference [3]. Sometimes, only a half-wave plate is sufficient for the polarisation alignment.

2.7 Saturated absorption spectroscopy

Spectroscopy is inevitable for laser frequency reference in atomic physics experiments. At room temperature, the transition lines are highly broadened due to the Doppler effect and hence the frequencies can not be measured accurately. However, saturated absorption spectroscopy enables precise spectroscopy of the atomic system without the requirement of cooling down

the system. It is a technique to resolve the hyperfine lines buried within the Doppler width. In this case, the frequency measurement is only limited by the lifetime of the excited state.

The technique uses two counter-propagating beams; one strong beam called the pump beam and a weak beam called the probe beam. The pump beam is strong enough to saturate the optical transition such that the population in both the ground state and the excited state are approximately equal. When the probe beam traverses the medium, it interacts with the atoms in the excited state and undergoes stimulated emission. This leads to a peak at the hyperfine resonance in the probe transmission signal. The counter-propagation helps in the interaction of both the beams with the same velocity group of atoms.

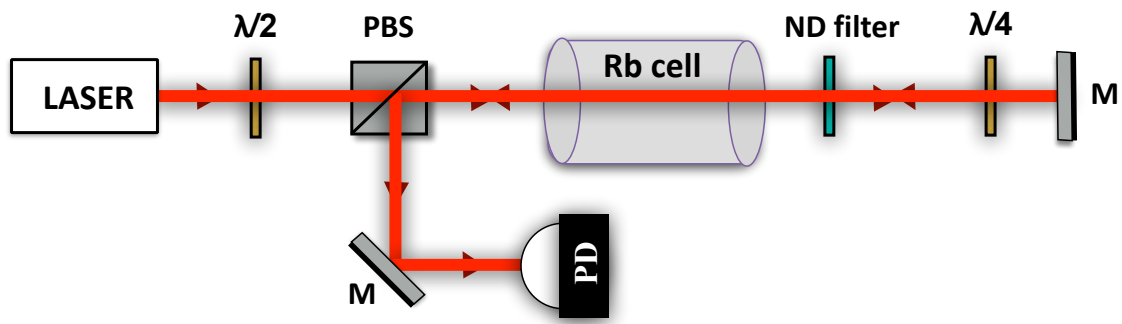


Figure 2.11: Experimental setup for saturated absorption spectroscopy. M: Mirror, PBS: Polarising beam splitter, PD: Photodetector.

The experimental setup for the saturated absorption spectroscopy is presented in Fig.2.11. Here the laser beam is passed through a combination of PBS and a $\frac{\lambda}{2}$ plate to control the input intensity into the Rb cell. The input beam is retroreflected through the cell using a mirror. A neutral density (ND) filter is put after the cell such that the retro-reflected beam will have a lower intensity than the pump beam and hence will act as a weak probe beam. Furthermore, a $\frac{\lambda}{4}$ plate is put on the path of the beam such that it acts as a $\frac{\lambda}{2}$ plate for the probe beam, which is double-passed through it by retroreflection. The angle of this to be orthogonally polarised to the pump beam so that it can be filtered out to be collected using a photodetector and analyzed in an oscilloscope.

The spectroscopy signal recorded for Rubidium D_2 line using a 10 cm vapor cell at room temperature (25^0 C) is presented in Fig. 2.12. Here we have shown the expanded view of the $F = 3 \rightarrow F'$ transition as an inset of the figure. The dipole selection rule ($\Delta F = 0 \pm 1$) implies that there are three possible dipole-allowed transitions in this case, namely $F = 3 \rightarrow$

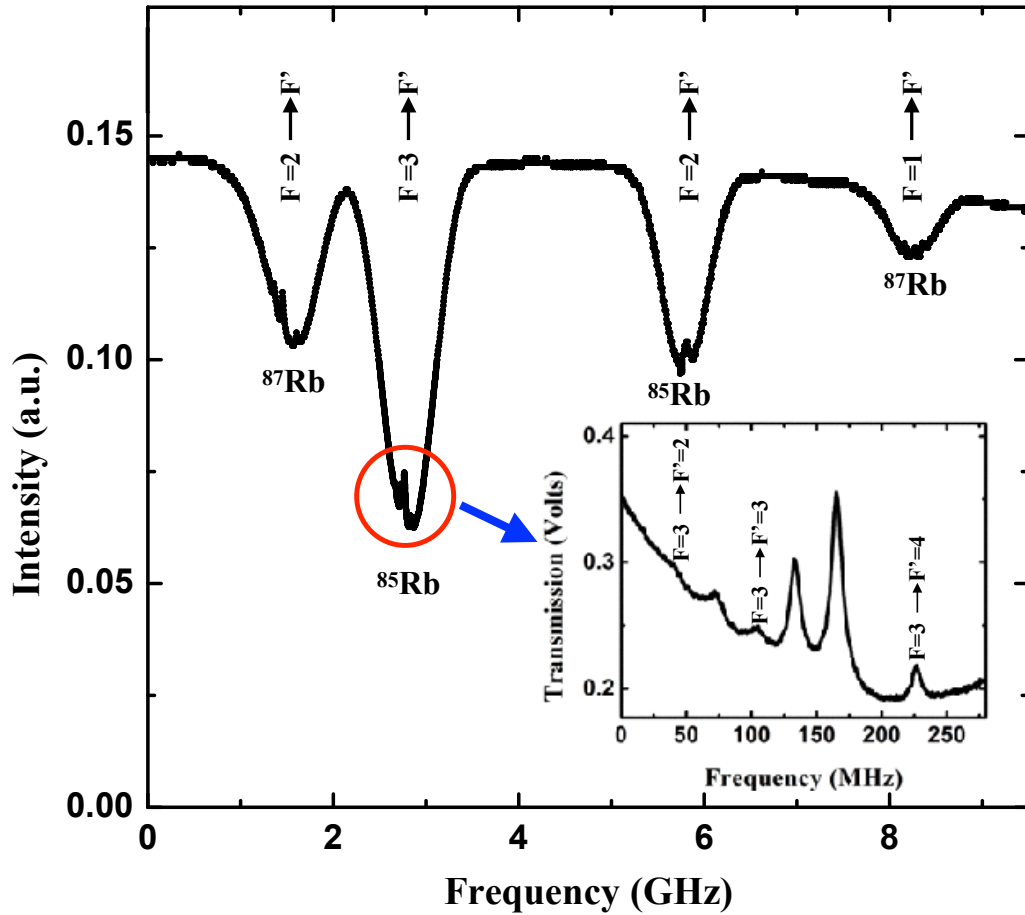


Figure 2.12: Experimentally recorded saturation absorption spectroscopy.

$F' = 2, 3, 4$. However, the inset shows three additional transition lines apart from the atomic transitions and these are called the cross-over resonances. These resonances occur when two transitions are within a Doppler profile sharing a common ground state. In this case, when the laser is at the mid-frequency of the two transitions, the same velocity group of atoms will be resonant to the pump at one transition and resonant to the probe at the other transition. This results in the increased transmission of the probe leading to a cross-over resonance, which is stronger than the atomic resonances. As expected, three cross-over resonances are corresponding to the three atomic transitions as depicted in Fig 2.12. However, for the case of a multi-level system as presented here, hyperfine pumping plays a significant role in the sub-Doppler absorption spectroscopy [5]. The larger width of the spectral features, as well as the origin of the efficient cross-over resonances, are due to hyperfine pumping of the corresponding open transitions.

2.8 4-f imaging technique

It is a technique used for imaging with unit magnification. The schematic of the experimental arrangement is shown in Fig. 2.13 (a). It consists of two lenses separated by $2f$ distance and the image plane is at $4f$ distance from the object plane. It makes use of a cascade of two Fourier transforms to reconstruct an image. The first lens ($L1$) performs a Fourier transform of the object at the Fourier plane. If $f(x, y)$ is the complex amplitude of the object function, then the complex amplitude of the optical wave of wavevector k and wavelength λ at the Fourier plane is proportional to the Fourier transform of $f(x, y)$ i.e. $F(\nu_x, \nu_y)$ and is given by [4],

$$g(x, y) = \frac{i}{\lambda f} e^{-i2kf} F\left(\frac{x}{\lambda f}, \frac{y}{\lambda f}\right), \quad (2.31)$$

where, $\nu_x = \frac{x}{\lambda f}$ and $\nu_y = \frac{y}{\lambda f}$ are the spatial frequencies. Now as the coordinate system in the image plane is inverted, i.e., $(x, y) \rightarrow (-x, -y)$, the second lens ($L2$) performs inverse Fourier transform on $g(x, y)$ given by,

$$F^{-1}\{g(x, y)\} \propto f(-x, -y). \quad (2.32)$$

In this way, the image is a replica of the object. In our experiment, this technique is used to image the transverse profiles of the laser beams at the exit faces of the vapor cell without the diffraction effect. We use two lenses of the focal length of 40 cm. To check the correctness of the technique, we put a glass plate with an imprinted image at the object plane on the path of the laser beam. A CCD camera is placed at the image plane to record the replica of the image on the laser beam profile. The image of the imprinted glass plate used in the experiment is shown in Fig. 2.13 (b) whereas Fig. 2.13 (c) shows the CCD image of the laser beam profile at the image plane of the 4f-imaging system. The pattern of the glass plate is replicated in the laser beam with the diffraction of the pattern being compensated by the lens system. We also checked the laser beam waists at both the object and the image planes, which are found to be similar.

We further observed that the free space diffraction of the beam after the cell can also be studied using this technique. If the object plane is moved towards the first lens ($L1$) by a distance z , then the image plane moves away from the second lens ($L2$) by the same distance z . So the CCD camera can be translated accordingly to measure the beam diffraction. We can also achieve a different magnification of the image by using a different combination of lenses. For example, if the focal length of $L1$ is $f1$ and that of $L2$ is $f2$, then we can get an image

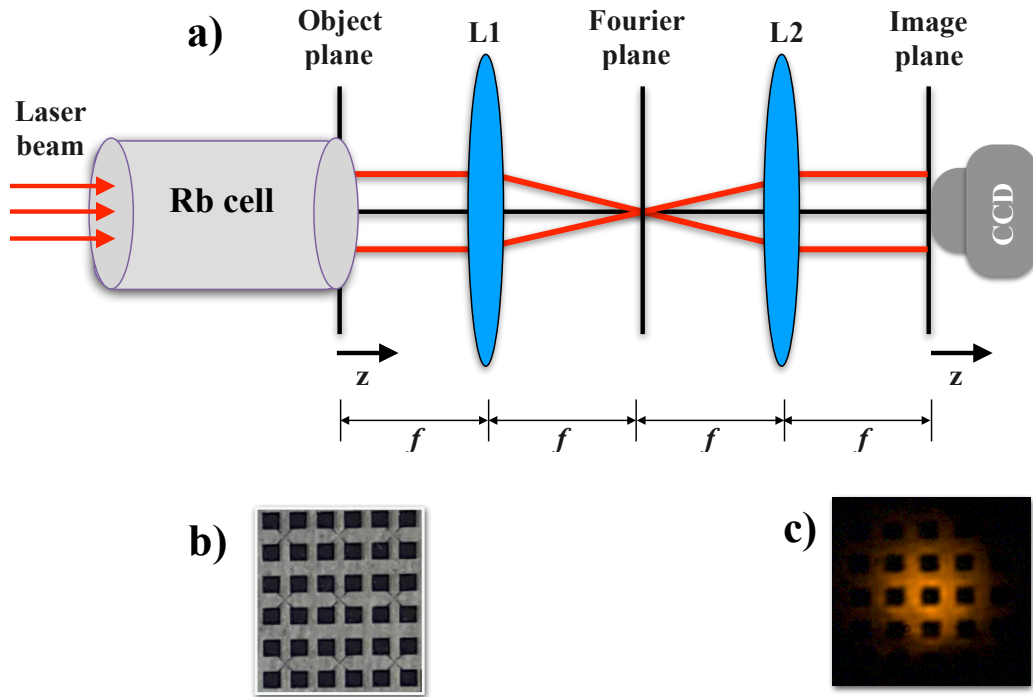


Figure 2.13: a) Schematic of 4-f imaging technique. L1, L2: Lens, f : Focal length of lens. b) Image of the imprinted glassplate. c) CCD image of the laser beam profile with the imprinted image at the image plane.

with magnification f_2/f_1 without diffraction effects. In this case, the two lenses should be separated by the distance, $f_1 + f_2$.

Bibliography

- [1] C. Cohen-Tannoudji, J. Dupont-Roc, and G. Grynberg, *Atom-Photon Interactions* (Wiley-Interscience, New York, 1998).
- [2] S. H. Autler, and C. H. Townes. *Physical Review* **100** 703 (1955).
- [3] P. Arora, A. Agarwal, and A. Sen Gupta, *Rev. of Sci. Inst.* **82**, 125103 (2011).
- [4] B. E. A. Saleh and M. C. Teich, *Fundamentals of Photonics*, 2nd ed. (Wiley, 2014).
- [5] David A. Smith and Ifan G. Hughes, *Am. J. Phys.* **72**(5) (2004).

Chapter 3

Polarization rotation of light with efficient FWM and XPM in thermal atomic vapor

Nonlinear interaction of atom and light can lead to the modification of the basic properties of the light field such as the rotation of the input Polarization state. There are extensive studies on Polarization rotation resulting from different types of processes. Polarization self-rotation (PSR) occurs when a light field with elliptical Polarization propagates through a non-linear medium in the absence of a magnetic field. This is a result of unequal ac-stark shifts due to unequal contribution from circularly-polarized components of the input field, typically observed in near-resonant atomic vapour [1–4]. PSR has an application in squeezing of electromagnetic vacuum field, which has been studied by many groups [5–9]. This non-linear phenomenon does not necessitate the presence of a magnetic field. However, when an external magnetic field is applied to the system, it induces birefringence and dichroism leading to the Polarization rotation of the input linearly polarized light field. When the magnetic field is applied in the longitudinal direction to the polarization plane of the light field, the effect is called as Faraday rotation [10] while it is called Voigt effect [11] when the magnetic field is applied in the transverse direction to the plane of polarization of the light field. In the case of a near-resonant light beam traversing the atomic vapor in presence of a magnetic field, the rotation angle and change in ellipticity depend on the strength of the magnetic field as well as the light intensity. This phenomenon is termed as the nonlinear magneto-optic rotation (NMOR). There are reports on substantial theoretical as well as experimental work based on NMOR [12–15] and it has various applications in atomic magnetometry [16, 17], atomic clocks [18] and narrow-band optical filters [19, 20].

We study the Polarization rotation of an input elliptically polarized light while passing

through thermal rubidium vapor with a magnetic noise of magnitude less than 10 mG. The input light, in this case, undergoes PSR as well as NMOR and the superimposed effect of the two will lead to the polarization rotation of the input beam. However, the same system can be alternatively studied by introducing two basic non-linear optical phenomena i.e. four-wave mixing (FWM) and cross-phase modulation (XPM) [21]. These processes are found to be enhanced by the Zeeman coherence. This work involves the theoretical as well as an experimental investigation of the induced Polarization rotation.

In this chapter, first, we present the experimental observation of efficient FWM and XPM in thermal rubidium vapor. Then we discuss the principle of Polarization rotation for the system. We also derive the probe propagation equations, where we discuss how the above nonlinear processes affect the polarization state of the input light field. The experimental method for the study of the polarization rotation of the input light field is discussed. Then the experimental results are presented along with an estimate of the nonlinearities induced in the medium.

3.1 Observation of FWM and XPM in rubidium thermal vapor

The Polarization rotation in our system depends on the efficiency of the nonlinear processes. Therefore, we experimentally investigate FWM and XPM in the thermal rubidium vapor, which in turn helps us to optimize the parameters to observe efficient Polarization rotation as well.

The experiment consists of FWM between the co-propagating pump and probe beams passing through atomic vapor as shown in Fig. 3.1(a). The pump beam is horizontally polarized with optical frequency ω and the probe beam is vertically polarized with optical frequency $\omega + \delta$. The phase-matching of the co-propagating fields leads to the generation of light at optical frequency $\omega - \delta$ along the same propagation direction. The symmetry of $\chi_{ijkl}^{(3)}$ responsible for FWM in an isotropic medium allows only an even number of indices, which implies that the Polarization of the newly generated light field is same as that of the probe field. This is also consistent with the angular momentum conservation of atom-photon interaction. One of the basic processes of FWM, as allowed by the angular momentum conservation, is depicted in Fig. 3.1(b). Here, the pump and the probe fields being π polarised and σ_- polarised respectively, the FWM process requires a change of magnetic quantum number by $2m_\pi - m_{\sigma_-} = 0 - (-1) = +1$ leading to the generation of σ_+ polarised light. A detailed numerical calculation on the dependence of

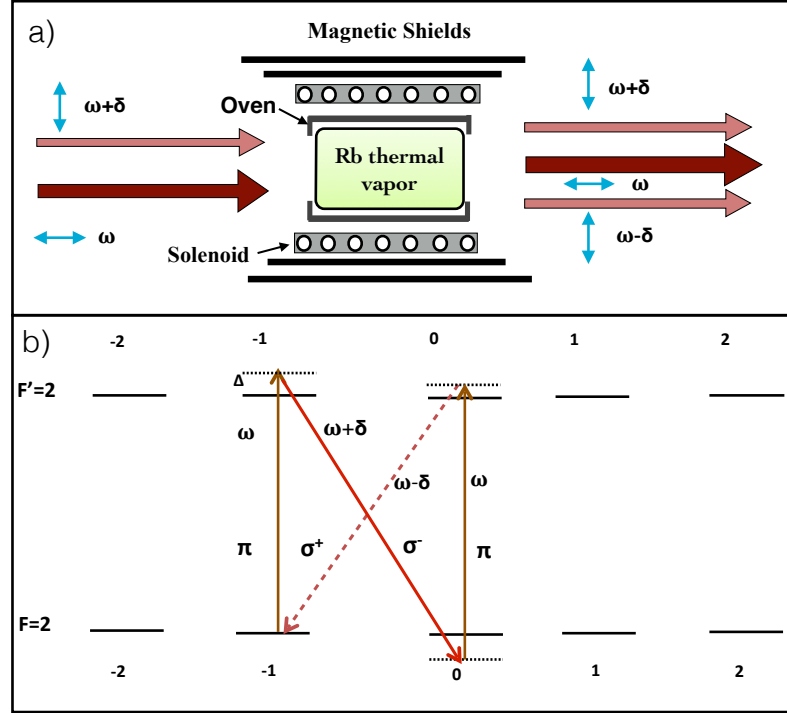


Figure 3.1: (a) Schematic of degenerate FWM for orthogonal linearly-polarized pump and probe fields. (b) Illustration of a basic process of FWM using Zeeman degenerate hyperfine sublevels.

FWM and XPM spectra on Zeeman-coherence is presented in references [22, 23].

3.1.1 Experimental setup

The detailed experimental setup for observation of FWM is presented in Fig 3.2. The input beams are derived from an external cavity diode laser of wavelength 780 nm. The frequency offset (δ) between the pump and the probe is introduced by using double-pass configurations of two AOMs (IntraAction, ATM-80A2) of 80 MHz. The value of δ was varied by at most 5 MHz for the experiment. Since the probe and the newly generated fields are orthogonally polarised to the pump beam, they are filtered using a polariser after the cell. We detect the interference beat between the probe and the newly generated fields with frequency 2δ using a photo-detector (PD). The experimental data is recorded using both an oscilloscope and a spectrum analyzer connected to the PD. The experiment is performed with rubidium vapor, which is heated to a density that is optimized for efficient nonlinear processes. For our case, the cell is heated to a temperature of 120 °C corresponding an approximate number density of 10^{13}cm^{-3} . The vapor cell is magnetically shielded with three layers of cylindrical μ -metal enclosures. We further

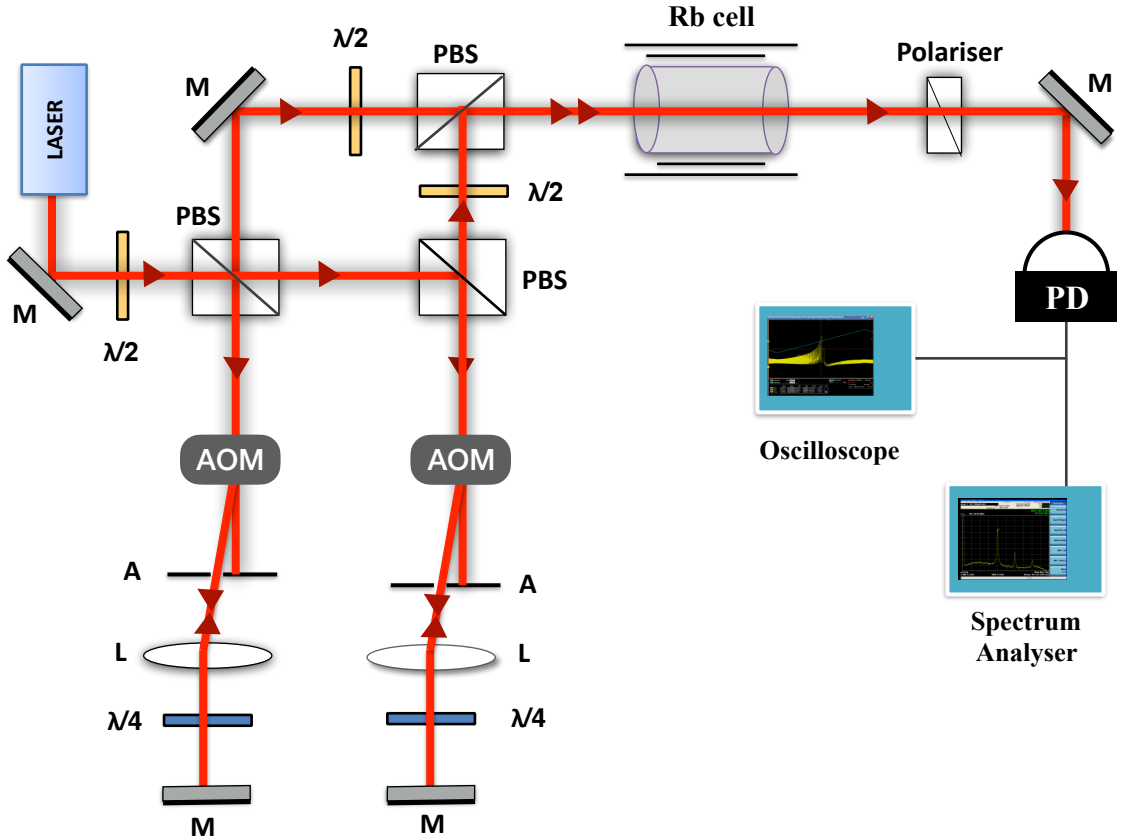


Figure 3.2: Experimental setup for the observation of FWM and XPM. M: Mirror, PBS: Polarising beam splitter, AOM: Acousto-optic modulator, A: Aperture, L: Lens, PD: Photo-detector.

use a solenoid to compensate for a small axial field of the order of 10 mG (Appendix B). To minimize the absorption of the input beams, the laser is blue detuned to the transition, $F = 3$ to $F' = 4$ of D_2 line of ^{85}Rb in the range 500 MHz - 1.5 GHz. The input intensity of the pump and the probe beams used in the experiment are 1.27 W/cm^2 and 0.04 W/cm^2 respectively.

3.1.2 Experimental Results and Discussion

The FWM signal is optimized for the laser detuning such that the probe beam undergoes minimum absorption. The spectroscopy signal showing $^{87}\text{Rb } F = 2 \rightarrow F'$ as well as $^{85}\text{Rb } F = 3 \rightarrow F'$ transition for laser detuning reference is shown in Fig. 3.3(a). We record the 2δ beat signal using an oscilloscope while scanning the laser frequency through both the transitions as shown in Fig. 3.3(b). From the expanded beat signals in both the cases, we observe that the FWM process is more efficient for $^{85}\text{Rb } F = 3 \rightarrow F'$ transition and hence it is chosen for further experimental measurement.

An RF spectrum analyzer is used to measure the FWM beat amplitude. The RF spectra

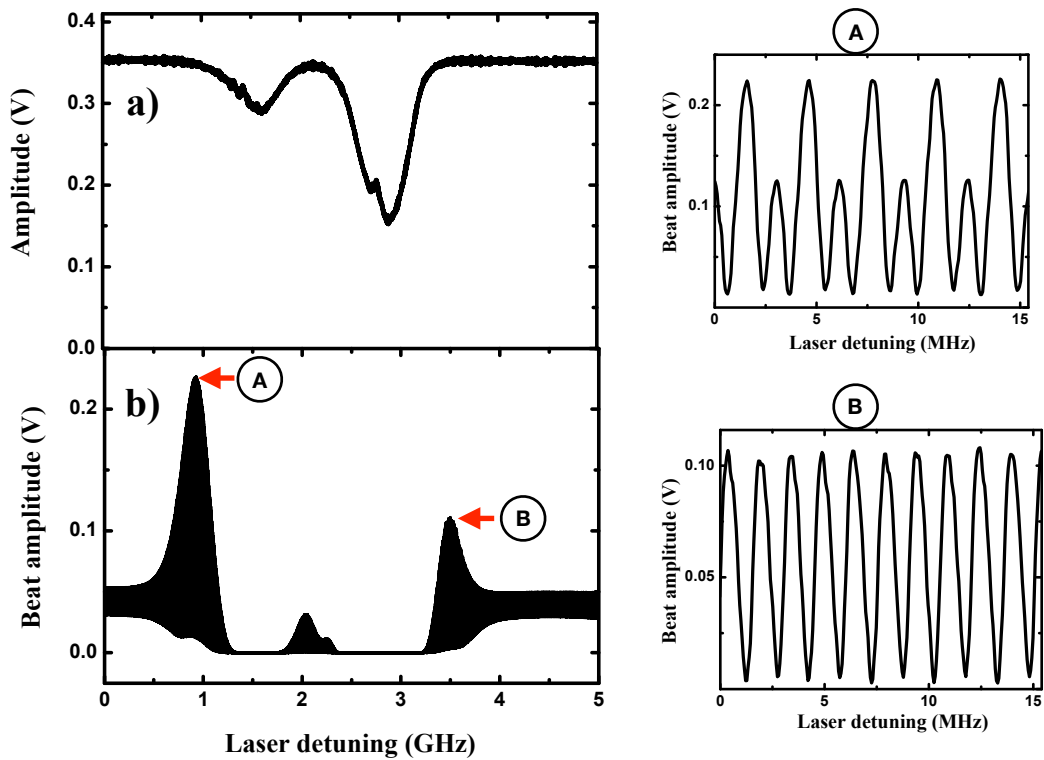


Figure 3.3: a) Rubidium spectroscopy reference b) 2δ beat signal while scanning the laser detuning. Expanded beat signals for A) ^{87}Rb and B) ^{85}Rb .

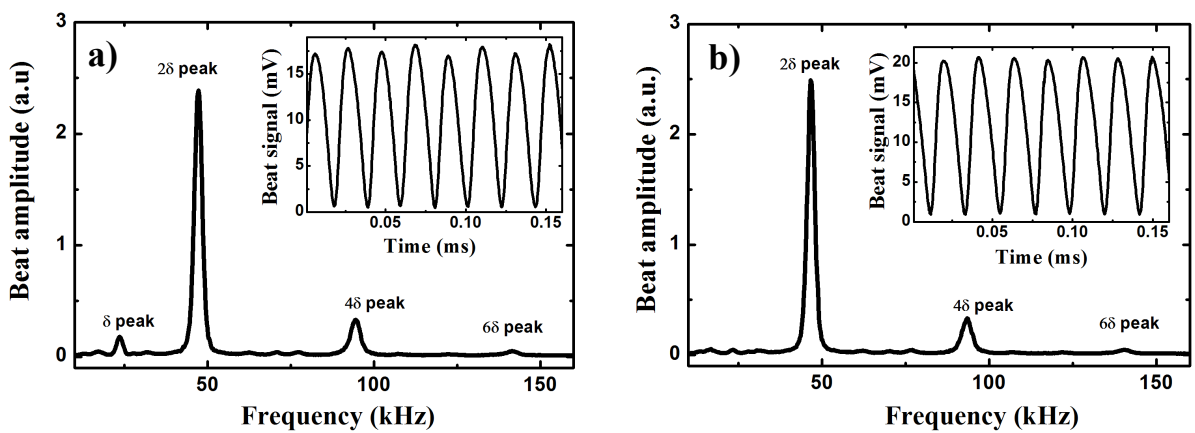


Figure 3.4: Observation of FWM beat signal. spectrum analyzer showing the beat amplitude as a result of the interference between probe and the newly generated fields recorded (a) without magnetic field compensation and (b) with magnetic field compensation. The insets show the corresponding beat signals.

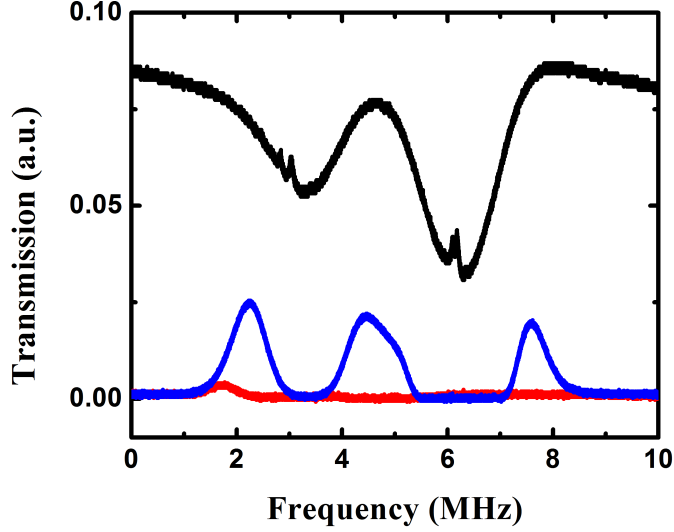


Figure 3.5: Observation of nonlinear magneto-optic rotation. blue line denotes the transmission in the orthogonal direction of the pump beam in presence of a finite magnetic field and red line denotes the transmission after field compensation.

with different experimental conditions are shown in Fig. 3.4(a) and (b) while the insets show the corresponding beat signals observed in the oscilloscope. We observe a larger 2δ -peak as expected along with the 4δ and 6δ -peaks as a result of the higher-order non-linear processes. The presence of a small axial field as allowed by the cylindrical μ -metal enclosure leads to the polarization rotation of the pump field due to the non-linear magneto-optic rotation (NMOR). Hence, a small part of the pump beam (ω), which is rotated to orthogonal direction transmits through the polarizer. It interferes with the probe beam ($\omega + \delta$) resulting in a small δ -peak as shown in Fig. 3.4(a). This NMOR effect and the corresponding small δ -peak can be compensated using a solenoid. To confirm the NMOR effect, the Polarization rotation of the pump field is observed in the absence of the probe field. A typical transmission signal in the orthogonal direction of the linearly polarised pump beam due to NMOR observed for our system is presented in Fig. 3.5. Here the blue line refers to the transmission in presence of a finite magnetic field whereas the red line denotes the transmission after compensating the magnetic field.

The RF spectrum of the beat signal recorded by compensating the magnetic field does not contain the small δ -peak anymore as shown in Fig. 3.4(b). The corresponding beat signals are shown in the insets of Fig. 3.4(a) and (b). The interferometric visibility, which is defined as $\frac{I_{\max} - I_{\min}}{I_{\max} + I_{\min}}$ is calculated for both the cases. The visibility of the interference between the probe and the newly generated light field as shown in Fig. 3.4(b) is found to be nearly one with effective shielding of magnetic field noise. This is because the Zeeman coherence leads to enhanced

FWM, which in turn results in the generation of equal intensities of the probe and the newly generated fields. Therefore, the interferometric visibility is a suitable parameter to measure the efficiency of FWM and XPM in the system.

We study the 2δ -peak height as measured in the spectrum analyzer as a function of the frequency offset δ between the pump and the probe beams. The experimental data are presented in Fig. 3.6(a). We observe that the 2δ -peak height follows an asymmetric peak functional form such that it is maximum for $\delta \approx 0$. This suggests that the FWM process is efficient for the degenerate case i.e. when the pump and probe have the same optical frequencies. We also measure the visibility of the 2δ beat signals by varying δ as shown in Fig. 3.6(b). As expected, the plot shows a decrease in the visibility with an increasing value of δ . The observed asymmetric profile of the peak height is a result of XPM induced in the system.

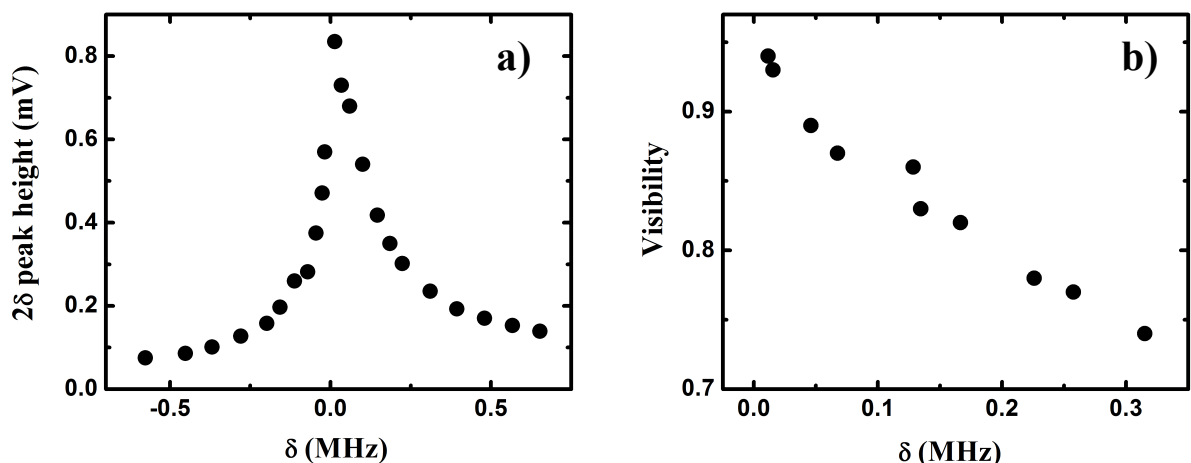


Figure 3.6: a) 2δ -peak height as a function of the frequency offset δ . b) Visibility of the 2δ beat signal as a function of δ .

To study the XPM in the system, we record the probe transmission by varying δ over the two-photon resonance. Under the co-linear phase-matching condition, the 2δ interference pattern due to the FWM process is enveloped by the transmission signal as shown in Fig. 3.7(a). Now, if the pump beam is slightly misaligned from the probe beam, then the new field is generated in a different direction than the probe beam as determined by the phase-matching condition. This leads to the reduction in the beat interference signal as depicted in Fig. 3.7(b). The gain feature in the probe transmission signal is a contribution from the XPM of the probe due to the strong pump beam. Here, we have normalized the transmission signals to the transmission data corresponding to the far off-resonant condition.

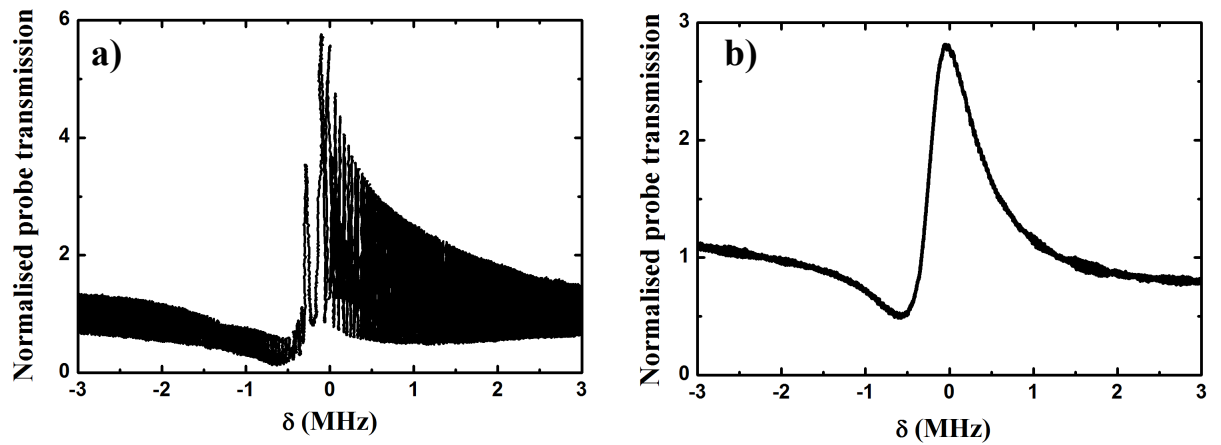


Figure 3.7: Observation XPM in the system. The probe transmission measured (a) with phase-matching and, (b) without phase-matching condition.

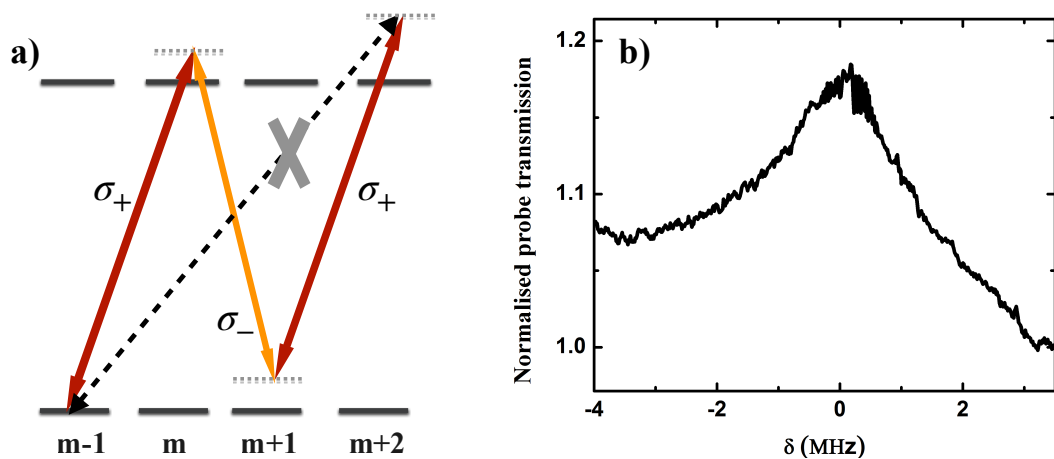


Figure 3.8: a) Scheme of FWM process showing non-conservation of angular momentum and b) Probe transmission showing non-existence of FWM process for the case when pump and probe light fields are of $\sigma^+ - \sigma^-$ Polarizations.

We also investigate the efficiency of the nonlinear processes for different input Polarization states for the pump and probe fields. We observe that the efficiency of the FWM process is highest for linear orthogonal Polarizations for the pump and the probe fields. But when the input fields are of opposite circular Polarizations, the FWM process is prevented as it requires a change of $\Delta m = \pm 3$, which is not allowed by angular momentum conservation as shown in Fig. 3.8(a). The experimentally recorded probe transmission for $\sigma^+ - \sigma^-$ Polarizations for the input beams is presented in Fig. 3.8(a). As expected, it is devoid of 2δ interference due to the FWM process.

3.2 Principle of Polarization rotation of light

In this work, we study the polarization rotation of an input elliptically polarised light assisted by FWM and XPM. The input elliptically polarized light can be expressed as a coherent superposition of two light fields with mutually-orthogonal linear Polarization states. The Polarization states, which form a two-dimensional Hilbert space can be represented on the surface of a sphere with unit radius called the Bloch sphere. Any arbitrary Polarization state can be expressed using two Bloch sphere parameters θ and ϕ as $\cos \frac{\theta}{2} |H\rangle + e^{i\phi} \sin \frac{\theta}{2} |V\rangle$, where $|H\rangle$ and $|V\rangle$ correspond to horizontally and vertically linear polarization states of light respectively. θ is a measure of intensity proportions between the Polarization basis states and ϕ denotes the phase difference between them. As illustrated in the schematic of the Bloch sphere i.e. in Fig 3.9, the north pole and south pole represent the $|H\rangle$ and $|V\rangle$ states respectively. The point with $\theta = \frac{\pi}{2}$ and $\phi = 0(\pi)$ represent the diagonal (anti-diagonal) Polarization state denoted by $|D\rangle(|A\rangle)$. The prime meridian ($\phi = 0, \pi$ and $\theta = 0$ to π) represent all the linear Polarization states. Similarly, point with $\theta = \frac{\pi}{2}$ and $\phi = \frac{\pi}{2}(\frac{3\pi}{2})$ represent the right (left) circular Polarization state denoted by $|R\rangle(|L\rangle)$. All other points on the Bloch sphere represent the elliptical Polarization states of light. In this case, the total intensity is normalized to 1.

Conventionally, the polarisation states are represented using the Poincare sphere and the Stokes parameters, S_0, S_1, S_2 and S_3 satisfying $S_0^2 = S_1^2 + S_2^2 + S_3^2$. Mathematically,

$$S_1 = S_0 \cos 2\psi \cos 2\chi, \quad (3.1)$$

$$S_2 = S_0 \sin 2\psi \cos 2\chi, \quad (3.2)$$

$$S_3 = S_0 \sin 2\chi. \quad (3.3)$$

Here the angles ψ and χ are related to Bloch sphere parameters θ and ϕ as, $2\psi = \theta$ and

$\frac{\pi}{2} - 2\chi = \theta$. It implies that S_1 , S_2 and S_3 are the projections of the polarization vector along $|D\rangle$, $|R\rangle$ and $|H\rangle$ directions respectively on the Bloch sphere whereas S_0 is the total optical power of the light. However, we use the Bloch sphere representation since it allows for simpler theoretical analysis.

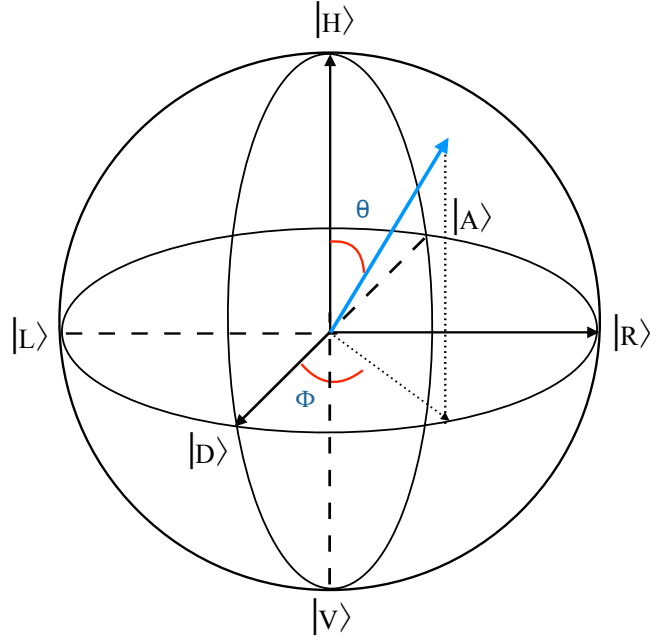


Figure 3.9: Bloch sphere representation of polarization states.

Now if the ellipticity of the input light is small, then one of the two orthogonal components, which is strong, acts as a pump field. The other component being weak is considered as the probe field. Suppose, the pump field is horizontally polarized ($|H\rangle$) with optical frequency ω_h and the probe is vertically polarized ($|V\rangle$) with optical frequency ω_v . FWM process with associated $\chi^{(3)}(\omega_h + \omega_h - \omega_v)$ leads to generation of a light field with same optical frequency if $\omega_h = \omega_v$ with its Polarization to be same as the probe i.e. vertically polarized as ensured by the symmetry of the $\chi^{(3)}$ tensor [21]. In this way, there is intensity transfer from horizontal to vertical Polarization due to FWM and hence the value of θ is changed. Furthermore, the relative phase of the newly generated field is determined by the relative phase between the pump and probe fields and hence, the input phase acts as a control parameter for the interference between the probe and the newly generated field. So, the transmission of the probe through the medium is also modified by its relative phase with the pump beam leading to a change in the value of θ . Similarly, the XPM process with associated $\chi^{(3)}(\omega_h - \omega_h + \omega_v)$ also modifies the transmission

(θ) as well as the output phase (ϕ) of the probe field. Hence, both FWM and XPM contribute to the polarization rotation of the original input beam.

The input, as well as the output polarization directions, can be determined by measuring the intensities along the different Polarization directions. The normalized intensity components along $|H\rangle$, $|V\rangle$, $|D\rangle$, $|A\rangle$, $|R\rangle$ and $|L\rangle$ directions on a Bloch sphere are given by the following expressions:

$$\begin{aligned} I_H &= \frac{1}{2}(1 + \cos \theta), & I_V &= \frac{1}{2}(1 - \cos \theta), \\ I_D &= \frac{1}{2}(1 + \sin \theta \cos \phi), & I_A &= \frac{1}{2}(1 - \sin \theta \cos \phi), \\ I_R &= \frac{1}{2}(1 + \sin \theta \sin \phi), & I_L &= \frac{1}{2}(1 - \sin \theta \sin \phi). \end{aligned}$$

The Bloch sphere parameters θ and ϕ can be calculated from these aforementioned intensities as,

$$\phi = \tan^{-1}\left(\frac{2I_R - 1}{2I_D - 1}\right) \quad (3.4)$$

$$\theta = \cos^{-1}(1 - 2I_V). \quad (3.5)$$

Hence, by measuring the intensities along different polarization directions, we can uniquely determine the polarization states of the input and output light fields.

3.3 Theoretical model: Probe propagation equations

Since we are considering Polarization rotation for an elliptically polarised light traversing the atomic vapor, the effect can be theoretically studied by considering Maxwell's equation with the respective nonlinear Polarization terms.

We start with the general case with different frequencies for the input and generated fields. Let's consider the pump, probe and the newly generated fields propagating through the medium with amplitudes E_p , E_{+s} , E_{-s} and frequencies (propagation constants) $\omega_p(k_p)$, $\omega_{+s}(k_{+s})$ and $\omega_{-s}(k_{-s})$ respectively. The pump field being strong is approximated to be undepleted such that the pump field amplitude remains intact while the weak fields experience the aforementioned nonlinear phenomena present in the system i.e. FWM and XPM with corresponding nonlinear

Polarizations given as,

$$P_{FWM}^{(3)}(\omega_{+s}) = 3\epsilon_0\chi_{FWM}^{(3)}(2\omega_p - \omega_{-s})E_p^2E_{-s}^*, \quad (3.6)$$

$$P_{XPM}^{(3)}(\omega_{+s}) = 3\epsilon_0\chi_{XPM}^{(3)}(\omega_p - \omega_p + \omega_s)|E_p^2|E_{+s}. \quad (3.7)$$

These non-linear source terms are included in the wave equation

$$\nabla^2 E(r) - \frac{\omega^2}{c^2}(1 + \chi^{(1)})E(r) = \frac{\omega^2}{\epsilon_0 c^2}P^{NL}(r). \quad (3.8)$$

Here we use the plane-wave approximation for the fields leading to the fact that the fields depend only on the longitudinal co-ordinate z and hence $\nabla^2 E(r) = \frac{d^2 E(z)}{dz^2}$. Using slowly-varying amplitude approximation i.e. $E_{p,+s,-s}(z) = A_{p,+s,-s}(z)e^{ik_{p,+s,-s}z}$, where the amplitudes $A_{p,+s,-s}(z)$ are slowly varying function of z such that $\left|\frac{d^2 A_{+s,-s}}{dz^2}\right| \ll \left|k_{+s,-s}\frac{dA_{+s,-s}}{dz}\right|$. So, for one of the weak fields, say $E_{+s}(z)$,

$$\frac{d^2 E_{+s}(z)}{dz^2} = \left[2ik_{+s}\frac{dA_{+s}(z)}{dz} - k_{+s}^2 A_{+s}\right] e^{ik_{+s}z}. \quad (3.9)$$

Here the propagation constant k_{+s} is defined as $k_{+s} = n_{+s}\frac{\omega_{+s}}{c}$ where $n_{+s} = n_{s0} + 2n_{+s2}|A_p|^2$, $n_{s0}(= 1 + \frac{1}{2}\text{Re}\chi^{(1)})$ refers to the linear refractive index and n_{+s2} refers to the nonlinear index related to $\chi_{XPM}^{(3)}$ as $n_{+s2} = \frac{3}{4n_{s0}}\text{Re}\chi_{XPM}^{(3)}$. Therefore,

$$k_{+s}^2 = (n_{s0} + 2n_{+s2}|A_p|^2)^2 \frac{\omega_{+s}^2}{c^2}, \quad (3.10)$$

$$= (n_{s0}^2 + 4n_{s0}n_{+s2}|A_p|^2) \frac{\omega_{+s}^2}{c^2}. \quad (3.11)$$

Here we have ignored the higher-order term $4n_{+s2}^2|A_p|^4$. Thus the wave-equation for A_{+s} can be written as,

$$\begin{aligned} & 2ik_{+s}\frac{dA_{+s}}{dz} - (n_{s0}^2 + 4n_{s0}n_{+s2}|A_p|^2)\frac{\omega_{+s}^2}{c^2}A_{+s} + n_{s0}^2\frac{\omega_{+s}^2}{c^2}A_{+s} + i\frac{\omega_{+s}^2}{c^2}\text{Im}\chi^{(1)}A_{+s} \\ & = -3\frac{\omega_{+s}^2}{c^2}\left[\chi_{FWM}^{(3)}A_p^2A_s^*e^{-i(2k_p-k_{+s}-k_{-s})z} + (\text{Re}\chi_{XPM}^{(3)} + i\text{Im}\chi_{XPM}^{(3)})|A_p|^2A_s\right], \\ \implies & 2ik_{+s}\frac{dA_{+s}}{dz} - 4n_{s0}n_{+s2}\frac{\omega_{+s}^2}{c^2}|A_p|^2A_{+s} + i\frac{\omega_{+s}^2}{c^2}\text{Im}\chi^{(1)}A_{+s} \\ & = -3\frac{\omega_{+s}^2}{c^2}\left[\chi_{FWM}^{(3)}A_p^2A_s^*e^{-i(2k_p-k_{+s}-k_{-s})z} + \left(\frac{4n_{s0}n_{+s2}}{3} + i\text{Im}\chi_{XPM}^{(3)}\right)|A_p|^2A_s\right], \\ \implies & 2ik_{+s}\frac{dA_{+s}}{dz} + i\frac{\omega_{+s}^2}{c^2}(\text{Im}\chi^{(1)} + \text{Im}\chi_{XPM}^{(3)})|A_p|^2A_{+s} = -3\frac{\omega_{+s}^2}{c^2}\chi_{FWM}^{(3)}A_p^2A_s^*e^{-i(2k_p-k_{+s}-k_{-s})z}. \end{aligned}$$

We proceed the same way for A_{-s} and divide the equations by $2ik_{+s}$ and $2ik_{-s}$ respectively to get

$$\frac{dA_{+s}}{dz} = -\alpha_{+s}A_{+s} + i\kappa_s A_{-s}^* e^{-i(2\Delta kz)}, \quad (3.12)$$

$$\frac{dA_{-s}}{dz} = -\alpha_{-s}A_{-s} + i\kappa_{-s} A_{+s}^* e^{-i(2\Delta kz)}. \quad (3.13)$$

where

$$\alpha_{\pm s} = \frac{1}{2} \frac{\omega_{\pm s}}{n_{\pm s} c} \text{Im} \chi_{eff}^{(1)}(\omega_p \pm \delta), \quad (3.14)$$

$$\kappa_{\pm s} = i \frac{3}{2} \frac{(\omega_p \pm \delta)}{n_{\pm s} c} \chi_{FWM}^{(3)} A_p^2, \quad (3.15)$$

$$2\Delta k = (2k_p - k_{+s} - k_{-s}), \quad (3.16)$$

$$= \Delta n \frac{\omega_p}{c} = \frac{1}{2} \frac{\omega_p}{n_{\pm s} c} \text{Re} \chi_{XPM}^{(3)} |A_p|^2. \quad (3.17)$$

Where, $\chi_{eff}^{(1)} = \chi_{2L} + \chi_{XPM}^{(3)} |A_p|^2$. Here A_p is the complex envelope of the pump field amplitude, $n_{+s}(n_{-s})$, n_p are the refractive indices of the probe (newly generated) and pump field respectively and $\Delta n (= n_p - n_{\pm s})$ is the difference in refractive indices of the fields. χ_{2L} is the susceptibility pertaining to two-level system and does not contain the effect of Zeeman coherence. It can be mathematically expressed as, $\chi_{2L} = \chi^{(1)} + \chi_{SPM}^{(3)} |A_p \hat{x} + e^{i\phi} A_s \hat{y}|^2$. Here $\chi^{(1)}$ is the linear susceptibility and $\chi_{SPM}^{(3)}$ is the self-phase modulation (SPM) of the total input light field $|A_p \hat{x} + e^{i\phi} A_s \hat{y}|$, which is independent of light Polarization. Hence, $\chi_{SPM}^{(3)}$ being same for both the probe and the pump fields, doesn't contribute to the Polarization rotation of the total light field.

For the case of Polarization rotation, $\omega_p = \omega_{\pm s}$ the system undergoes degenerate FWM. Hence, the newly generated field can not be distinguished from the probe field. Therefore, we substitute $A_s = A_{+s} = A_{-s}$, so that the equations (1) and (2) boil down to a single equation given as,

$$\frac{dA_s}{dz} = -\alpha_s A_s + i\kappa_s A_s^* e^{-i(2\Delta kz)}. \quad (3.18)$$

The amplitude of the probe field (A_s), measured after a medium of length z is given by,

$$A_s(z) = e^{(i2\Delta k - \alpha_s)z} [f(p)(iz)(\kappa_s A_s^*(0) - \Delta kz) + g(p)A_s(0)], \quad (3.19)$$

with,

$$f(p) = \frac{e^{2pz} - e^{-2pz}}{2pz}, \quad g(p) = \frac{e^{2pz} + e^{-2pz}}{2}.$$

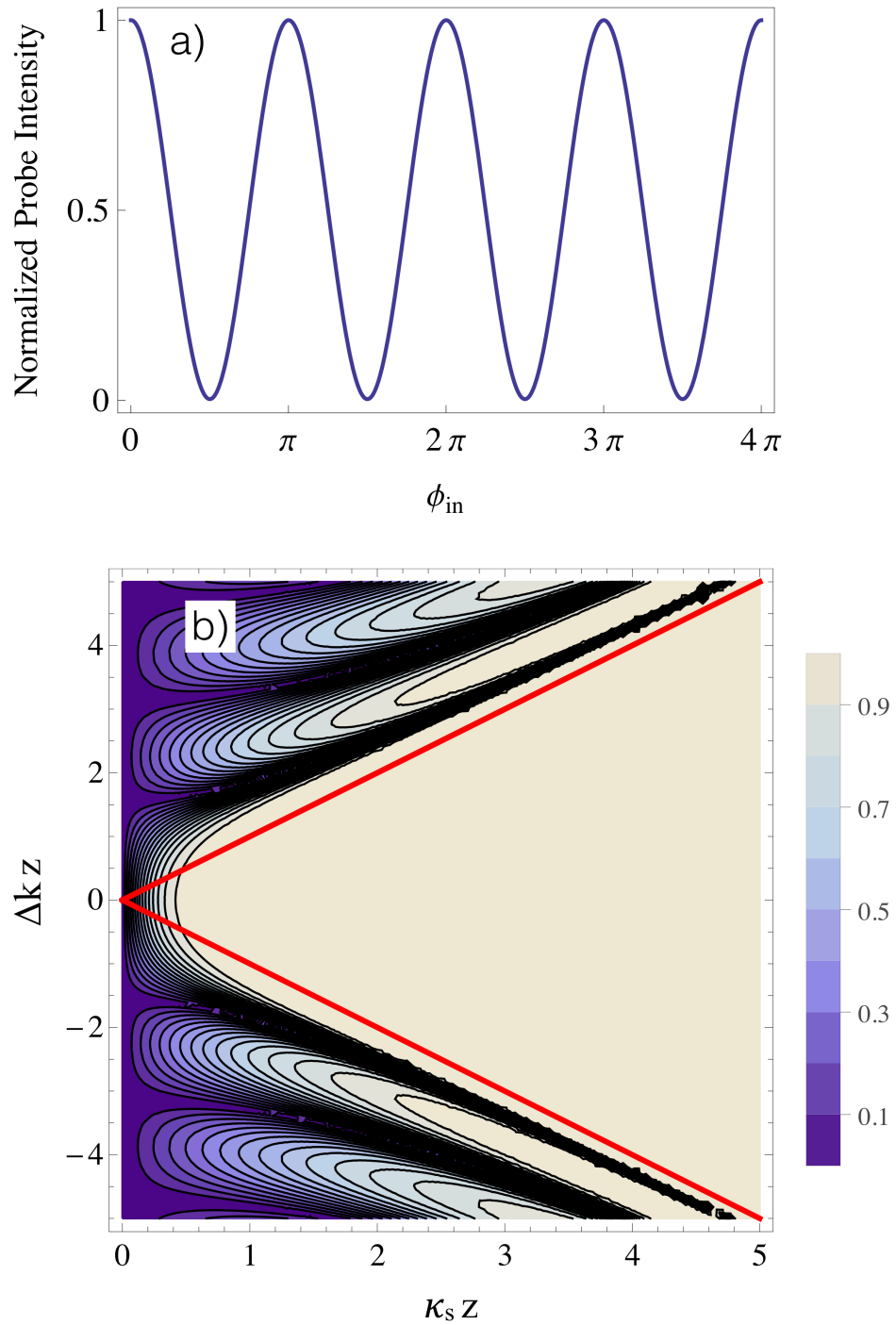


Figure 3.10: (a) Normalized output probe intensity as a variation of the relative phase of the pump and the probe fields. (b) Contour plot of visibility in the parameter space of Δkz and $\kappa_s Z$. The red solid lines refers to the visibility for $\Delta k = -\kappa_s$ and $\Delta k = \kappa_s$.

Here, $p = \sqrt{\kappa_s^2 - (\Delta k)^2}$ and $A_s(0)$ is the amplitude of the probe field at the input face of the medium. A_p is chosen to be real and $A_s = |A_s|e^{i\phi_{in}}$ such that ϕ_{in} is the relative phase between the pump and the probe light field amplitudes before the medium. Equation (3.4) can be used to understand the Polarization rotation under different parameter range. Then the output intensity $I_s(z)$, which is normalized to $I_s(0)e^{-2\alpha_s z}$ with $I_s(0)$ being the input intensity, can be calculated and is given by the expression as

$$I = f(p)^2(\kappa_s^2 + \Delta k^2 - 2\kappa_s \Delta k \cos 2\phi_{in})z^2 + g(p)^2 + 2\kappa_s z f(p)g(p) \sin 2\phi_{in}.$$

We present a typical form of the output intensity with ϕ_{in} in Fig. 3.10(a), where the values of $\kappa_s z$ and $\Delta k z$ used are 2.85 and 3 respectively. Here, the presented interference pattern has a period of π as a function of ϕ_{in} , because the phase difference between the probe and the newly generated field is $2\phi_{in}$. Now a visibility function defined as, $V = \frac{I_{max} - I_{min}}{I_{max} + I_{min}}$ can be used to study the combined effect of FWM and XPM processes inside the medium. For better understanding, we present a contour plot of visibility as a function of $\kappa_s z$ and $\Delta k z$ as depicted in Fig. 3.10(b).

We consider the two cases, $\Delta k < \kappa_s$ i.e. p is real and $\Delta k > \kappa_s$ i.e. p is imaginary. As shown in Fig. 3.10(b), the triangular region within the lines for $p = 0$, corresponds to visibility for real value of p . In this region, $f(p)$ and $g(p)$ are hyperbolic functions of p and the probe intensity is calculated to be, $I = \frac{\sinh^2 2pz}{p^2}(\kappa_s^2 + \Delta k^2 - 2\kappa_s \Delta k \cos 2\phi_{in}) + \cosh^2 2pz + 2\frac{\kappa_s}{p} \sinh 4pz \sin 2\phi_{in}$. In this region, as the FWM process dominates over the phase mismatch due to XPM, the larger visibility is obtained with smaller FWM co-efficient. This effect can be understood by considering a simple case, $\Delta k = 0$ i.e. when there is no phase mismatch in the system. Then the probe intensity reads as, $I = 1 + \sinh(4\kappa_s z) \sin(2\phi_{in})$, so that $V = \tanh 4\kappa_s z$ which saturates to a value close to 1 for a finite smaller value of $\kappa_s z$.

Now, when p is imaginary, $f(p)$ and $g(p)$ are trigonometric functions of pz . The visibility function, in this case, is shown by the uppermost and lowermost triangular region of Fig. 3.10(b). For the simplest case of $\kappa_s = 0$ i.e., when FWM is absent in the system, the probe intensity becomes constant with ϕ_{in} with no visibility. This is represented by the y-axis of Fig. 3.10(b). For this case of imaginary p , the combined effect of FWM and XPM results in an oscillatory pattern of visibility. To understand further, we plot the visibility as a variation of the propagation direction z with different ratios of $\frac{\Delta k}{\kappa_s}$ as presented in Fig. 3.11. If Δk is very large, which is a result of a large change in the refractive index due to XPM as well as a finite relative angle between pump and probe, then the amplitude of the generated field is small

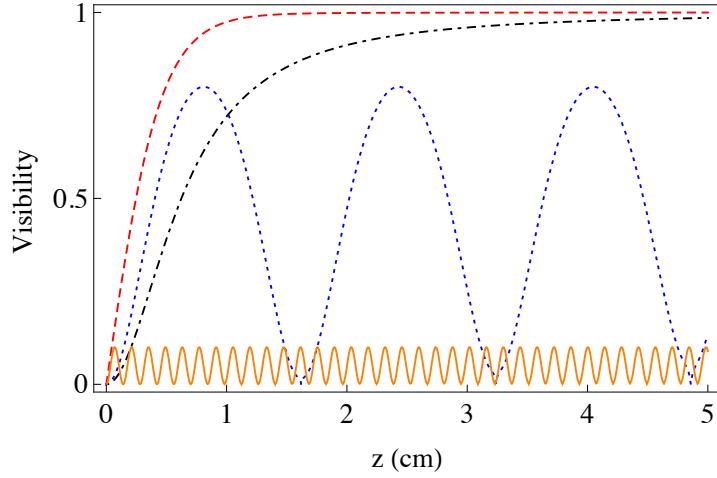


Figure 3.11: Variation of visibility with z for $\Delta k = 0$ (red dashed line), $\Delta k = \kappa_s$ (black dash-dotted line), $\Delta k = 2\kappa_s$ (blue dotted line) and $\Delta k = 20\kappa_s$ (orange solid line). The value of κ_s used is 57 m^{-1} .

compared to the probe amplitude. Hence, the maximum visibility of interference of probe and newly generated field is much smaller than 1. For an intermediate value of Δk , the visibility is a periodic function of z .

The visibility plot provides an intuitive understanding of interesting effects due to FWM and XPM in the system such as the generation of a squeezed vacuum state. Let's consider the case for which, the probe is the vacuum state in the system. Then the field component of the vacuum fluctuation, which is in phase with the pump field will increase as a result of its constructive interference with the newly generated field due to degenerate FWM. On the other hand, the destructive interference will suppress the field component in quadrature and it will lead to a squeezed vacuum state. The amount of squeezing, in this case, depends on the interference visibility with maximum squeezing corresponding to the visibility value of 1. Hence, we can obtain the parameter range for the efficient generation of squeezed vacuum state of light from the visibility plot. One such parameter range is $\Delta k \leq \kappa_s$ with a finite value of $\kappa_s z$ such that the visibility is nearly 1 as discussed previously. But for $\Delta k > \kappa_s$, the visibility has an oscillatory pattern resulting in more constraints on the range of parameters. For example, let's consider two cases: $\kappa_s z = 2.5, \Delta k z = 3.3$ with maximum visibility and $\kappa_s z = 3.5, \Delta k z = 4.6$ with minimum visibility (Ref. to Fig. 3). So, a larger $\kappa_s z$ does not ensure maximum squeezing rather it requires an experimentally achievable combination of both the parameters. This effect can be understood better by studying the rotation of the

polarization state of a light field traversing the medium. The following section provides the details of the method and experimental arrangement for the observation of polarization rotation in the system.

3.4 Experimental setup

The schematic of the experimental arrangement is shown in Fig.3.12. Here a laser beam from an external cavity diode laser is split using a polarizing beam splitter (PBS) into two orthogonal linearly-polarized laser beams. One of the two i.e. the transmitted beam is kept at high intensity and it is considered as the pump beam. The other beam of relatively lower intensity acts as the probe beam. The probe beam is passed through a corner cube retro-reflector (CCR) and then is superimposed with the pump beam using a non-polarizing beam splitter (NPBS). A piezo-actuator is attached to the CCR as shown in Fig 3.13(a). When a suitable piezo voltage is applied, the actuator undergoes expansion or contraction and hence changes the optical path length of the probe beam with respect to that of the pump beam. In this way, a relative path difference leading to a relative phase shift is introduced between the pump and probe beams. The linear dependence between the piezo voltage and phase shift implies that when the piezo is applied with a ramp voltage, the phase shift varies alternatively from 0 to 2π . This leads to an interference of the beams with time. A typical signal is presented in Fig 3.13(b), where we have allowed equal powers in both the beams through a polariser. The experimental data shows a good fitting with a sinusoidal function. This proves the linear behavior of the piezo expansion with applied voltage. In this case, when the PZT voltage is fixed, the stability of the relative phase between the paths is dependent on the noise due to vibrations and acoustic disturbances. This is minimized by floating the optical table. Furthermore, with the measurement time of 10 ms (refer to Fig. 3.13), these low-frequency noises have a negligible effect on the experiment.

Two Glan-Thompson polarizers (GTH10-B) are used in the paths of both the pump and the probe beams to make them highly polarized with an extinction ratio of $\sim 5000:1$. We use two half-wave plates before the polarizers to vary the intensities of both the beams. The pump and the probe beams are made horizontally and vertically polarized respectively. Now, as the intensities of both the beams are fixed and the relative phase is varied using piezo, it leads to the generation of a set of elliptical polarization of light. The elliptically polarized beam generated at one of the output ports of the NPBS is used for the experiment by passing it through thermal

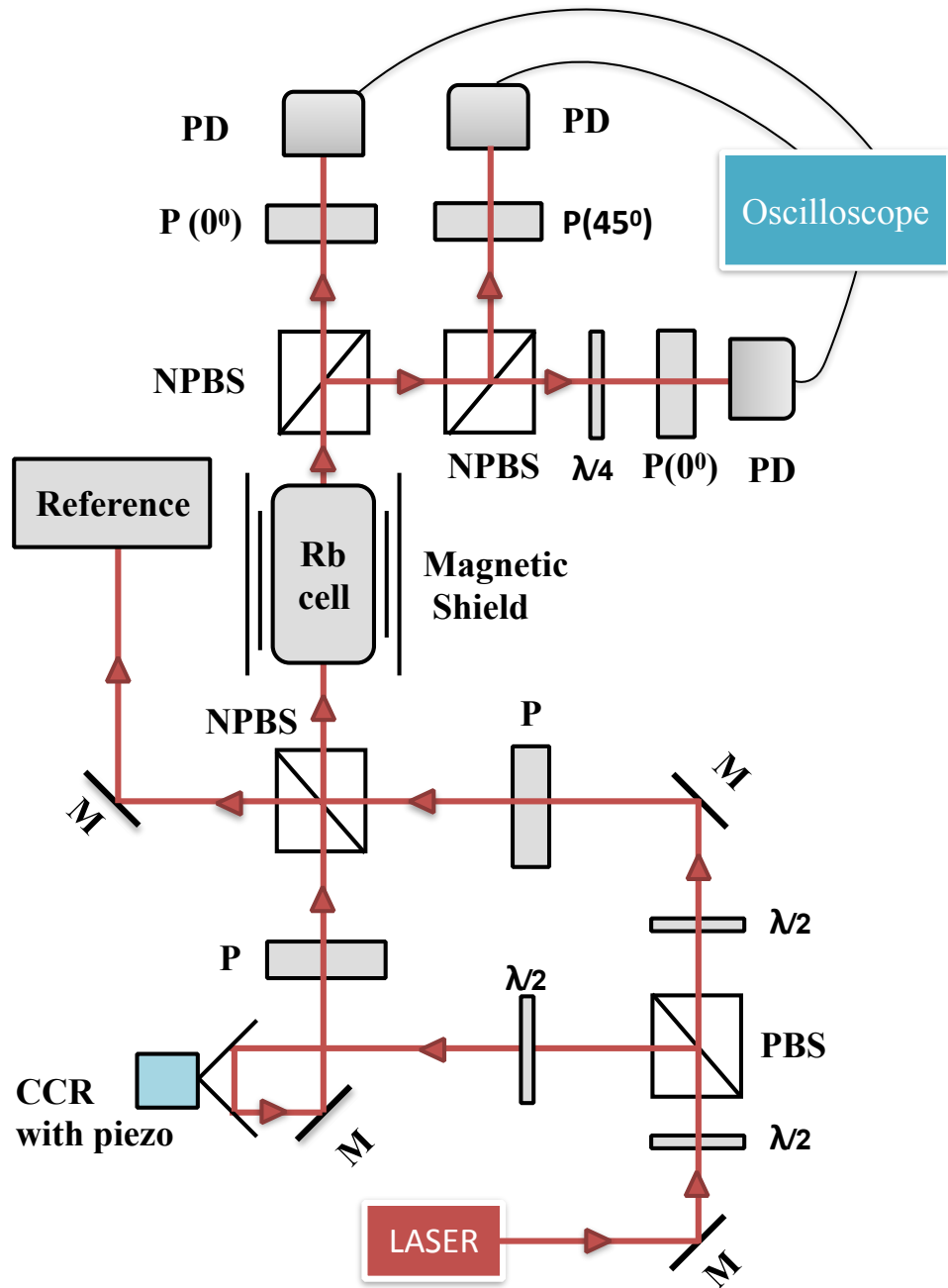


Figure 3.12: Schematic of the experimental arrangement to measure the Polarization rotation. M: Mirror, PBS: Polarizing beam splitter, NPBS: Non-Polarizing beam splitter, CCR: Corner cube retro-reflector, P(θ): Polarizer aligned at θ w.r.t $|V\rangle$, P: Glan-Thompson polariser, PD: Photo-detector.

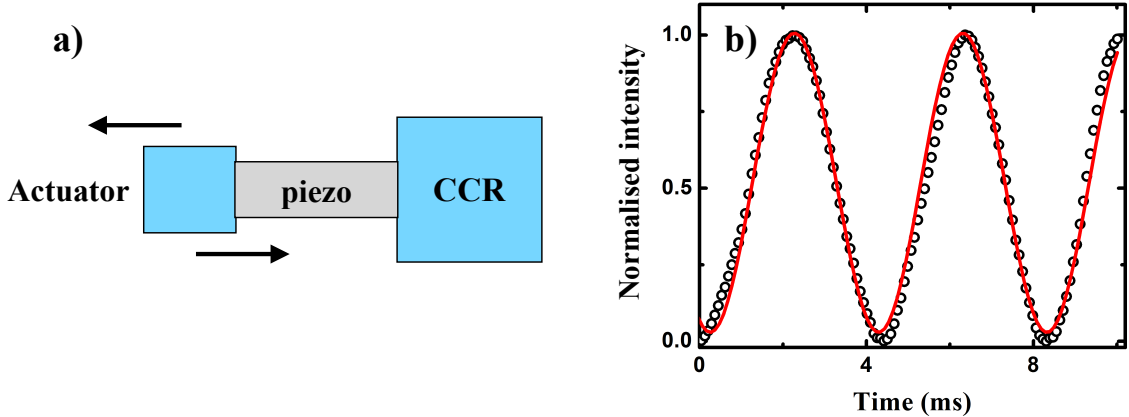


Figure 3.13: a) Schematic of piezo actuator attached to Corner cube retro-reflector (CCR). b) A typical interference signal between the pump and probe when the phase difference between them is varied using the piezo. The black circles represent the experimental data whereas the red line shows its fitting with a sinusoidal function.

rubidium vapor in the regime of efficient FWM. The light from the other output port of the NPBS is used for reference.

We divide the output beam into three parts using two non-polarizing beam splitters. A polarizer at 0° to the vertical polarization is used in one of the paths to measure the probe intensity along the vertical polarization direction (I_V). A polarizer at 45° is used in another path to measure the intensity along 45° polarization (I_D). A quarter-wave plate at 45° followed by a polarizer at 0° is used in the remaining output path to measure the intensity along the right circularly polarization direction (I_R). We apply the same measurement technique in the reference path to determine the correspondence between the input and the output polarization states. As discussed before, a solenoid is used to reduce the residual magnetic field noise along the axial direction. The temperature of the vapor cell is kept between 110° - 120° C for the experiment with the corresponding number density of $\sim 10^{13}\text{cm}^{-3}$. The experiment is performed with ^{85}Rb and the laser is blue detuned by about 500 MHz to the transition, $F = 3$ to $F' = 4$ of the D2 line. We use the pump and the probe intensities to be 1.02 and 0.002 W/cm^2 respectively.

3.4.1 Experimental Results

The polarization of the input and output beams are determined by measuring the intensities along different polarisation directions as explained before. The corresponding Bloch sphere parameters (refer to equations 3.4 and 3.5) for the input as well as the output polarisation states

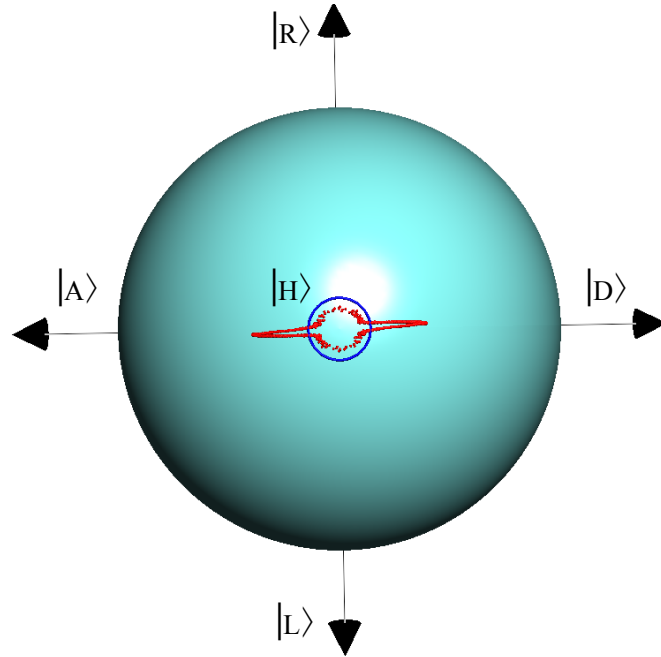


Figure 3.14: Bloch sphere representation showing the polarization rotation of light field. The solid line (blue) represents the input polarization states and points (red) denote the output polarization states.

are evaluated and are represented on the Bloch sphere as shown in Fig. 3.14. Since we vary the relative phase between the horizontal and vertical polarisation directions while keeping the relative intensity fixed, the input polarization states with a fixed value of θ and ϕ varying between 0 to 2π trace a circle around $|H\rangle$. The blue solid line in Fig. 3.14 denotes the input Polarization states. The red points represent the output polarization states after the rotation. It is observed that if the relative phase between the pump and the probe beams is close to 0^0 or 180^0 , there is a constructive interference between the probe and the newly generated field leading to the enhancement of I_V . However, when the relative phase is close to 90^0 or 270^0 , there is destructive interference of probe and newly generated fields resulting in the suppression of I_V . Hence, a squeezed vacuum state can be generated in the orthogonal polarization direction of an input linearly polarised light field traversing the same medium as explicitly discussed in the theoretical section similar to systems exhibiting self-polarisation rotation [6–8].

To analyze the correspondence between the input and output polarization states, we plot the output Bloch sphere parameters ϕ_{out} and θ_{out} as a function of the input Bloch sphere parameter ϕ_{in} as presented in Fig. 3.15 (a) and (b). We use the theoretical analysis of the probe prop-

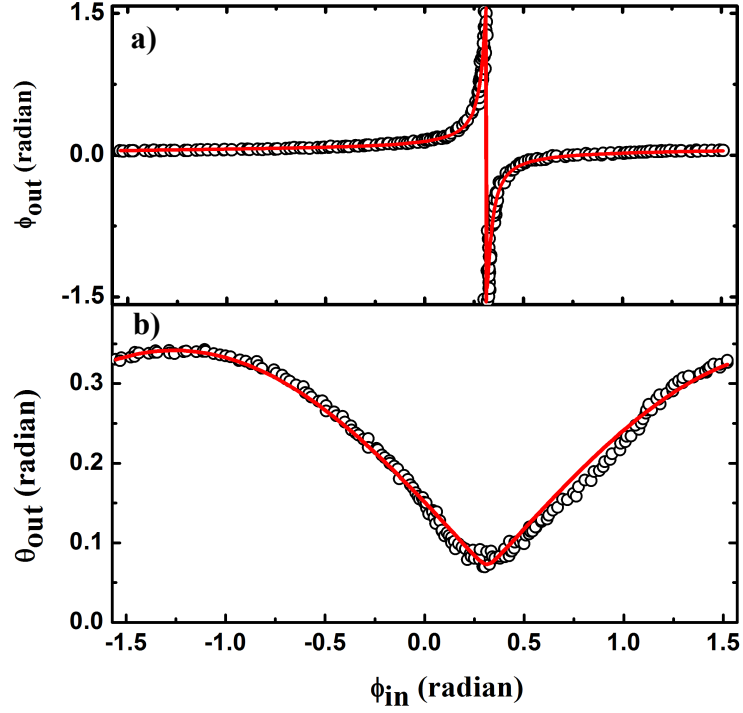


Figure 3.15: Output Bloch sphere parameters (a) ϕ_{out} and (b) θ_{out} as a function of ϕ_{in} . The open circles are the experimental data and the red solid curves are the theoretical fitting.

agation equation to fit the experimental data. Here the Bloch sphere parameters θ and ϕ are evaluated from the expression of the complex probe amplitude A_s . Since we have considered pump field amplitude to be real, the complex phase of A_s is the Bloch sphere parameter ϕ . The other parameter θ is a measure of the intensity proportion of the pump and the probe fields and hence it is evaluated by using $I_s = I_p \cos^2 \frac{\theta}{2}$. So theoretically the Bloch sphere parameters are evaluated using,

$$\phi = \tan^{-1} \left[\frac{Im(A_s)}{Re(A_s)} \right] \quad \theta = 2 \cos^{-1} \frac{|A_s|}{|A_p|}, \quad (3.20)$$

where $|A_s|$ is given by the equation 3.19. The experimental data is found to fit well with the theoretical analysis. From the theoretical fitting, we obtain the value of $\kappa_s z$ and $\Delta k z$ which can give an estimate of the non-linearities induced in the system as explained in the following section.

3.4.2 Estimation of nonlinear susceptibilities of the medium

We define effective nonlinear susceptibilities for both FWM and XPM by considering those higher order nonlinear optical processes, which results in the newly generated light field of

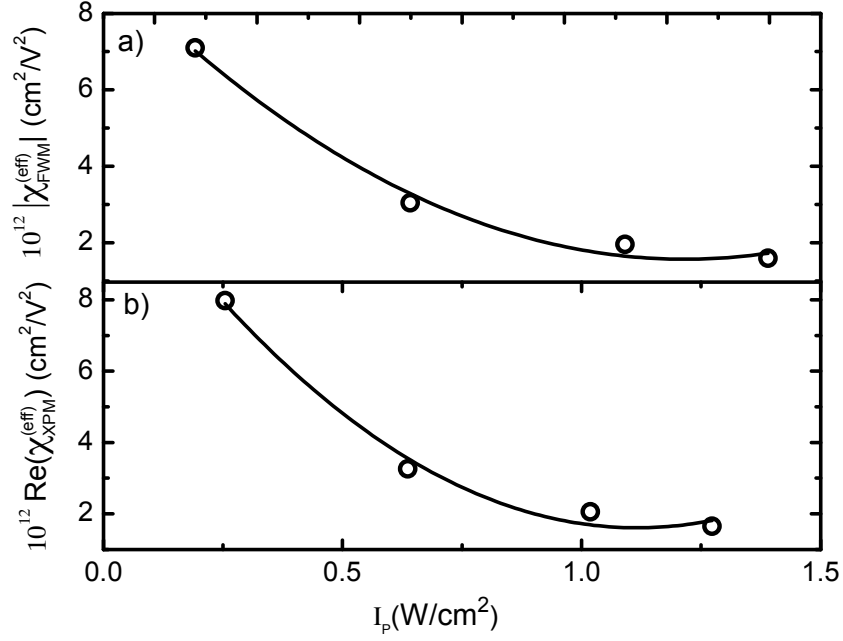


Figure 3.16: Variation of (a) $|\chi_{FWM}^{eff}|$ and (b) $\text{Re}(\chi_{XPM}^{eff})$ as a function of pump intensity, I_p . The open circles denote the experimental data and the solid lines represent the fittings to quadratic functions.

same phase as that due to degenerate FWM. These effective susceptibilities can be mathematically expressed as,

$$\chi_{FWM}^{(eff)} = \chi_{FWM}^{(3)} + \frac{10}{3\epsilon_0 C} \chi_{FWM}^{(5)} I_p + \frac{28}{3\epsilon_0^2 C^2} \chi_{FWM}^{(7)} |I_p|^2 + \dots$$

$$\chi_{XPM}^{(eff)} = \chi_{XPM}^{(3)} + \frac{10}{3\epsilon_0 C} \chi_{XPM}^{(5)} I_p + \frac{28}{3\epsilon_0^2 C^2} \chi_{XPM}^{(7)} |I_p|^2 + \dots$$

Here I_p is the input pump intensity. $\chi_{FWM}^{(5)}$ is the fifth-order nonlinear susceptibility, which involves the absorption of three pump photons as well as the stimulated emission of one pump and two probe photons. $\chi_{FWM}^{(7)}$ is the seventh order nonlinear susceptibility, which involves the absorption of four pump photons as well as the stimulated emission of two probe and two pump photons. The resulting newly generated light field due to these higher-order processes can't be distinguished from the one due to the third-order process of FWM. Similarly, $\chi_{XPM}^{(5)}$ refers to a process with both absorption and emission of two pump photons and one probe photon. $\chi_{FWM}^{(7)}$ involves both absorption and emission of three pump photons and one probe photon. The contributions from these processes depend strongly on the input intensity of the pump beam.

To have an estimation of these higher order optical non-linearity induced in the system, the experimental data of Polarization rotation are recorded with probe intensity fixed at 0.002 W/cm^2 and the pump intensity being varied from 0.254 to 1.27 W/cm^2 . The Bloch sphere parameters are calculated experimentally and fitted with the theory. From the theoretical fitting, χ_{FWM}^{eff} and χ_{XPM}^{eff} are evaluated and are plotted as a function of the input pump intensity, I_p as depicted in Fig. 3.16 (a) and (b). The data are fitted with a polynomial function of the form, $a + bI_p + cI_p^2$, where a, b, c are related to $\chi^{(3)}, \chi^{(5)}$ and $\chi^{(7)}$ for the corresponding nonlinear process respectively. From the fitting of $|\chi_{FWM}^{eff}|$, the value of $\chi_{FWM}^{(3)}$ was found to be $1.07 \pm 0.09 \times 10^{-11} \text{ cm}^2/\text{V}^2$ with value of $\chi_{FWM}^{(5)}$ and $\chi_{FWM}^{(7)}$ given by, $-1.28 \pm 0.16 \times 10^{-14} \text{ cm}^4/\text{V}^4$ and $4.16 \pm 0.95 \times 10^{-22} \text{ cm}^6/\text{V}^6$ respectively. Similarly from the fitting of $\text{Re}\chi_{XPM}^{eff}$, the values of $\text{Re}\chi_{XPM}^{(3)}, \text{Re}\chi_{XPM}^{(5)}$ and $\text{Re}\chi_{XPM}^{(7)}$ are found to be $1.21 \pm 0.11 \times 10^{-11} \text{ cm}^2/\text{V}^2$, $-1.5 \pm 0.24 \times 10^{-14} \text{ cm}^4/\text{V}^4$ and $4.88 \pm 1.14 \times 10^{-22} \text{ cm}^6/\text{V}^6$ respectively. The value of nonlinear susceptibility due to XPM ($\text{Re}\chi_{XPM}^{(3)}$) presented for our system is four orders of magnitude higher than that reported for atomic media with electromagnetically induced transparency [24].

3.5 Conclusion

This work involves the study polarization rotation of an elliptically polarized light assisted by the efficient FWM and XPM processes in the medium with Zeeman coherence. The experimental data are explained using a basic theoretical analysis of the light propagation through a nonlinear medium and the theoretical fitting of the data provides an estimate of the nonlinear susceptibilities associated with FWM and XPM induced in the system. This study promises application towards providing useful parameters for generating a squeezed vacuum state of light.

Bibliography

- [1] I. Novikova, A. B. Matsko, V. A. Sautenkov, V. L. Velichansky, G. R. Welch, and M. O. Scully, *Opt. Lett.* **25**, 1651 (2000).
- [2] William V Davis, Alexander L. Gaeta, and Robert W Boyd *Opt. Lett.* **17**, 1304 (1992).
- [3] S. M. Rochester, D. S. Hsiung, D. Budker, R. Y. Chiao, D. F. Kimball and V. V. Yashchuk, *Phys. Rev. A* **63**, 043814 (2001).
- [4] Travis Horrom, Salim Balik, Arturo Lezama, Mark D. Havey and Eugeny E. Mikhailov, *Phys. Rev. A* **83**, 053850 (2011).
- [5] J. Ries, B. Brezger and A. I. Lvovsky, *Phys. Rev. A* **68**, 025801 (2003).
- [6] I. Novikova, A. B. Matsko, and G. R. Welch *J. Mod. Opt.* **49**, 2565 (2002).
- [7] A. B. Matsko, I. Novikova, G. R. Welch, D. Budker, D. F. Kimball, and S. M. Rochester *Phys. Rev. A* **66**, 043815 (2002).
- [8] Min Jeong Seo, Heung-Ryoul Noh *Opt. Commun.* **285**, 5175 (2012).
- [9] Eugeny E. Mikhailov and Irina Novikova *Opt. Lett.* **33**, 11 (2008).
- [10] M. Faraday, *Experimental Research in Electricity*, (London, 1855), Vol. III.
- [11] A. Cotton, and H. Mouton, *J. Phys.* **1**, 5 (1911).
- [12] W. Gawlik *et al.*, *Phys. Lett. A* **48**, 283 (1974); A. Weiss, V.A. Sautenkov, and T.W. Hansch, *Phys. Rev. A* **45**, 7991 (1992).
- [13] K.H. Drake, W. Lange, and J. Mlynek 1998 *Opt. Commun.* **66**, 315.
- [14] Budker D *et al.*, *Rev. Mod. Phys.* **74** 1153 (2002).

- [15] S. I. Kanorsky, A. Weis, J. Wurster, and T. W. Hansch *Phys. Rev. A* **47**, 1220 (1993).
- [16] D. Budker and M. V. Romalis *Nat. Phys.* **3**, 227 (2007).
- [17] S. Pustelny, A. Wojciechowski, M. Gring, M. Kotyrba, J. Zachorowski, and W. Gawlik, *J. Appl. Phys.* **103**, 063108 (2008).
- [18] S. Knappe, P. Schwindt, V. Shah, L. Hollberg, J. Kitching, L. Liew, and J. Moreland, *Opt. Express* **13**, 1249 (2005).
- [19] A. Cere, V. Parigi, M. Abad, F. Wolfgramm, A. Predojevic, and M. W. Mitchell, *Opt. Lett.* **34**, 1012 (2009).
- [20] D. J. Dick and T. M. Shay, *Opt. Lett.* **16**, 867 (1991).
- [21] R. W. Boyd, *Nonlinear Optics*, 3rd ed. (Academic, New York, 2008).
- [22] A. Lezama, S. Barreiro, A. Lipsich, and A. M. Akulshin, *Phys. Rev. A* **61**, 013801 (1999).
- [23] A.M. Akulshin, R.J. McLean, A.I. Sidorov and P. Hannaford, *J. Phys. B: At. Mol. Opt. Phys.* **44**, 175502 (2011).
- [24] Yanpeng Zhang, Zhiguo Wang, Zhiqiang Nie, Changbiao Li, Haixia Chen, Keqing Lu, and Min Xiao, *Phys. Rev. Lett.* **106**, 093904 (2011).

Chapter 4

Mirrorless optical parametric oscillator inside an all-optical waveguide

The phenomenon of mirrorless optical parametric oscillator (MOPO) was first theoretically predicted by S.E. Harris [1] and has been extensively studied ever since. It has been demonstrated in non-linear $\chi^{(2)}$ medium assisted by parametric down conversion [2–5] and in non-linear $\chi^{(3)}$ medium assisted by FWM process [6–11]. The FWM-based MOPO leads to the generation of a pair of fields from noise due to nonlinear interaction of a pair of input counter-propagating strong fields. The effect has been investigated in cold atomic ensemble as well as in thermal atomic vapor [16–21]. The input strong fields induce spatially varying refractive index for the generated beams via XPM and hence lead to the all-optical wave guiding effect [23–31]. Using Gaussian [32] as well as doughnut-shaped pump beams [33, 34], all-optical waveguiding has been demonstrated in thermal Rubidium vapor.

While all the existing works in the last few decades on MOPO are mostly centered at the study of its threshold, coherence and the generation of narrow-band biphotons, we aim at a different aspect of the phenomenon i.e. the correlated spatial modes of the generated biphotons due to the all-optically induced wave-guide in thermal atomic vapor. We use a system with a double- Λ configuration involving hyperfine ground states of ^{85}Rb . The ground state coherence enhances FWM and XPM in the medium and hence facilitates the generation of guided single spatio-temporal modes via MOPO with high input field conversion efficiency. In this chapter, we discuss the theory, experimental details, and results for the demonstration of MOPO under the effect of the all-optical waveguide.

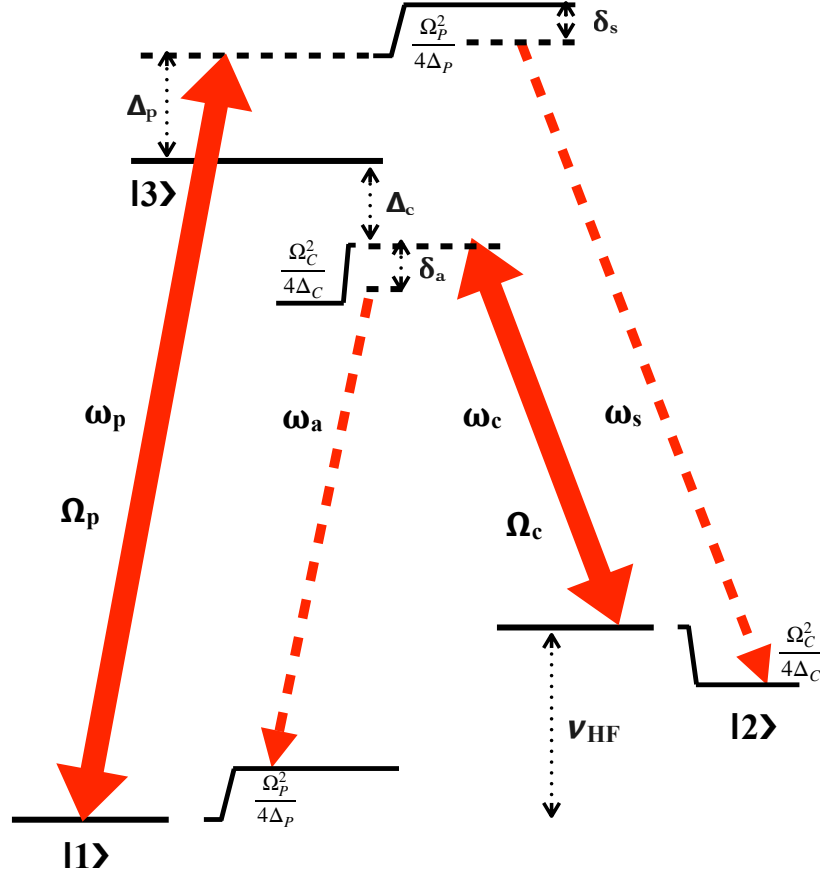


Figure 4.1: Schematic of energy level diagram with the coupling of the input pump and control laser fields (solid lines) and the generated Stokes and anti-Stokes fields (dashed lines).

4.1 Principle of FWM-based MOPO

If the nonlinear interaction of two counter-propagating driving fields is efficient, then it can lead to the onset of parametric oscillation in the system. For the case of $\chi^{(3)}$ medium, the phenomenon results in the generation and amplification of a pair of fields i.e. Stokes and anti-Stokes fields from vacuum fluctuations. The input strong fields called the pump and the control fields undergo spontaneous FWM resulting in the internal feedback mechanism required for the MOPO process. The phase-matching condition ensures the generation of the Stokes and the anti-Stokes beams to be along the pump and the control beam directions respectively.

The schematic of the energy level diagram for MOPO process is shown in Fig. 4.1. The system has a double- Λ configuration with two hyperfine ground states $|1\rangle$, $|2\rangle$ and two virtual excited states, which are detuned from the state $|3\rangle$. The process involves interaction of the pump laser field of Rabi frequency Ω_p , optical frequency ω_p and detuning Δ_p with the atomic

transition $|1\rangle \rightarrow |3\rangle$. Similarly, the control laser field with Rabi frequency Ω_c , optical frequency ω_c and detuning Δ_c interacts with the atomic transition $|2\rangle \rightarrow |3\rangle$. The Stokes and the anti-Stokes beams are emitted from the corresponding virtual states with the respective two-photon detunings given as, $\delta_s = \omega_s - \omega_p + \Delta_{LS} + \nu_{HF}$ and $\delta_a = \omega_a - \omega_c - \Delta_{LS} - \nu_{HF}$, where $\Delta_{LS} = \frac{\Omega_c^2}{4\Delta_c} - \frac{\Omega_p^2}{4\Delta_p}$ is the light shift due to the strong pump and the control fields whereas ν_{HF} is the splitting of the hyperfine ground states $|1\rangle$ and $|2\rangle$. The energy conservation associated with the FWM process i.e. $\omega_s + \omega_a = \omega_p + \omega_c$ ensures that $\delta_s + \delta_a = 0$.

4.2 Experimental details

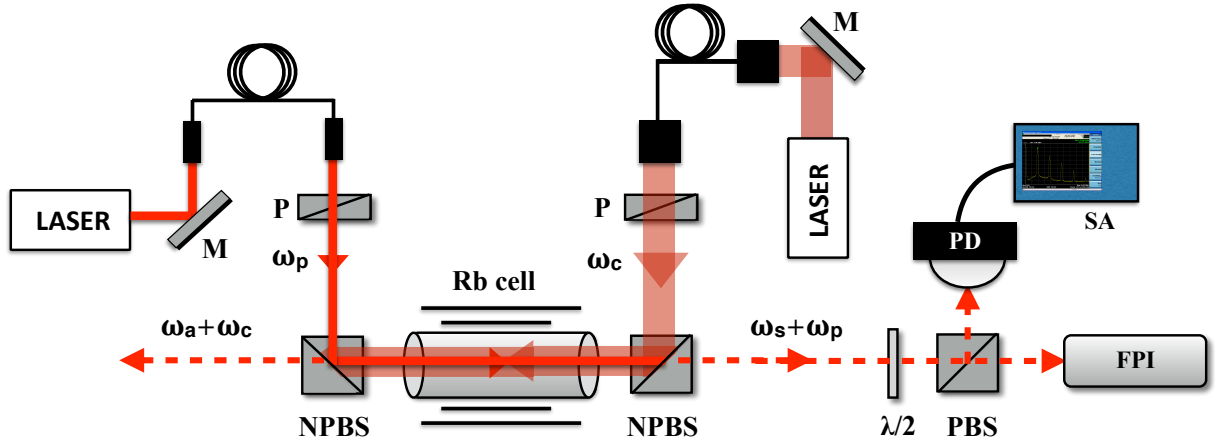


Figure 4.2: Schematic of the experimental setup. PBS: Polarising beam splitter, P: Polariser, M: Mirror, NPBS: Non-polarising beam splitter, PD: Photo-detector, SA: Spectrum analyser, FPI: Fabry-Perot Interferometer.

The schematic of the experimental setup is shown in Fig. 4.2. The input beams are derived from two external cavity diode lasers and are passed through single-mode fibers for spatial mode filtering. The experiment is performed with ^{85}Rb (D2 line), where the pump laser is about 1.2 GHz blue-detuned to the transition $5^2S_{1/2}, F = 2 \rightarrow 5^2P_{3/2}, F' = 3$ and the control laser is detuned to the red of the transition $5^2S_{1/2}, F = 3 \rightarrow 5^2P_{3/2}, F' = 3$ by 800 MHz as shown in Fig 4.3. Both the input beams are made to counter-propagate with each other using two non-polarising beam splitters (NPBS) through a 5 cm long vapor cell with rubidium in its natural abundance. The cell is enclosed by two layers of magnetic shields to avoid magneto-optic rotation of the strong beams (Appendix C). The temperature of the vapor cell is optimised for the signal, which is kept between $110^0 - 120^0$ C using a controlled heater with the corresponding

number density of approximately 10^{13} cm^{-3} . Both the strong fields are linearly polarised in the same polarization direction and the generated fields are found to be orthogonally polarised to the input beams. A polarising beam splitter (PBS) is used to split the output beam into two parts. One part is collected in a fast photodetector and is analyzed using a spectrum analyzer. Another part is directed into a Fabry-Perot interferometer. $\frac{1}{e}$ radii of the pump and the control beams used in the experiment are $200 \mu\text{m}$ and 1 mm respectively.

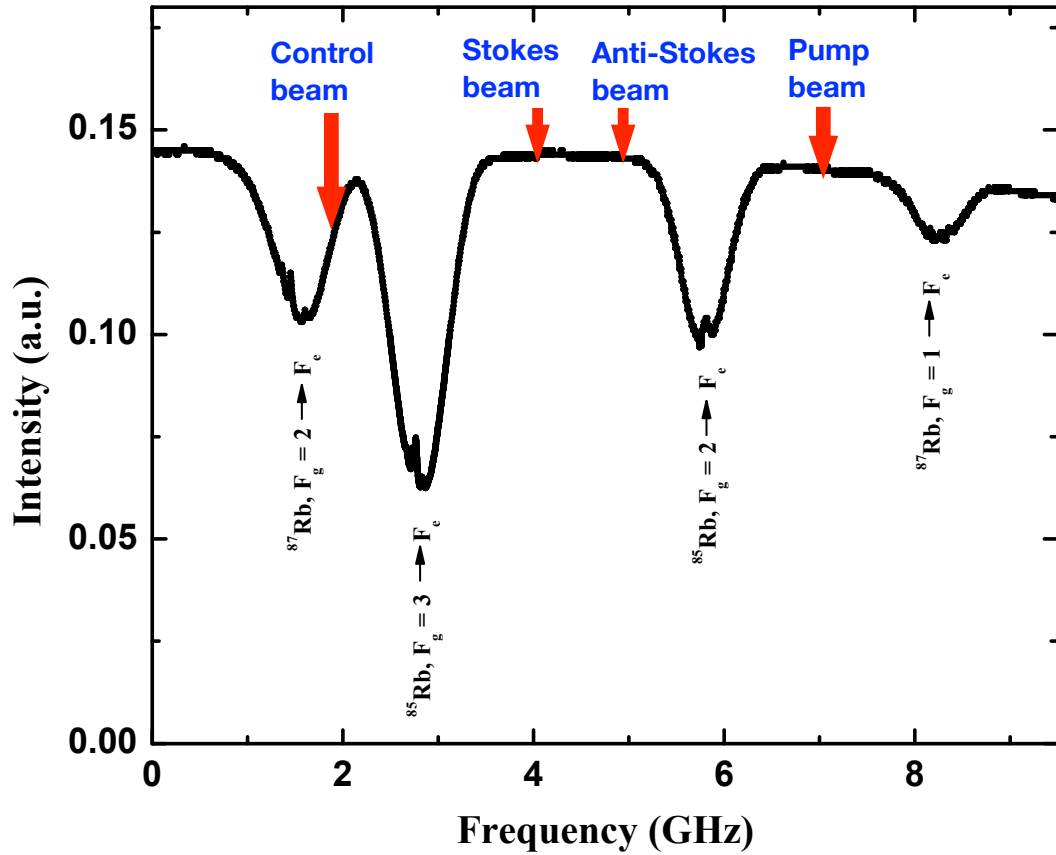


Figure 4.3: The frequencies of the input as well as the generated beams depicted in Rb absorption spectrum. The Stokes beam being generated outside the Doppler linewidth does not undergo absorption and hence is used for analysis.

4.3 Preliminary experimental results

As illustrated in Fig. 4.2, the output beams after the exit faces of the cell contain the corresponding generated as well as the input beams. We analyze the output beam from one of the exit faces (pump beam direction) for confirmation of the MOPO process. The half-wave plate

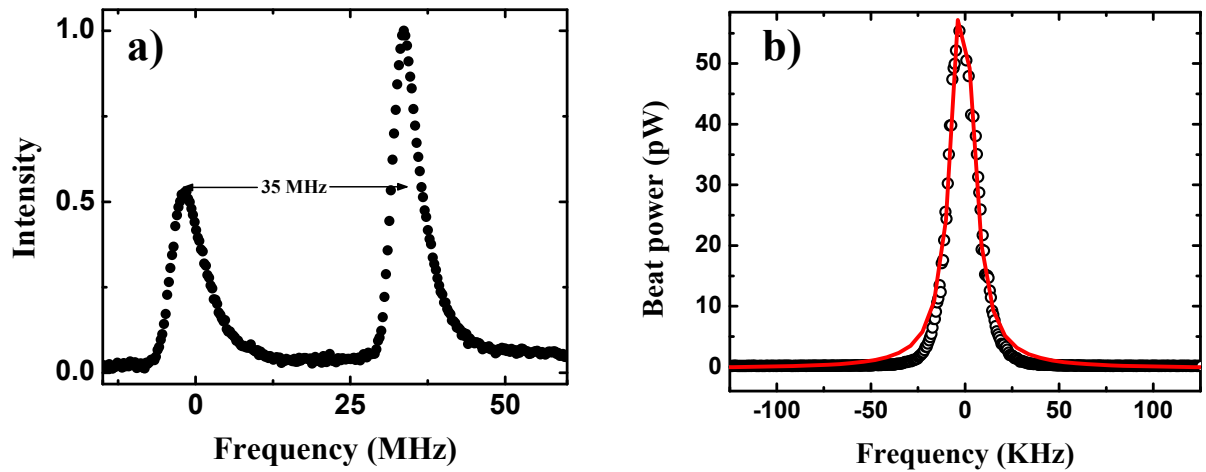


Figure 4.4: a) Fabry-Perot cavity signal, which shows the frequency difference of about 35 MHz between the pump and the Stokes beam. b) Spectrum analyzer signal showing the beat frequency between the pump and the Stokes beam. Black circles denote the experimental data and the red lines correspond to the Lorentzian fitting with a width of 14 kHz.

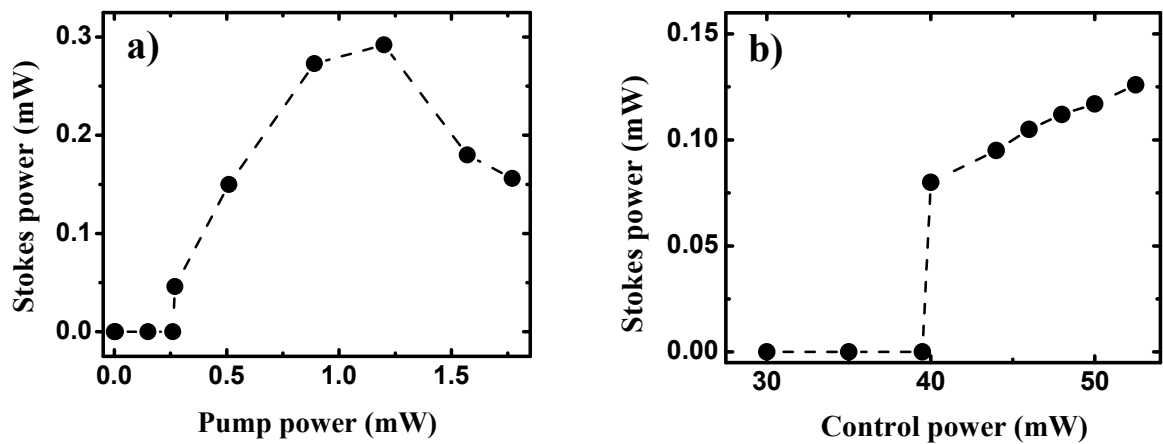


Figure 4.5: a) Stokes power variation with input pump power, where the control power is fixed at 54 mW b) Stokes power variation with input control power. The pump power is fixed at 1.6 mW.

before the PBS allows us to analyze the output beam along different polarization directions. We rotate the wave-plate to an angle such that each port of PBS contains a contribution from both pump and Stokes beams. A Fabry-Perot interferometer (FPI) is used to measure the frequency difference between the pump and the Stokes beam. Fig. 4.4 (a) shows a typical FPI signal for near-threshold MOPO, where the smaller peak corresponds to the pump beam leaked through the PBS and the larger peak is due to the generated beam. It is confirmed by the fact that when the control beam is turned off, the larger peak disappears and there is an increase in the smaller peak height. We use an FPI with a free spectral range of 1 GHz. So, the measured frequency difference of ~ 35 MHz between the peaks confirms the generated Stokes beam to be frequency-separated from the pump beam by the hyperfine difference of ~ 3.035 GHz. The broad cavity signal is a consequence of the mismatch of the cavity length (out of confocality).

As a further confirmation of the MOPO process, we observe the beat signal between the pump and the Stokes beams using a fast photodetector connected to a spectrum analyzer as shown in Fig 4.2. A typical beat signal is depicted in Fig 4.4 (b). The experimental data are fitted with a Lorentzian function and the linewidth is found to be ~ 14 kHz. The observed beat frequency of 3.03314 GHz in this case is due to the factor, $\omega_p - \omega_s = \nu_{\text{HF}} + \Delta_{\text{LS}} - \delta_s$. We also measure the beat signal between the control and anti-Stokes beam simultaneously, which is found to be of the same linewidth and center frequency as that for the pump and Stokes beam. We present the frequencies of the input as well as generated beams due to the MOPO process in the rubidium absorption spectrum as shown in Fig. 4.3.

When the half-wave plate is rotated to pump polarisation direction, we do not observe the peak corresponding to the Stokes beam. It is thus inferred that there is no mirrorless oscillation along the input polarisation direction. Here, MOPO generation along the orthogonal polarization direction is not understood theoretically and hence further experiments are carried out based on this experimental observation. Also, we do not observe the generation when the input fields are orthogonally polarised to each other.

The pump threshold power is found to be $270 \mu\text{W}$ ($\Omega_p = 30$ MHz) when the control power is fixed at 54 mW ($\Omega_c = 140$ MHz). In this case, The Rabi frequencies are estimated using, $\Omega = \Gamma_{eg} \sqrt{\frac{I}{2I_s}}$, where I_s is the saturation intensity and Γ_{eg} is the population decay rate from the excited state. For, ^{85}Rb , $I_s = 2.5 \text{ mW/cm}^2$ and $\Gamma_{eg} = 6$ MHz. We study the Stokes power variation with increasing input pump and control power as shown in Fig. 4.5 (a) and (b) respectively. The features show a linear increase in the Stokes power with the input beam

power variation after the threshold and hence confirming the mirrorless lasing. The decrease in Stokes power with high pump power as shown in Fig. 4.5(a) is a consequence of the multimode regime of MOPO, which is explicitly discussed later in the chapter. It is also observed that an increase in the input control power leads to the increase in the pump threshold power for the process, which is in accordance with the threshold condition derived in reference [11].

To characterize the fields generated via MOPO, we have to investigate different nonlinear processes experienced by them. In the following section, we discuss the theoretical model for the estimation of nonlinear processes in the medium and the propagation equations for the generated fields.

4.4 Theoretical model

4.4.1 XPM of the generated fields due to the pump and the control fields

The generated fields experience cross-phase modulation due to the strong input beams. To estimate this XPM, we present the semi-classical model by considering a system of four levels interacting with a pump, control and probe field. Here, one of the generated beams of the MOPO process is considered as the probe field with Rabi frequency Ω_e and the effect of the other generated field is neglected by considering it to be weak. The pump and control fields are counter-propagating and depending on whether the probe field signifies the Stokes field or the anti-Stokes field, its direction is chosen accordingly. The single-photon detunings for the pump, control, and probe fields are given by Δ_p , Δ_c and Δ_e respectively. Δ is defined as, $\Delta_e - \Delta_p$ and is related to δ_s and δ_a as defined in section 4.1 by $\Delta = \delta_s - \Delta_{LS} = -(\delta_a + \Delta_{LS})$, as shown in Fig. 4.6(a). Similar systems have been analyzed to study the narrow resonance with gain as well as the dispersion of the probe beam [36, 37] and also for optical steering, cloning and splitting of probe beam [38].

With the semi-classical approach and rotating-wave approximation, the Hamiltonian of the four level system is given by,

$$\hat{H} = -\hbar/2 \begin{pmatrix} 0 & 0 & \Omega_p^* & 0 \\ 0 & -2\Delta & \Omega_e^* & \Omega_c^* \\ \Omega_p & \Omega_e & 2\Delta_p & 0 \\ 0 & \Omega_c & 0 & 2(\Delta_c - \Delta) \end{pmatrix}.$$

The time evolution of the system is described by the master equation as

$$i\hbar \frac{d\hat{\rho}}{dt} = [\hat{H}, \hat{\rho}] + i\hbar \hat{\mathcal{L}}_D, \quad (4.1)$$

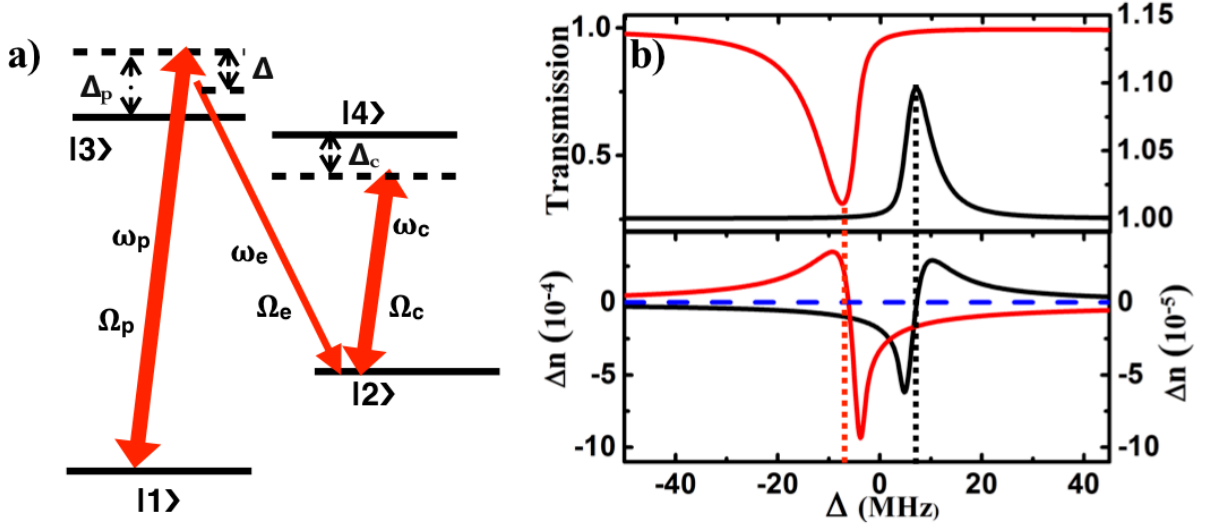


Figure 4.6: a) Energy level configuration with four levels used for the theoretical model. b) Transmission and nonlinear refractive index (Δn) of the generated beams. The red solid line corresponds to the anti-Stokes beam and the black solid line corresponds to the Stokes beam. We present the scaling for the anti-Stokes and Stokes beam in the left-axis and right axis of the graph respectively. The blue dotted line represents the line of null refractive index.

with

$$\hat{\mathcal{L}}_D = \begin{pmatrix} \Gamma_{31}\rho_{33} + \Gamma_{41}\rho_{44} & -\gamma_c\rho_{12} & -\gamma_{31}\rho_{13} & -\gamma_{41}\rho_{14} \\ -\gamma_c\rho_{21} & \Gamma_{32}\rho_{33} + \Gamma_{42}\rho_{44} & -\gamma_{32}\rho_{23} & -\gamma_{42}\rho_{24} \\ -\gamma_{31}\rho_{31} & -\gamma_{32}\rho_{32} & -(\Gamma_{31} + \Gamma_{32})\rho_{33} & -\gamma_{43}\rho_{34} \\ -\gamma_{41}\rho_{41} & -\gamma_{42}\rho_{42} & -\gamma_{43}\rho_{43} & -(\Gamma_{41} + \Gamma_{42})\rho_{44} \end{pmatrix}.$$

Here $\gamma_{31} = \gamma_{32} = \frac{\Gamma_{31} + \Gamma_{32}}{2}$, $\gamma_{41} = \gamma_{42} = \frac{\Gamma_{41} + \Gamma_{42}}{2}$, $\gamma_{43} = \frac{\Gamma_{31} + \Gamma_{32} + \Gamma_{41} + \Gamma_{42}}{2}$. $\hat{\rho}$ is the density matrix operator and $\hat{\mathcal{L}}_D$ is the Lindblad operator, which describes all the decay and dephasing rates present in the medium. $\Gamma_{31} = \Gamma_{32} = \Gamma_{41} = \Gamma_{42} = 2\pi \times 6$ MHz are the population decay rates from the excited states to the ground states. $\gamma_c \sim 1$ MHz is the dipole dephasing rate associated with the ground states and it is dominated by the transit time of the thermal atoms through the interacting beams.

The time-evolution of the density matrix elements are given by the following equations.

$$\dot{\rho}_{11} = \frac{i}{2}(\Omega_p^* \rho_{31} - \Omega_p \rho_{13}) + \Gamma_{31} \rho_{33} + \Gamma_{41} \rho_{44}, \quad (4.2)$$

$$\dot{\rho}_{22} = \frac{i}{2}(\Omega_e^* \rho_{32} - \Omega_e \rho_{23} + \Omega_c^* \rho_{42} - \Omega_c \rho_{24}) + \Gamma_{32} \rho_{33} + \Gamma_{42} \rho_{44}, \quad (4.3)$$

$$\dot{\rho}_{33} = \frac{i}{2}(\Omega_e \rho_{23} - \Omega_e^* \rho_{32} + \Omega_p \rho_{13} - \Omega_p^* \rho_{31}) - (\Gamma_{31} + \Gamma_{32}) \rho_{33}, \quad (4.4)$$

$$\dot{\rho}_{44} = \frac{i}{2}(\Omega_c \rho_{24} - \Omega_c^* \rho_{42}) - (\Gamma_{41} + \Gamma_{42}) \rho_{44}, \quad (4.5)$$

$$\dot{\rho}_{12} = \frac{i}{2}(\Omega_p^* \rho_{32} - \Omega_e \rho_{13} - \Omega_c \rho_{14} + 2\Delta \rho_{12}) - \gamma_c \rho_{12}, \quad (4.6)$$

$$\dot{\rho}_{13} = \frac{i}{2}(\Omega_p^* (\rho_{33} - \rho_{11}) - \Omega_e^* \rho_{12} - 2\Delta_p \rho_{13}) - \gamma_{31} \rho_{13}, \quad (4.7)$$

$$\dot{\rho}_{14} = \frac{i}{2}(\Omega_p^* \rho_{34} - \Omega_c^* \rho_{12} - 2(\Delta_c - \Delta) \rho_{14}) - \gamma_{41} \rho_{14}, \quad (4.8)$$

$$\dot{\rho}_{23} = \frac{i}{2}(\Omega_e^* (\rho_{33} - \rho_{22}) + \Omega_c^* \rho_{43} - \Omega_p^* \rho_{21} - 2(\Delta_p + \Delta) \rho_{23}) - \gamma_{32} \rho_{23}, \quad (4.9)$$

$$\dot{\rho}_{24} = \frac{i}{2}(\Omega_c^* (\rho_{44} - \rho_{22}) + \Omega_e^* \rho_{34} - 2\Delta_c \rho_{24}) - \gamma_{42} \rho_{24}, \quad (4.10)$$

$$\dot{\rho}_{34} = \frac{i}{2}(\Omega_p \rho_{14} - \Omega_c^* \rho_{32} + \Omega_e \rho_{24} + 2\Delta \rho_{34}) - \gamma_{43} \rho_{34}. \quad (4.11)$$

With

$$\rho_{11} + \rho_{22} + \rho_{33} + \rho_{44} = 1.$$

These optical Bloch equations of the density matrix elements are numerically solved in steady state. The effective susceptibility $\chi^{(eff)}$ of the weak probe beam is related to ρ_{32} as $\chi^{(eff)} = \frac{2N\mu^2}{\epsilon_0 \hbar \Omega_e} \rho_{32}$, where N is the number density and μ is the atomic dipole moment. The nonlinear susceptibility of the weak probe beam due to XPM, $\chi_{XPM}^{(eff)}$ is evaluated from $\chi^{(eff)}$ by subtracting the linear term. Considering the Doppler broadening in the medium, the laser detunings Δ_p , Δ_c and Δ_e are modified as $\Delta_p - k_p v$, $\Delta_c + k_c v$ and $\Delta_e - k_e v$ respectively, where v is the velocity and k_p , k_c , k_e are the wave vectors of the pump, control and probe fields respectively. The nonlinear susceptibility of the weak probe beam due to XPM, $\chi_{XPM}^{(eff)}$, evaluated under the steady state condition is doppler-averaged to include the effect of the velocities of the atoms. Here, the imaginary and the real part of the susceptibility respectively provide information about the nonlinear gain or absorption and nonlinear refractive index as experienced by the generated fields. As for the case of anti-Stokes beam, the roles of the pump and control beams are interchanged in the model.

We have calculated the transmission and nonlinear refractive index of the Stokes and anti-Stokes beams as presented in Fig. 4.6(b). The theoretical parameters are $\Omega_p = 2\pi \times 60$ MHz,

$\Omega_c = 2\pi \times 140$ MHz, $\Delta_p = 2\pi \times 1.2$ GHz, $\Delta_c = -2\pi \times 800$ MHz, $v_p = 270$ m/s and $N = 10^{13}$ cm $^{-3}$. The Stokes beam is found to experience gain whereas the anti-Stokes beam undergoes absorption. However, both the beams can experience positive refractive index, which can lead to optically induced waveguiding effect.

4.4.2 Experimental verification of the model

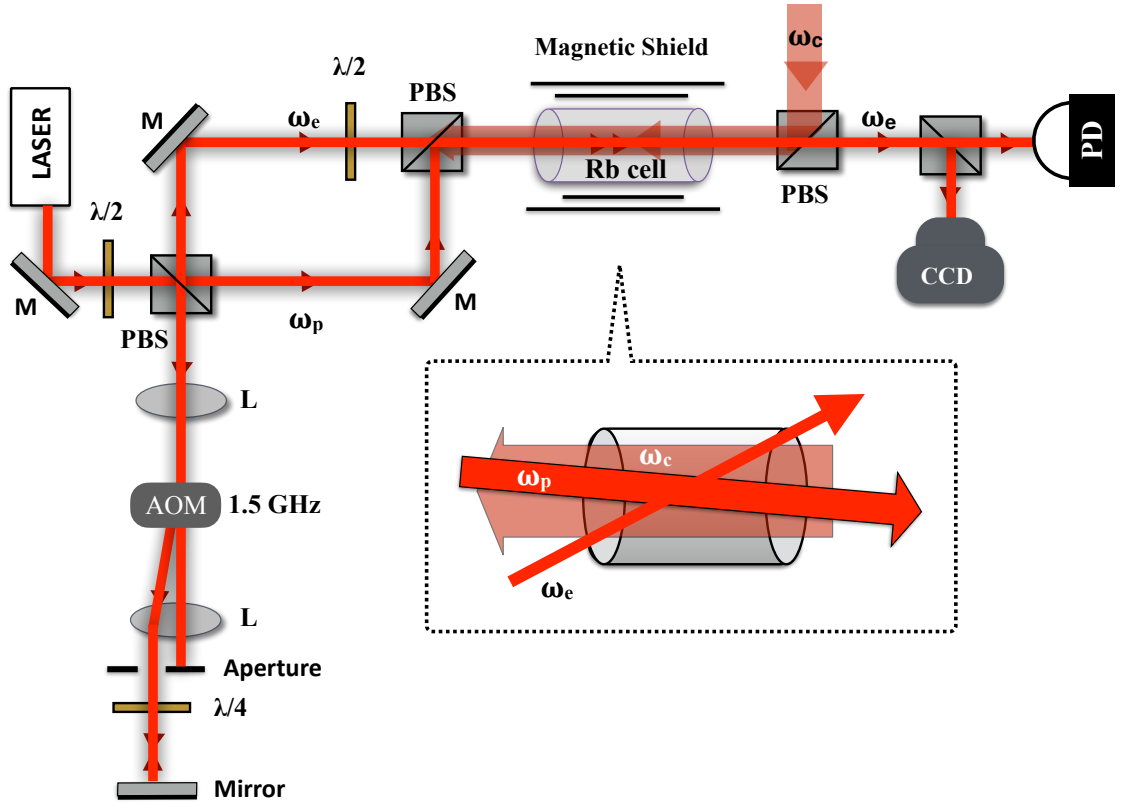


Figure 4.7: Schematic of the experimental setup for probe transmission in N-type system. M: Mirror, L: Lens, PBS: Polarising beam splitter, PD: Photo-detector.

To experimentally investigate the XPM experienced by the generated beams, we perform an experiment using an external probe in the MOPO configuration of counter-propagating pump and control beams. The schematic of the experimental setup is presented in Fig. 4.7. The probe and the pump beams are derived from the same laser. The frequency separation of 3.035 GHz is achieved by an AOM operating at 1.5 GHz in a double-pass configuration. The probe and the pump beams are mixed using a PBS and a half-wave plate is used to control the corresponding intensities. The polarization of the pump and control beams are linear in the same direction while the probe beam is orthogonally polarised to the strong beams. The strong beams are

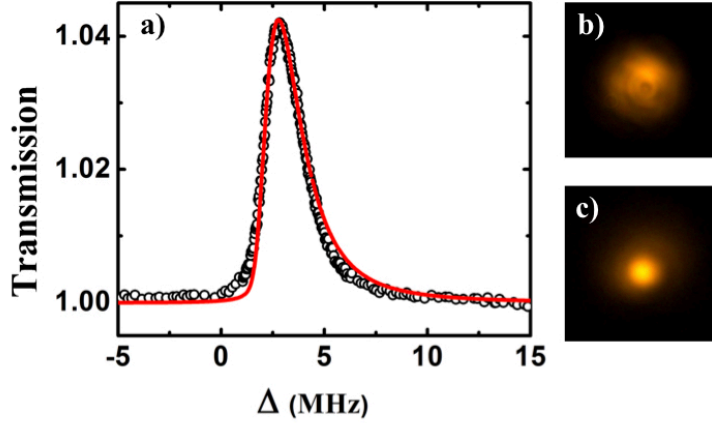


Figure 4.8: a) Matching of the experimentally measured and the theoretically calculated transmission of the external probe beam. The black circles denote the experimental data and the red solid line represents the data from the theoretical model. The CCD images of the probe beam for b) lower and c) higher value of Δ . The scales of both the images are same.

slightly misaligned by $\sim 1^\circ$ to avoid the MOPO process. A part of the transmitted probe light is collected using a photo-detector and is analyzed using an oscilloscope. We measure the probe absorption or gain in the medium by scanning the probe frequency using the AOM. Another part of the beam is directed into a CCD camera.

We observed that in the absence of the control beam, the probe transmission shows an absorptive feature due to two-photon absorption whereas it becomes a gain in the presence of the control beam. The model is verified by comparing the theoretical calculation with the experimentally measured transmission of the external probe beam coupling the system. We observe that the model shows a good agreement with the experimental result as shown in Fig. 4.8(a). We also observe the probe beam profiles by scanning the two-photon detuning Δ along the gain profile. The probe beam is found to be defocused for a lower value of Δ than the peak value i.e for the negative value of the refractive index (Δn). Similarly, for the higher value of Δ corresponding to a positive Δn , the probe beam is found to be focused. The CCD images of the probe beam for both the cases are presented in Fig. 4.8 (b) and (c). Here both the images are in the same scale and they are used to illustrate the focusing and defocusing of the input probe beam due to the medium. This is the preliminary experimental observation of the waveguiding mechanism present in the system.

In the next section, we derive the propagation equations for the generated fields by incorporating the calculated XPM from the model and discuss how the equations speculate the

generation of different spatial modes of light.

4.4.3 Wave-equations for the generated fields

The wave equation of the Stokes field propagating along the z-direction with the radial transverse coordinate r is given as,

$$\nabla^2 E_s(r) + \frac{\omega_s^2}{c^2} (1 + \chi_s^{(1)}) E_s(r) = \frac{-\omega_s^2}{\epsilon_0 c^2} P^{(NL)}(r).$$

$P^{(NL)}(r) = 3\epsilon_0 \chi_{\text{XPM}}^{(eff)}(r) E_s + 3\epsilon_0 \chi_{\text{FWM}}^{(3)} E_p E_c E_a$ is the non-linear polarization of the medium oscillating with frequency ω_s of the Stokes field, $\chi_{\text{FWM}}^{(3)}$ is the nonlinear susceptibility of the Stokes beam due to FWM and $\chi^{(1)}$ is the linear susceptibility, which is related to the linear refractive index as, $n_s = \sqrt{1 + \chi_s^{(1)}}$. The electric field amplitudes in the propagation equation are replaced with, $E_i(z) = A_i(z) e^{\pm i n_i k_i z}$, $i=p,c,s,a$ where k_i is the wave-vector and n_i is the linear refractive index associated with the corresponding field. Using the slowly varying amplitude approximation, the wave equation can be reduced to

$$i \frac{dA_s}{dz} + \frac{\nabla_T^2}{2k_s} A_s + i\alpha_s A_s + \frac{3}{2} k_s \text{Re} \left(\chi_{\text{XPM}}^{(eff)}(r) \right) A_s + \frac{3}{2} k_s \chi_{\text{FWM}}^{(3)} A_p A_c A_a^* e^{i\Delta k z} = 0. \quad (4.12)$$

Similarly for the anti-Stokes field,

$$-i \frac{dA_a}{dz} + \frac{\nabla_T^2}{2k_a} A_a + i\alpha_a A_a + \frac{3}{2} k_a \text{Re} \left(\chi_{\text{XPM}}^{(eff)}(r) \right) A_a + \frac{3}{2} k_a \chi_{\text{FWM}}^{(3)} A_p A_c A_s^* e^{i\Delta k z} = 0. \quad (4.13)$$

Here, $\Delta k = n_p k_p - n_c k_c - n_s k_s + n_a k_a$ is the linear phase-mismatch in the system. $\alpha_{s,a} = \frac{k_{s,a}}{2} \text{Im} \left(\chi_s^{(1)} + 3\chi_{\text{XPM}}^{(eff)} \right)$ accounts for the gain/absorption of the generated beams in the medium.

Because of the Gaussian profiles of the pump and the control fields, $\text{Re}(\chi_{\text{XPM}}^{(eff)}(r))$ gives rise to spatially varying nonlinear refractive indices ($\Delta n(r)$) for both the generated fields. Using the theoretical model, $\Delta n(r)$ for the Stokes and the anti-Stokes fields are evaluated for $r = 0$ and are presented in Fig. 4.9 (a) and (d) as functions of the respective laser detunings. If δ_s is positive, the energy conservation i.e. $\delta_s = -\delta_a$ implies that both the Stokes and the anti-Stokes fields experience a positive nonlinear refractive index as specified by the blue points in Fig. 4.9 (a) and (d).

The refractive index patterns are expected to be nearly Gaussian in nature leading to waveguiding of the generated beams via MOPO. The spatial modes of the generated fields under the

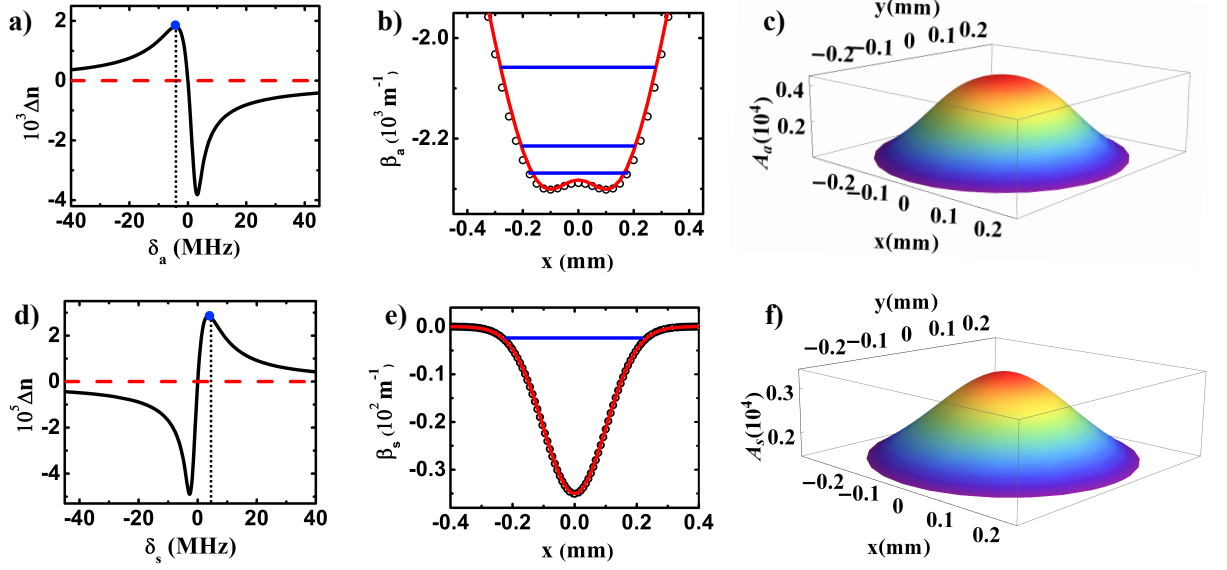


Figure 4.9: Nonlinear refractive index (Δn) as a function of the two-photon detuning, a) δ_a for anti-Stokes and d) δ_s for Stokes fields. Approximate Gaussian potentials experienced by the b) anti-Stokes and e) Stokes fields. The black circles denote the potentials evaluated from the theoretical model and the red solid line represents the functional fitting of the form, $c_1(-e^{-x^2/(\Delta x_c)^2} + c_2 e^{-x^2/(\Delta x_p)^2})$ and $c_3(-e^{-x^2/(\Delta x_p)^2})$ for the anti-Stokes and Stokes beams respectively. Here, $c_1 = 2.4 \times 10^3 \text{ m}^{-1}$, $c_2 = 0.065$, $c_3 = 3.5 \times 10^2 \text{ m}^{-1}$, $\Delta x_c = 680 \text{ }\mu\text{m}$ and $\Delta x_p = 142 \text{ }\mu\text{m}$. The horizontal blue solid lines on the potentials refers to the corresponding theoretically calculated eigenvalues. The normalized ground-state eigenfunction of the waveguide for the case of c) anti-Stokes field and f) Stokes fields.

effect of the all-optical waveguides can be studied using their propagation equations through the nonlinear medium. In this case, the transverse sizes of the generated beams would be much smaller than that of the control and pump beams for the lowest order modes of the all-optical waveguides. Therefore, the input strong fields can be approximated as the plane waves and hence, the gain as a result of the four-wave mixing as well as the nonlinear absorption process would give rise to a uniform gain/loss in the transverse direction of the generated fields. So, in this approximation, the spatial profiles of the generated fields are mostly decided by the all-optical waveguide at least for the case of the lowest order modes. To determine the transverse modes of the generated fields, only the nonlinear refractive index due to XPM is considered in equation (4.12) and (4.13) to get

$$i \frac{dA_s}{dz} = -\frac{1}{2k_s} \nabla_T^2 A_s + V_s(r) A_s = \beta_s A_s, \quad (4.14)$$

$$-i \frac{dA_a}{dz} = -\frac{1}{2k_a} \nabla_T^2 A_a + V_a(r) A_a = \beta_a A_a, \quad (4.15)$$

where $V_{s,a}(r) = -\Delta n_{s,a}(r) k_{s,a}$ are the near-Gaussian potentials as experienced by the Stokes and the anti-Stokes fields. We theoretically evaluate the values of $V_{s,a}(r)$ from the model by considering the Gaussian profiles of the pump and control beams at the specified values of δ_s and δ_a as shown in the respective figures. With input beam sizes of 200 μm and 1 mm for the pump and control beams, the calculation results in near-Gaussian refractive index patterns of radii 142 μm and 680 μm for the Stokes and anti-Stokes beams respectively. The theoretically calculated potentials are presented in Fig. 4.9 (b) and (e) with parameters, $\Omega_p = 30$ MHz, $\Omega_c = 140$ MHz.

Numerical solution of 2D isotropic Gaussian potential in polar co-ordinates

The above equation (4.14) and (4.15) resemble the Schrödinger's equation for a two-dimensional Gaussian potential with eigenvalues $\beta_{s,a}$.

Multiplying $2k_{s,a}$ on both sides of the equation (4.13), we get

$$-\nabla_T^2 A_{s,a} + U_{s,a}(r) A_{s,a} = \beta'_{s,a} A_{s,a},$$

where the notations used are $U_{s,a}(r) = 2k_{s,a} V_{s,a}(r)$ and $\beta'_{s,a} = 2k_{s,a} \beta_{s,a}$. Using separation of variables method, $A_{s,a} = R(r)\Phi(\phi)$ we get two separate equations as;

$$\begin{aligned} [-r^2 \frac{d^2}{dr^2} + r \frac{d}{dr} + r^2(U_{s,a}(r) - \beta'_{s,a})] R(r) &= -l^2 R(r). \\ \frac{d^2}{d\phi^2} \Phi(\phi) &= -l^2 \Phi(\phi) \implies \Phi(\phi) = e^{\pm il\phi}. \end{aligned}$$

Now for the radial equation, the regular solution is of the form, $R(r) = r^l \mathcal{R}(r)$. So the modified radial equation reads as,

$$-\frac{d^2 \mathcal{R}}{dr^2} + \frac{(2l+1)}{\mathcal{R}} \frac{d\mathcal{R}}{dr} + U_{s,a}(r) \mathcal{R} = \beta'_{s,a} \mathcal{R},$$

with $\mathcal{R}(r=0) = 1$ and $\frac{d\mathcal{R}}{dr}|_{r=0} = 0$. We use a simple numerical method to solve the equations to find the eigenvalues of the potentials for both the generated beams. We use the fact that the eigenfunctions becomes zero for $r \rightarrow \infty$. So we start with an approximate eigenvalue and plot the eigenfunction as a variation of r . The input eigenvalue is changed until the eigenfunction flips its sign i.e. becomes positive to negative. This implies that the eigenfunction goes to

zero for some intermediate value of the eigenvalue. By trial and error, we find the eigenvalue such that the eigenfunction doesn't flip its sign for the largest possible value of radius. This numerical method is found to be very accurate in evaluating the eigenvalues as well as the eigenfunctions.

The numerically evaluated eigenvalues for both the potentials are depicted as blue solid lines in Fig. 4.9(b) and (e). The corresponding eigenfunctions for the lowest order modes are also evaluated as shown in Fig. 4.9(c) and (f).

Derivation of equations pertaining to the threshold condition

Considering the generated fields to be excited in one of the eigenmodes of the waveguide, the solution of the spatial modes would be, $A_s = A_{s0}e^{i\beta_s z}$ and $A_a = A_{a0}e^{-i\beta_a z}$ for the counter-propagating Stokes and anti-Stokes fields respectively. Replacing these spatial mode solutions in equation (4.12) and (4.13), we get

$$\frac{dA_{s0}}{dz} + \alpha_s A_{s0} = i\kappa_s A_{a0}^* e^{i\Delta k' z}, \quad (4.16)$$

$$-\frac{dA_{a0}}{dz} + \alpha_a A_{a0} = i\kappa_a A_{s0}^* e^{i\Delta k' z}, \quad (4.17)$$

where $\kappa_{s,a} = \frac{3}{2}k_{s,a}\chi_{\text{FWM}}^{(3)}A_p A_c$ and $\Delta k' = (\beta_a - \beta_s + \Delta k)$. According to the method presented in [6], we use the transform $A_{s0,a0} = \tilde{A}_{s0,a0}e^{\frac{i\Delta k' z}{2}}$ to get the following equations,

$$\frac{d\tilde{A}_{s0}}{dz} + \left(\alpha_s + \frac{i\Delta k'}{2}\right)\tilde{A}_{s0} = i\kappa_s \tilde{A}_{a0}^*, \quad (4.18)$$

$$\frac{d\tilde{A}_{a0}^*}{dz} - \left(\alpha_a + \frac{i\Delta k'}{2}\right)\tilde{A}_{a0}^* = i\kappa_a^* \tilde{A}_{s0}. \quad (4.19)$$

These equations (4.16 and 4.17) resemble the coupled equations for the Stokes and the anti-Stokes fields in the undepleted strong field regime as presented in references [6, 11]. These equations can be solved to calculate the threshold condition of MOPO.

For efficient MOPO under the effect of an all-optical waveguide, the eigenmodes of the waveguide are required to meet the condition of complex phase-matching inside the medium as $(\beta_a - \beta_s + \Delta k) - i(\alpha_s + \alpha_a) = 0$. Apart from the phase-matching condition, a large overlapping integral is also necessary for the efficiency of the process. To understand this, we consider the case of near-threshold MOPO. As shown in Fig. 4.9(b) and (e), the waveguide potential for the

Stokes beam has one spatial eigenmode whereas the anti-Stokes beam potential supports many eigenmodes. For both the waveguides, we plot the ground-state eigenfunctions and found them to be similar as shown in Fig. 4.9(c) and (f), which ensures a large overlapping integral and hence efficient generation.

4.4.4 Observation of spatial modes of the generated fields in the single-mode regime of MOPO

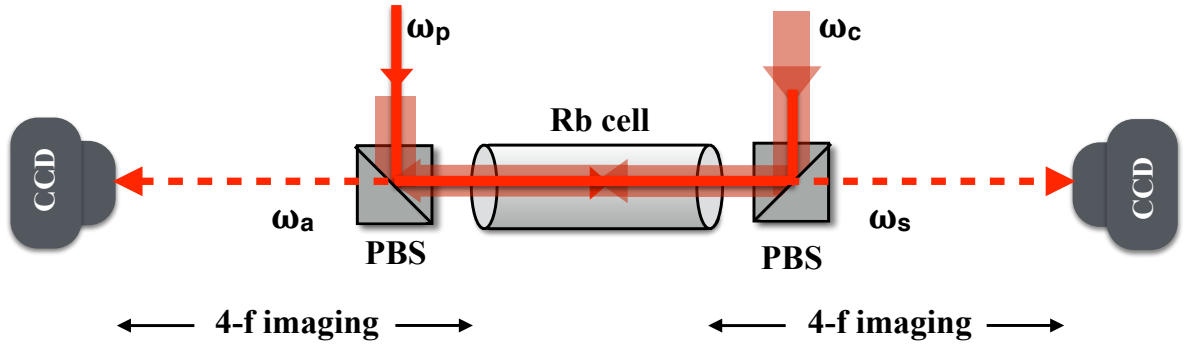


Figure 4.10: Experimental setup for observation of correlated spatial modes. PBS: Polarising beam splitter.

We use the 4-f imaging technique (refer to chapter 2) to image the spatial profiles of the generated beams to the CCD camera at the exit faces of the vapor cell in both directions. The control beam power is kept fixed at 54 mW ($\Omega_c = 140$ MHz) and the spatial profiles of the Stokes and anti-Stokes beams are recorded by varying the input pump beam power. It is observed that with pump power as low as $\simeq 270 \mu\text{W}$ ($\Omega_p = 30$ MHz), the Stokes field with 54 μW is generated in the Gaussian spatial mode. It implies a pump conversion efficiency of $\sim 20\%$ in this mode. This high efficiency is a result of the maximized overlapping integral due to the similar eigenfunctions of the Gaussian mode for both the generated beams as presented in Fig. 4.9 (e) and (f). the CCD images of the Gaussian mode are shown in Fig. 4.11 (a) and (b) whereas the corresponding intensity profiles along the transverse co-ordinate x are depicted in Fig. 4.11 (c) and (d) for the Stokes and anti-Stokes beams respectively. The $\frac{1}{e}$ radii of the generated Gaussian Stokes and anti-Stokes beams are measured to be 97 μm and 147 μm respectively. The different sizes of the generated beams could be due to the fact that they are imaged at different positions of the cell i.e. at the back face and front face of the cell for the Stokes and the anti-Stokes beams respectively. Moreover, the control beam being 800 MHz

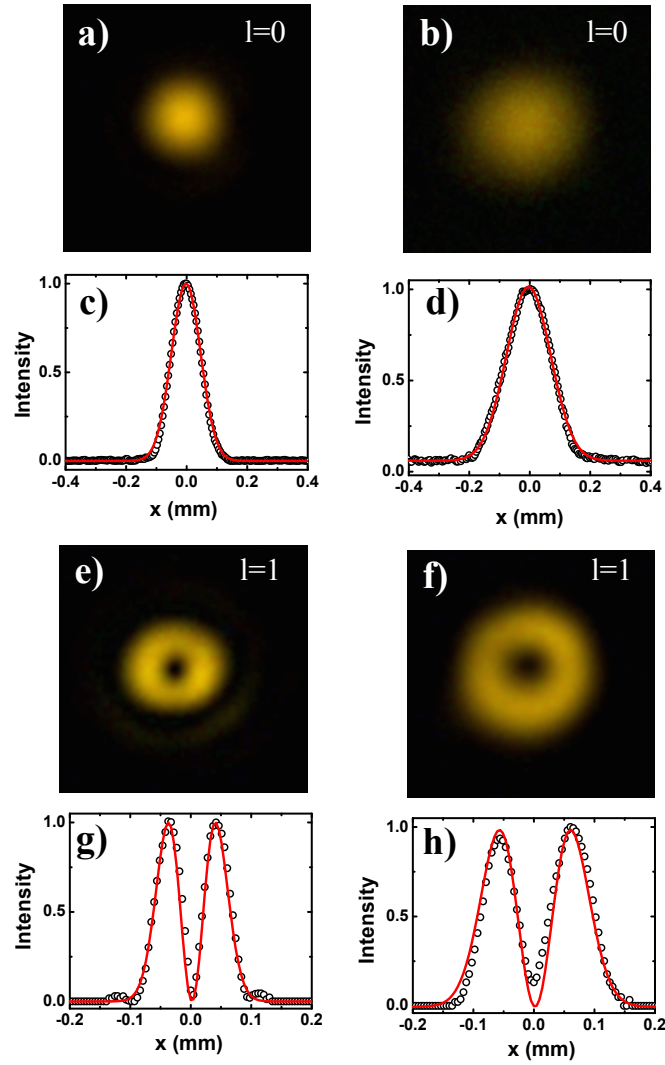
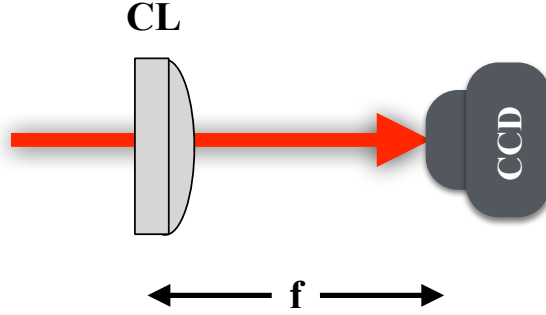
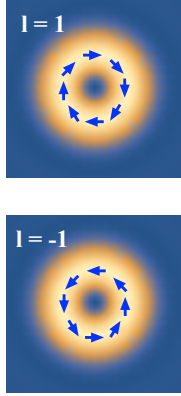


Figure 4.11: CCD images of the symmetric Gaussian mode for a) Stokes and b) anti-Stokes beam. The corresponding transverse intensity patterns for c) Stokes and d) anti-Stokes fields. CCD images of the first-order Laguerre-Gaussian (LG01) mode in the generated e) Stokes and f) anti-Stokes fields. The corresponding transverse intensity profiles for the g) Stokes and h) anti-Stokes fields. The intensity profiles are normalized to the peak value of intensities and are fitted with corresponding Gaussian or Laguerre-Gaussian (LG01) distribution functions.

Incident beam



Beam at focal plane

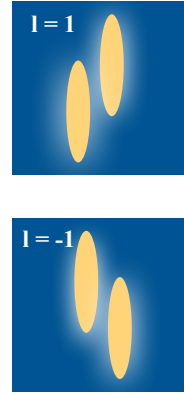


Figure 4.12: Experimental arrangement for determining handedness of the generated LG beams. CL: Cylindrical lens.

red-detuned to the $5^2S_{1/2}, F=3 \rightarrow 5^2P_{3/2}, F'=4$ transition of ^{85}Rb , it falls within the Doppler width of $5^2S_{1/2}, F=2 \rightarrow 5^2P_{3/2}, F'=3$ transition of ^{87}Rb . Hence, it is absorbed while propagating from the back face to the front face of the cell leading to shallower waveguiding potentials for the generated beams. This results in the larger radii of the generated beams on the front face of the cell.

In the same experimental setup, we achieve the excitation of the Laguerre-Gaussian (LG) mode with a pump threshold power $\simeq 900 \mu\text{W}$ ($\Omega_p = 60 \text{ MHz}$) while keeping the control power at 54 mW . Fig. 4.12 (a) and (b) refer to the CCD images of the LG modes in both the generated beams. In this case, we could generate $\simeq 300 \mu\text{W}$ of Stokes power with 33% pump conversion efficiency. Fig. 4.12 (c) and (d) show the transverse intensity patterns for the generated beams, which are fitted with LG distribution function. The $\frac{1}{e}$ radii of the LG Stokes and anti-Stokes beams are found to be $55 \mu\text{m}$ and $83 \mu\text{m}$ respectively.

However, the intensity distribution is not sufficient to confirm LG beam generation and it is essential to investigate the presence of the helical phase structure of $\exp(il\phi)$ in the mode. The typical method to analyze the phase profile of an LG beam is to interfere with another reference beam and their interference pattern, which is spiral for a spherical reference beam and fork-shaped for a plane reference beam confirms the presence of phase singularity of the beam. Another simpler method is based on the use of a single cylindrical lens in the path of the LG beam. In this case, the vortex of the LG beam gets deformed at the focal plane of the lens leading to an extended pattern with tilted dark stripes [39, 40]. This pattern can be

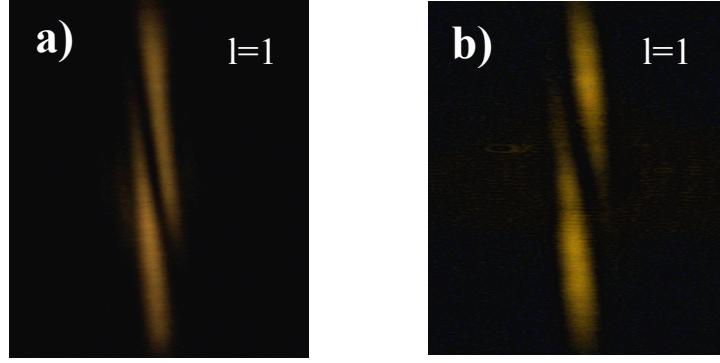


Figure 4.13: Experimental observation of the LG modes in the generated a) Stokes and b) anti-Stokes beams at the focal plane of the cylindrical lens.

understood by solving the paraxial wave-equation of the LG beam multiplied with the lens transmission function [40]. The number of dark stripes equals the magnitude of the vortex charge and the orientation of the stripes provide information about the sign of the vortex charge (l) as illustrated in Fig. 6.3. Hence, we perform this simple measurement by using a cylindrical lens of focal length 100mm in the path of each of the generated LG beams. The CCD images of the Stokes and anti-Stokes beams at the focal plane of the cylindrical lenses are shown in Fig. 4.12 (e) and (f) respectively. The observation of a single dark stripe and its orientation in the same direction for both cases imply that the beams are generated with the same azimuthal index i.e. $l = 1$ for this case. To understand this, we consider the overlapping integral, $\int_{-L/2}^{L/2} \int_0^R \int_0^{2\pi} \rho E_p^* E_c^* E_s E_{as} d\phi d\rho dz$ where L is the length of the sample, R is the aperture size of the system, z is the propagation direction, E_p, E_c, E_s, E_{as} are the electric field amplitudes of the pump, control, Stokes and anti-Stokes fields respectively. The integral over the azimuthal angle, $\int_0^{2\pi} e^{-i(l_s - l_{as})} d\phi = 2\pi\delta(l_s - l_{as})$ for counter-propagating Stokes and anti-Stokes fields leading to same handedness for the LG mode. The selection for left or right-handedness depends mostly on the optical alignment of the input counter-propagating beams.

To understand the excitation of the single spatial mode of the generated LG beams, we consider the pump depletion at the center of the beam due to the high conversion efficiency. This effect modifies the Gaussian Stokes potential by developing a bump at the center. Simultaneously the anti-Stokes potential is modified similarly due to the cross-phase modulation between the strong beams e.g. as shown in Fig. 4.9 (b). Hence, we speculate that the overlapping integral for the lower Gaussian mode is minimized in this case whereas the potentials can favor the oscillation of the Laguerre-Gaussian mode with a better overlapping integral. However, a more

accurate physical interpretation can be done by incorporating the effect of the depletion of the pump and the control fields in the wave equations.

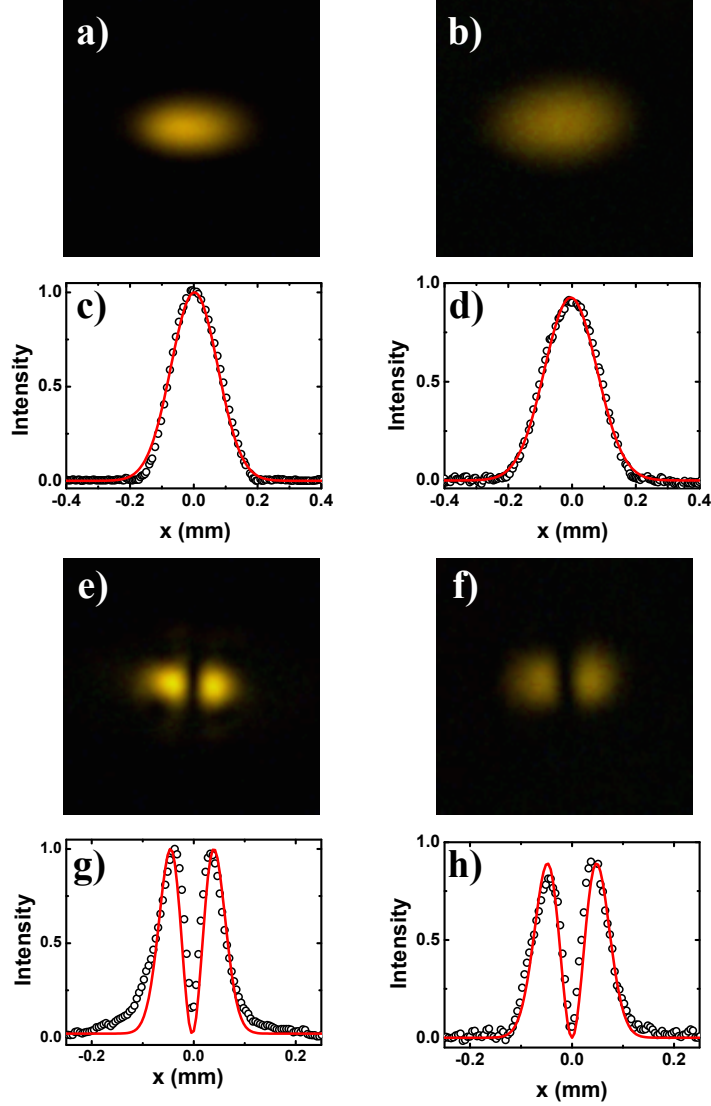


Figure 4.14: CCD images of the asymmetric gaussian mode in the generated a) Stokes and b) anti-Stokes fields. The first-order Hermite-Gaussian (HG01) mode in the generated c) Stokes and d) anti-Stokes fields.

To further verify the effect of waveguiding, the symmetry of the waveguide potential along the transverse directions is broken by using an elliptical pump beam. We use a pair of anamorphic prisms to make the transverse profile of the pump to be elliptic with ellipticity $\simeq 1.5$. We perform the experiment to observe the different spatial modes of the generated beams by varying the pump power. Since the input asymmetric pump beam induces an asymmetric Gaussian potential for the Stokes field, it leads to the generation of asymmetric Gaussian modes near the

threshold as shown in Fig. 4.14 (a) and (b). The intensity patterns along one transverse direction are fitted with Gaussian distribution function and are shown in Fig. 4.14 (c) and (d). In this case, as the cylindrical symmetry of the waveguide is broken, the next higher order eigenmode is the Hermite-Gauss mode. As expected, we observed excitation of the same mode in the experiment with an increase of the pump power. The corresponding CCD images presented in Fig. 4.14 (c) and (d) and the intensity patterns along a transverse direction are shown in Fig. 4.14 (e) and (f). As verified experimentally, the generation of the spatial modes, especially the higher-order modes is critical with regard to the beam sizes as well as the optical alignment of the strong driving fields.

We claim the existence of wave-guiding in the system based on the theoretical model as well as the experimental observation. As explained in the theoretical model, the generated beams experience cross-phase modulation induced refractive index due to the strong beams, which can be positive and hence will lead to the all-optical waveguiding. Experimentally, the wave-guiding for a laser beam is usually verified by the elimination of free-space diffraction. The beam sizes of both the generated beams should be similar inside the medium to achieve maximum overlapping and hence efficient generation. If we consider the LG (Gaussian) beam radius of 55 (97) μm at the back face of the cell as the beam waist, the free space propagation would have resulted in a beam radius of 236 (160) μm at the front face of the cell in the absence of waveguiding. However, we measure a beam radius of 83 (147) μm for the LG beam at the front face. This implies that the beams are not diffracting over the vapor cell length (5 cm), which is larger than the Rayleigh range for the LG beams by a factor of ~ 4 and hence it confirms the presence of the all-optical waveguide in the system.

We also study the free space propagation of the generated fields and the input fields after the vapor cell. We found that the size of the Stokes beam after free-space propagation distance of 50 mm is 340 μm , which is much larger than the size of the pump beam (210 μm). It implies that the Stokes beam is confined within the pump beam inside the vapor cell.

The excitation of different transverse modes in the system obviates the presence of waveguiding. The observation of Hermite-Gaussian mode for the case of the elliptic beam can be understood by considering the fact that the cylindrical symmetry of the all-optical waveguide is broken due to the asymmetric pump beam and leads to the excitation of HG mode. However, this result can not be explained with the four-wave mixing process only.

4.4.5 Multimode regime of MOPO

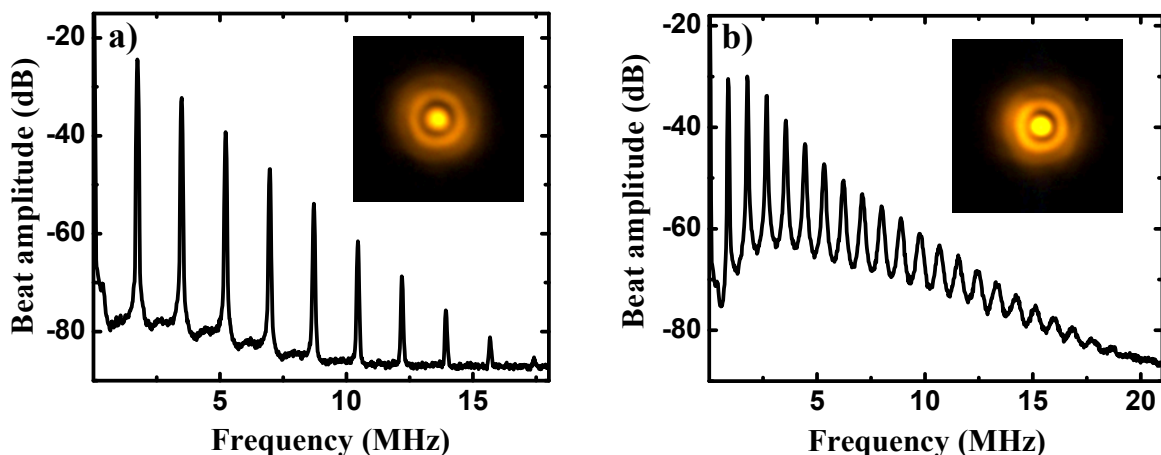


Figure 4.15: Multimode frequency comb signal with pump power a) 1.2 mW and b) 2.5 mW. The inset shows the corresponding transverse profiles of the generated beams.

The multimode excitation in the generated fields of MOPO is observed for pump power far from the threshold value i.e. in the range, $\simeq 1.2 - 3.3$ mW. We experimentally investigate this multimode regime by sending a part of the Stokes beam into a fast photodetector and analyze using a spectrum analyzer. In this regime, there is a generation of at least two different temporal modes of the Stokes beams. These beams have a beam waist of the order of $50 \mu\text{m}$. So the experimentally measured beam power of $\simeq 150 \mu\text{W}$ implies the corresponding Rabi frequency to be as large as 100 MHz. Therefore, the beams undergo efficient forward four-wave mixing due to Zeeman degenerate two-level system [35] and lead to the generation of the equispaced frequency comb. Fig. 4.15 (a) and (b) depicts the spectrum analyzer signal showing the frequency comb with fundamental frequency δ for different pump powers. The value of δ can be varied from hundreds of kHz to a few MHz and it strongly depends on the alignment of the input beams, their Rabi frequencies, and the laser detunings. Under certain parameter conditions, we have observed the simultaneous presence of multiple frequency comb structures, which is due to the generation of three or more longitudinal modes. The same frequency comb structure is also observed in the anti-Stokes beam simultaneously.

We also observe the CCD images of the generated fields in the multimode regime. As expected, the transverse patterns appear like a linear superposition of two or more spatial modes. In this case, also we observe the correlated spatial modes in both the generated beams. The pump conversion efficiency is found to be very low in the multi-mode regime, which is why we

observe a decrease in the Stokes power when the input pump power is increased above 1.2 mW as shown in Fig 4.5(a). This regime is attained near the threshold of MOPO for larger pump beam sizes. For pump beam size $\sim 500 \mu\text{m}$, we could generate Stokes power up to 1 mW in the multimode regime.

4.4.6 Observation of higher order spatial modes

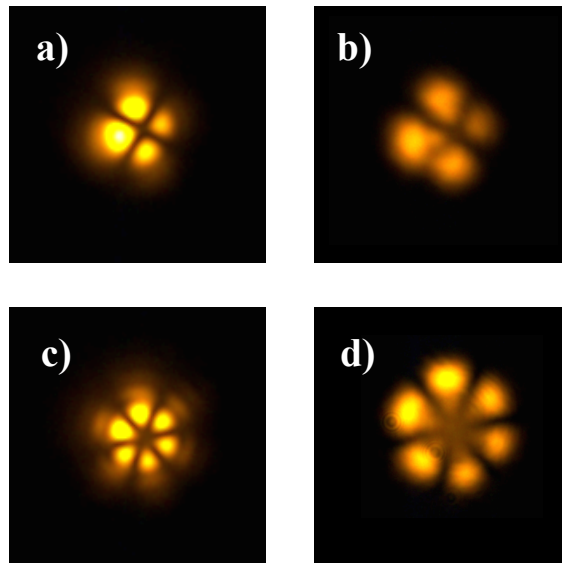


Figure 4.16: CCD images of higher order modes in the generated a), c) Stokes beam and b), d) anti-Stokes beam.

We observe higher-order correlated modes in the generated fields when the pump power was increased beyond the multimode regime. The experimental data are presented in Fig. 4.16. The four-lobe structure was obtained for pump power $\sim 6 \text{ mW}$ and the six-lobe structure was obtained for pump power $\sim 8 \text{ mW}$ when the control power was fixed at 54 mW. In this case, the pump conversion efficiency is equally low as that of the multimode regime.

Since the pump intensity, in this case, is quite comparable to that of the control intensity, the XPM between the two strong beams becomes non-negligible. Hence, the present model can't explain the generation of these spatial modes, which are speculated to be the result of a complex potential experienced by the generated fields. However, the simultaneous observation of these modes is further confirmation of the spatial correlation between the generated beams.

4.5 Conclusion

In this chapter, we have presented the study of all-optically guided MOPO which is found to be the result of ground-state coherence assisted efficient nonlinear processes. We report the excitation of spatially correlated modes in both the generated fields with a pump conversion efficiency of more than 30%. The maximum Stokes power could rise to ~ 1 mW with suitable experimental parameters. We show that the generation of the higher-order Laguerre-Gaussian modes is a consequence of optically induced waveguides unlike for the cases of FWM inside a fiber [41, 42] or FWM with input beams containing orbital angular momentum [43, 44]. We present a theory based on the propagation of fields in the nonlinear medium and a semiclassical model of the four-level system for the calculation of nonlinearity in the medium. However, our model does not include depletion of the input strong fields and hence is unable to explain the generation of higher-order modes in the generated fields.

Bibliography

- [1] S. E. Harris, *Appl. Phys. Letts.* **9**, 114 (1966).
- [2] C. Canalias and V. S. Pasiskeviciu, *Nat. Photonics* **1**, 459 (2007).
- [3] G. Strömqvist, V. Pasiskevicius, C. Canalias, and C. Montes, *Phy. Rev. A* **84**, 023825 (2011).
- [4] G. Strömqvist, V. Pasiskevicius, C. Canalias, P. Aschieri, A. Picozzi, and C. Montes, *J. Opt. Soc. Am. B* **29**, 1194-1202 (2012).
- [5] C. Liljestränd, A. Zukauskas, V. Pasiskevicius, and C. Canalias, *Opt. Lett.* **32**, 2435-2438 (2017).
- [6] D. A. Braje, V. Balić, S. Goda, G. Y. Yin, and S. E. Harris, *Phy. Rev. Lett.* **93**, 183601 (2004).
- [7] S. Du, J. Wen, and M. H. Rubin, *J. Opt. Soc. Am. B* **25**, C98–C108 (2008).
- [8] S. Du, P. Kolchin, C. Belthangady, G. Y. Yin, and S. E. Harris. *Phy. Rev. Lett.* **100**, 183603 (2008).
- [9] V. Balić, D. A. Braje, P. Kolchin, G. Y. Yin, and S. E. Harris, *Phy. Rev. Lett.* **94**, 183601 (2005).
- [10] P. Kolchin, *Phy. Rev. A* **75**, 033814 (2007).
- [11] Y. Mei, X. Guo, L. Zhao, and S. Du, *Phy. Rev. Lett.* **119**, 150406 (2017).
- [12] Y. Silberberg, and I. B. Joseph, *Phy. Rev. Lett.* **48**, 1541-1543 (1982).
- [13] M. Pinard, D. Grandclement, and G. Grynberg, *Europhys. Lett.* **2**, 755-760 (1986).

- [14] A. L. Gaeta, R. W. Boyd, J. R. Ackerhalt, and P. W. Milonni, *Phy. Rev. Lett.* **58**, 2432-2435 (1987).
- [15] G. Khitrova, J. F. Valley, and H. M. Gibbs, *Phy. Rev. Lett.* **60**, 1126-1129 (1988).
- [16] A. S. Zibrov, M. D. Lukin, and M. O. Scully, *Phy. Rev. Lett.* **83**, 4049-4052 (1999).
- [17] M. D. Lukin, P. R. Hemmer, M. Löffler, and M. O. Scully, *Phy. Rev. Lett.* **81**, 2675-2678 (1998).
- [18] M. Fleischhauer, M. D. Lukin, A. B. Matsko, and M. O. Scully, *Phy. Rev. Lett.* **84**, 3558-3561 (2000).
- [19] M. D. Lukin, A. B. Matsko, M. Fleischhauer, and M. O. Scully, *Phy. Rev. Lett.* **82**, 1847-1850 (1999).
- [20] Wei Jiang, Chao Han, Peng Xue, L.-M. Duan, and G.-C. Guo, *Phy. Rev. A* **69**, 043819 (2004).
- [21] C. H. R. Ooi, Q. Sun, M. S. Zubairy, and M. O. Scully, *Phy. Rev. A* **75**, 013820 (2007).
- [22] K. Zhang, J. Guo, C.-H. Yuan, L. Q. Chen, C. Bian, B. Chen, Z. Y. Ou, and W. Zhang, *Phy. Rev. A* **89**, 063826 (2014).
- [23] G. P. Agrawal, *Phy. Rev. Lett.* **64**, 2487-2490 (1990).
- [24] R. De La Fuente, A. Barthelemy, and C. Froehly, *Eurpphy. Lett.* **16**, 793-795 (1991).
- [25] G. A. Swartzlander, Jr. and C. T. Law, *Phy. Rev. Lett.* **69**, 2503-2506 (1992).
- [26] J. Cheng, S. Han, and Y. Yan, *Phy. Rev. A* **72**, 021801 (2005).
- [27] A. André, M. Bajcsy, A. S. Zibrov, and M. D. Lukin, *Phy. Rev. Lett.* **94**, 063902 (2005).
- [28] M. Vengalattore and M. Prentiss, *Phy. Rev. Lett.* **95**, 063902 (2005).
- [29] R. R. Moseley, S. Shepherd, D. J. Fulton, B. D. Sinclair, and M. H. Dunn, *Phy. Rev. A* **53**, 408-415 (1996).
- [30] R. Kapoor and G. S. Agarwal, *Phy. Rev. A* **61**, 053818 (2000).

- [31] H. Shpaisman, A. D. Wilson-Gordon, and H. Friedmann, *Phy. Rev. A* **71**, 043812 (2005).
- [32] J. A. Andersen, M. E. J. Friese, A. G. Truscott, Z. Ficek, P. D. Drummond, N. R. Heckenberg, and H. Rubinsztein-Dunlop, *Phy. Rev. A* **63**, 023820 (2001).
- [33] A. G. Truscott, M. E. J. Friese, N. R. Heckenberg, and H. Rubinsztein-Dunlop, *Phy. Rev. Lett.* **82**, 063902 (1999).
- [34] P. K. Vudyasetu, D. J. Starling, and J. C. Howell, *Phy. Rev. Lett.* **102**, 123602 (2009).
- [35] S. S. Sahoo, A. Bhowmick and A. K. Mohapatra, *J. Phys. B: At. Mol. Opt. Phys* **50**, 055501 (2017).
- [36] M. G. Bason, A. K. Mohapatra, K. J. Weatherill and C. S. Adams, *J. Phys. B: At. Mol. Opt. Phys* **42**, 075503 (2009).
- [37] K. Islam et al., *J. Phys. B: At. Mol. Opt. Phys* **50**, 215401 (2017).
- [38] O. N. Verma and T. N. Dey, *Phys. Rev. A* **91**, 013820 (2015).
- [39] S. Alperin, R. Niederriter, J. Gopinath, and M. Siemens, *Opt. Lett.* **41**, 5019-5022 (2016).
- [40] V. Denisenko, V. Shvedov, A. S. Desyatnikov, D. N. Neshev, W. Krolikowski, A. Volyar, M. Soskin, and Y. S. Kivshar, *Opt. Express* **17**, 23374 (2009).
- [41] D. A. Akimov, E. E. Serebryannikov, A. M. Zheltikov, M. Schmitt, R. Maksimenka, W. Kiefer, K. V. Dukelskii, V. S. Shevandin, and Yu. N. Kondratev, *Opt. Lett.* **28**, 1948 (2003).
- [42] Omer Tzang, Antonio M. Caravaca-Aguirre, Kelvin Wagner and Rafael Piestun, *Nat. Phot.* **12**, 368 (2018).
- [43] S. Barreiro and J.W. R. Tabosa, *Phys. Rev. Lett.* **90**, 133001 (2003).
- [44] G. Walker, A. S. Arnold, and S. Franke-Arnold, *Phy. Rev. Lett.* **108**, 243601 (2012).

Chapter 5

MOPO-based optical bistability

Optical bistability refers to the existence of two different stable transmission states of a system under the same input condition and it is possible when the system has a memory effect. The phenomenon was first proposed by Szoke *et al.* [1] and experimentally observed by Gibbs *et al.* [2] in the transmission of Fabry-Perot interferometer containing sodium vapor. Typically, a bistable device consists of a nonlinear medium placed inside a resonator to provide optical feedback to the system [3]. Substantial work on bistability using a two-level and three-level atomic system inside a cavity has been reported [4–8]. However, there are instances of optical bistability in systems without requiring a resonator such as; bistability using degenerate four-wave mixing [9], intrinsic atom-light coupling [10], polarisation bistability in sodium vapor [11], resonator-less bistability with single mirror feedback [12], dynamic bistability in the Raman generation [13] or bistability as a result of co-operative inter-atomic interaction with Rydberg atoms [14]. It has potential applications in all-optical switching [15–17] and hence is very important for signal processing.

For the case of MOPO in thermal vapor, we observe that the generated beam power shows a bistable behavior with the input pump or control power variation. This is also an instance of bistability in a nonlinear medium without the need for external feedback. In this chapter, we discuss the experimental setup and observation of MOPO-based all-optical bistability. We also discuss the possible theoretical explanation for the observed bistability. The dependence of the phenomenon on different experimental parameters is presented. The possibility of a phase transition at the threshold is studied by investigating critical slowing down in the switch-on time of the generated beams.

5.1 Principle of MOPO-based optical bistability

The system under consideration is a double- Λ system as shown in Fig. 5.1. The MOPO-based bistability can be understood by considering the coupled equations for the propagation of the Stokes and the anti-Stokes beams inside the medium. First, we find out the threshold condition by considering plane wave approximation and then the Gaussian nature of the beams is introduced to explain the existence of two different thresholds.

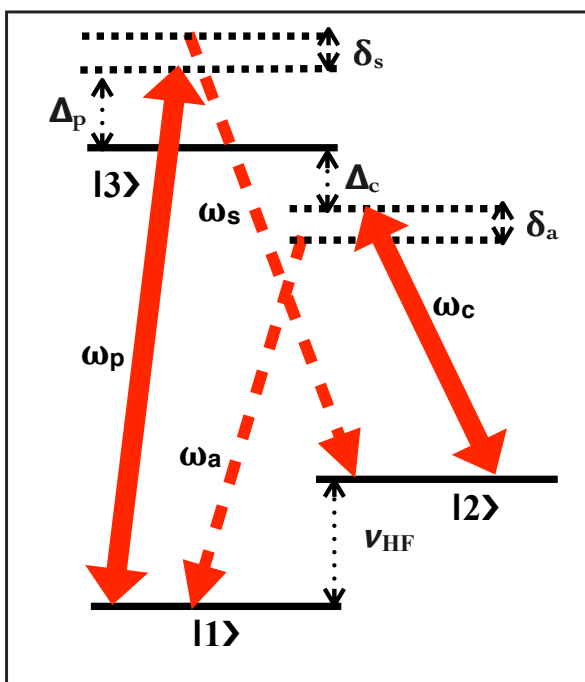


Figure 5.1: Schematic of energy level diagram for MOPO process.

5.1.1 Threshold condition for MOPO using plane-wave approximation

Neglecting the contribution of XPM, the coupled equations for the Stokes and anti-Stokes beams under phase-matched condition in plane-wave approximation read as,

$$\frac{dA_s}{dz} = i\kappa'_s A_p A_c A_a^*, \quad (5.1)$$

$$-\frac{dA_a}{dz} = i\kappa'_a A_p A_c A_s^*. \quad (5.2)$$

Where $\kappa'_{s,a} = \frac{3}{2}k_{s,a}\chi_{\text{FWM}}^{(3)}$. The phases of all the four interacting fields are related by, $\phi_p + \phi_c = \phi_s + \phi_a$ where ϕ_i , $i = p, c, s, a$ are the phases of the pump, control, Stokes and the anti-Stokes beams respectively. Since the pump and the control beams are derived from two different

lasers, we can choose their phases to be zero. This leads to $\phi_s + \phi_a = 0$, which is satisfied by considering $\phi_s = \phi_a = 0$. Therefore, we can consider all the field amplitudes to be real. Writing the equations in terms of the corresponding Rabi frequencies,

$$\frac{d\Omega_s}{dz} = \kappa\Omega_p\Omega_a, \quad (5.3)$$

$$-\frac{d\Omega_a}{dz} = \kappa\Omega_p\Omega_s. \quad (5.4)$$

Here $\kappa = i\frac{3}{2}k(\frac{\hbar}{2\mu})^2\chi_{\text{FWM}}^{(3)}\Omega_c$ and Ω_i , $i = p, c, s, a$ are the Rabi frequencies of the pump, control, Stokes and anti-Stokes beams respectively. For the experimental parameters used in our experiment, the conversion of control to anti-Stokes fields is negligibly small. Therefore, the control beam is considered to be undepleted. However, the pump conversion efficiency is very high i.e. $\sim 30\%$ and hence the pump depletion can not be neglected. We take the depletion of pump beam into account by considering, $\Omega_p^2 + \Omega_s^2 = \Omega_p^2(z = 0) = \Omega_i^2$ and $\Omega_s^2 + \Omega_a^2 = \Omega_s^2(z = l) = \Omega_a^2(z = 0) = \Omega_0^2$. Since Ω_0 and Ω_i are constants with z , these conditions upon differentiation lead to the relation,

$$\Omega_p \frac{d\Omega_p}{dz} = \Omega_a \frac{d\Omega_a}{dz} = -\Omega_s \frac{d\Omega_s}{dz} \quad (5.5)$$

Differentiating equation 5.3 w.r.t z , we get,

$$\frac{d^2\Omega_s}{dz^2} = \kappa\left[\frac{d\Omega_p}{dz}\Omega_a + \frac{d\Omega_a}{dz}\Omega_p\right]. \quad (5.6)$$

Substituting the value of $\frac{d\Omega_p}{dz} = \frac{\Omega_a}{\Omega_p} \frac{d\Omega_a}{dz}$ from equation 5.5 in equation 5.6, we get

$$\frac{d^2\Omega_s}{dz^2} = \kappa\left[\frac{\Omega_a^2}{\Omega_p} + \Omega_p\right]\frac{d\Omega_a}{dz}. \quad (5.7)$$

Now using equation 5.4, the equation 5.7 can be written as,

$$\frac{d^2\Omega_s}{dz^2} = -\kappa^2[\Omega_a^2 + \Omega_p^2]\Omega_s. \quad (5.8)$$

Replacing $\Omega_a^2 = \Omega_0^2 - \Omega_s^2$ and $\Omega_p^2 = \Omega_i^2 - \Omega_s^2$ in equation 5.8, the equation boils down to,

$$\frac{d^2\Omega_s}{dz^2} + 2\kappa^2(\Omega_i^2 + \Omega_0^2)\Omega_s - 2\kappa^2\Omega_s^3 = 0. \quad (5.9)$$

With a change of variables, $\Omega_s \rightarrow x$, $2\kappa^2(\Omega_i^2 + \Omega_0^2) \rightarrow \gamma$, $2\kappa^2 \rightarrow \beta$ and $z \rightarrow t$, equation 5.9 can be rewritten as,

$$\frac{d^2x}{dt^2} + \gamma x - \beta x^3 = 0, \quad (5.10)$$

which resembles the equation of motion of a classical particle in a potential given by, $V(x) = \frac{1}{2}\gamma x^2 - \frac{\beta}{4}x^3$. If t_0 is the time taken by the particle to reach the position x_0 corresponding to the maximum value of $V(x)$, then by Newtonian mechanics, t_0 can be evaluated by,

$$t_0 = \int_0^{x_0} \frac{dx}{\sqrt{2(V(x_0) - V(x))}} \quad (5.11)$$

The potential for the actual system is given as, $V(\Omega_s) = \frac{1}{2}\kappa(\Omega_i^2 + \Omega_0^2)\Omega_s^2 - \frac{1}{2}\kappa^2\Omega_s^4$, with the length of the cell (l) being related to Ω_0 by,

$$l = \int_0^{\Omega_0} \frac{d\Omega_s}{\sqrt{2(V(\Omega_0) - V(\Omega_s))}}, \quad (5.12)$$

which can be solved to get the solution as,

$$\kappa l \Omega_i = \text{EllipticK}(\eta). \quad (5.13)$$

Here, η stands for the pump conversion efficiency given as, $\eta = \frac{\Omega_0^2}{\Omega_i^2}$ and the elliptic function is defined as,

$$\text{EllipticK}(\eta) = \frac{\pi}{2} + \frac{\pi}{8}\eta + \frac{9\pi}{128}\eta^2 + \frac{25\pi}{512}\eta^3 + O(4) + \dots \quad (5.14)$$

The value of η can be solved for the given Ω_i , κ_0 and l as shown in Fig. 5.2. At the threshold, $\eta \rightarrow 0$, which leads to the condition,

$$\kappa l \Omega_i = \frac{\pi}{2}, \quad (5.15)$$

which is the same threshold condition found in the references [18, 19].

5.1.2 Effect of Gaussian nature of the beams

The density matrix equations of the four-levels (refer to equations 4.2-4.11) can be solved to find the expression of $\chi_{\text{FWM}}^{(3)}$ as a function of the atomic coherence, ρ_{12} . The propagation equations 5.3 and 5.4 can thus be alternatively expressed as,

$$\frac{d\Omega_s}{dz} = -3ik \left(\frac{N\mu^2}{\epsilon_0\hbar} \right) \frac{\Omega_p}{2\Delta_p} \rho_{12}^{(ca)}, \quad (5.16)$$

$$\frac{d\Omega_a}{dz} = -3ik \left(\frac{N\mu^2}{\epsilon_0\hbar} \right) \frac{\Omega_c}{2\Delta_c} \rho_{21}^{(ps)}, \quad (5.17)$$

where $\rho_{12}^{(ca)}$ and $\rho_{21}^{(ps)}$ are given by the expressions,

$$\rho_{12}^{(ca)} = \frac{\frac{\Omega_c\Omega_a}{(4\Delta_c)}}{\Delta_{eff} + i\gamma_c}, \quad (5.18)$$

$$\rho_{21}^{(ps)} = \frac{\frac{\Omega_p\Omega_s}{(4\Delta_p)}}{\Delta_{eff} - i\gamma_c}. \quad (5.19)$$

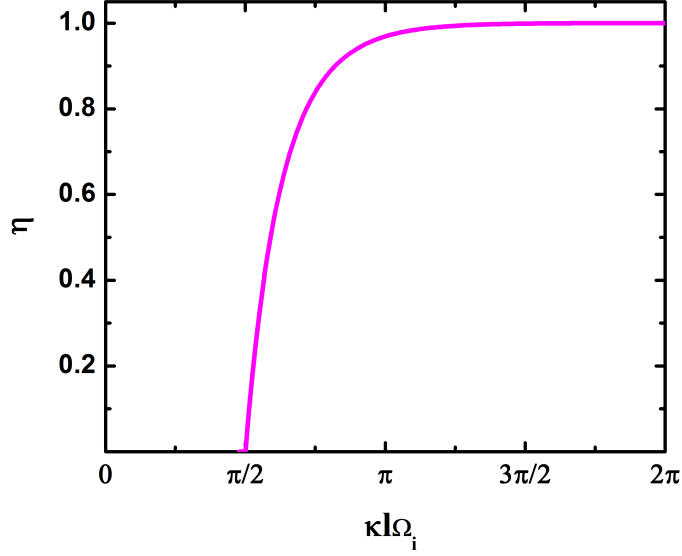


Figure 5.2: Variation of the pump conversion efficiency (η) with different values of $\kappa_0\Omega_i l$.

Here, Δ_p and Δ_c are the single-photon detunings for the pump and the control beams as shown in Fig 5.1 whereas $\Delta = \Delta_s - \Delta_p = \Delta_a - \Delta_c$ and $\Delta_{eff} = \Delta - \frac{\Omega_p^2}{4\Delta_p} + \frac{\Omega_s^2}{4\Delta_p} + \frac{\Omega_c^2}{4\Delta_c} - \frac{\Omega_a^2}{4\Delta_c}$. We consider the generation with effective detuning, $\Delta_{eff} = 0$. Now, the dephasing rate associated with the coherence time of the system can be expressed as,

$$\gamma_c = \frac{v_{avg}}{2x}, \quad (5.20)$$

where v_{avg} is the average velocity of the atoms in the thermal vapor and x is the size of the beam in the transverse direction. Hence, the atomic coherence depends on the sizes of the interacting fields as,

$$\rho_{12}^{(ca)} = -i \frac{x}{v_{avg}} \frac{\Omega_c \Omega_a}{(2\Delta_c)}, \quad \rho_{21}^{(ps)} = i \frac{x}{v_{avg}} \frac{\Omega_p \Omega_s}{(2\Delta_p)}. \quad (5.21)$$

The threshold condition can now be rewritten by considering the x dependence as,

$$\kappa_0 \Omega_i x = \frac{\pi}{2} \quad (5.22)$$

Here $\kappa_0 = \frac{\kappa l}{x} = -\frac{3}{4} k \left(\frac{N \mu^2 l}{\epsilon_0 \hbar v_{avg}} \right) \frac{\Omega_c}{\Delta_p \Delta_c}$. In plane-wave approximation, the size of the generated Stokes beam is same as the size of the pump beam. However, for the case of Gaussian beam with, $\Omega_i = \Omega_m e^{-\frac{x^2}{2w_0^2}}$, the radius of MOPO generation is determined by the value of x for which Ω_i satisfies the threshold condition (equation 5.22) as illustrated in Fig 5.3. This leads to the optimization between the input threshold and the coherence induced in the medium. Now, with

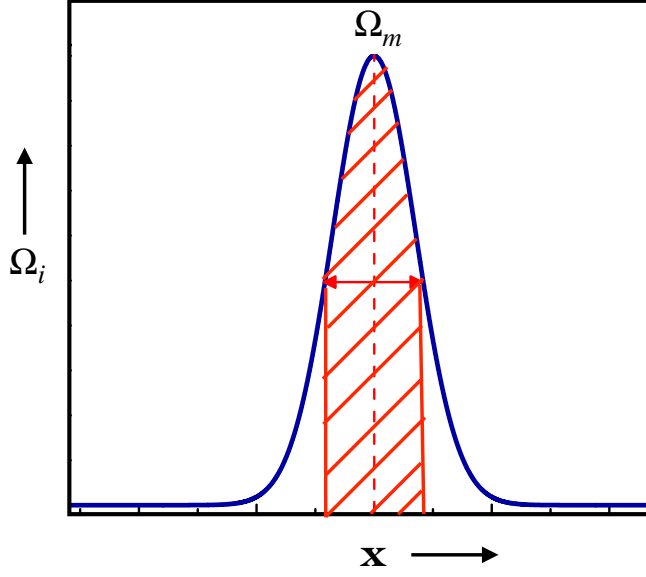


Figure 5.3: Gaussian nature of the Rabi-frequency with peak value Ω_m with the radius of MOPO generation being highlighted.

the Gaussian nature of the beam, the threshold condition is modified as,

$$x e^{-\frac{x^2}{2w_0^2}} = \frac{\pi}{2\kappa_0} \left(\frac{1}{\Omega_m} \right) \quad (5.23)$$

Since the L.H.S. of equation 5.23 has a peak functional form, the solution for minimum Ω_m satisfying the threshold condition is found by finding the maximum value of the L.H.S using $\frac{d}{dx} [x e^{-\frac{x^2}{2w_0^2}}] = 0$, which is satisfied for $x = \pm w_0$. It leads to the peak forward threshold Rabi frequency (Ω_F^T) satisfying,

$$\kappa_0 \Omega_F^T \frac{w_0}{\sqrt{e}} = \frac{\pi}{2}. \quad (5.24)$$

In this case, Ω_F^T satisfying the above condition is much larger than Ω_i for the case of plane-waves as given by equation 5.22 leading to a huge generation of light at the center of the beam. Comparing equation 5.24 and 5.22, the forward threshold for a Gaussian beam is \sqrt{e} times larger than the threshold for a plane wave with a beam size of w_0 . Now, the backward threshold is a consequence of the long-lived ground state atomic coherence present in the system, which stays even if the pump power is decreased to a value lower than the initial forward threshold. This finite atomic coherence in the backward direction is determined by the size of the Stokes beam. When the pump peak power is reduced to a value such that the size of the Stokes beam is insufficient to sustain the coherence throughout the medium, then the Stokes power falls to

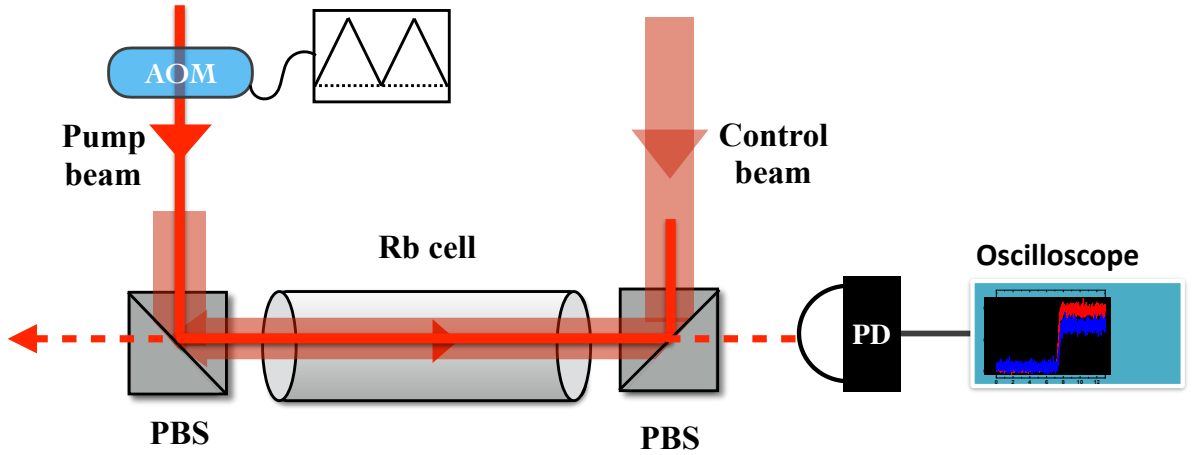


Figure 5.4: Schematic of experimental setup for the observation of MOPO-based optical bistability. PBS: Polarising beam splitter, PD: Photodetector.

zero resulting in the backward threshold. So, the backward threshold can be determined from 5.22 by replacing x with Stokes beam waist w_s ,

$$\kappa_0 \Omega_B^T w_s = \frac{\pi}{2} \quad (5.25)$$

These two different thresholds lead to the observed bistability in the system.

5.2 Experimental arrangement

The experiment is performed with rubidium vapor in the regime of MOPO with a double- Λ system as shown in Fig. 5.1. The experimental parameters i.e. the laser frequencies and powers of the input pump and control beams are optimized to get the generated Stokes and anti-Stokes beams in the lowest order mode of MOPO (refer to section 4.2 of chapter 4). To experimentally study the MOPO-based optical bistability, the experimental setup is slightly modified as shown in Fig. 5.4. In this case, the control power is fixed at the threshold value and an acousto-optic modulator (AOM) is used in the path of the pump beam to modulate its power with a ramp function. Hence, the pump power increases linearly from zero to a certain finite power, which is more than the threshold power of the MOPO generation and again decreases linearly to zero. In this way, the pump threshold in both increasing, as well as decreasing pump power direction, can be studied. The generated Stokes power is detected using a photodetector and is analyzed in an oscilloscope.

5.3 Experimental observation of the optical bistability

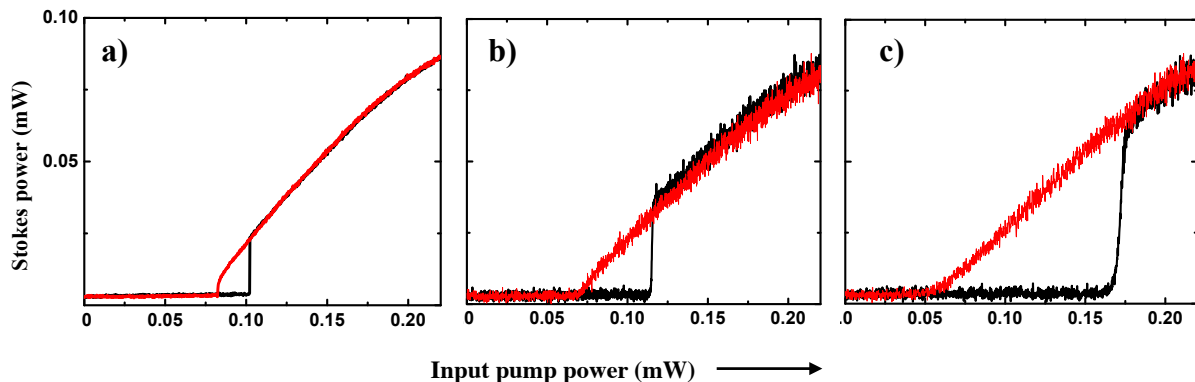


Figure 5.5: Variation of bistability width with modulation frequency for a) 50 Hz, b) 5 kHz and c) 50 kHz. The black line refers to forward direction and the red line refers to the backward direction of the pump power variation.

Under the experimental conditions of MOPO, we observe that the pump threshold value for MOPO in the increasing pump power direction is different from the value in the decreasing pump power direction. In the single-mode regime of MOPO, the Stokes power is observed to vary linearly with the input pump power in both increasing (forward) and decreasing (backward) direction of pump power variation. Similar bistable behavior is observed in the Stokes power as well in the anti-stokes power when the pump power is fixed and the control power is modulated.

We investigate the bistability width and the threshold values with different experimental parameters. To study the dynamical behavior of the optical bistability [13, 20] observed in our system, the frequency for pump intensity modulation is varied and its effect on bistability is studied. We find that the observed pump threshold values and hence the bistability width is found to depend on the modulation frequency (f_m). We present the experimental data for different modulation frequencies in Fig. 5.5. The width of the bistability is found to increase with the increase in the modulation frequency. This behavior is similar to the case of Raman generation, where the origin of bistability is the generalized four-photon dark state [13]. The forward threshold (P_F) and the backward threshold (P_B) in this case are expected to vary as the square root of the modulation frequency by the relation, $P_{F,B} \simeq P_{th}(1 \pm \frac{1}{2}\sqrt{f_m\tau})$, where P_{th} is the threshold power for CW regime and τ is the four-photon dark state equilibrium time [13]. The experimental data for both P_F and P_B with different modulation frequencies

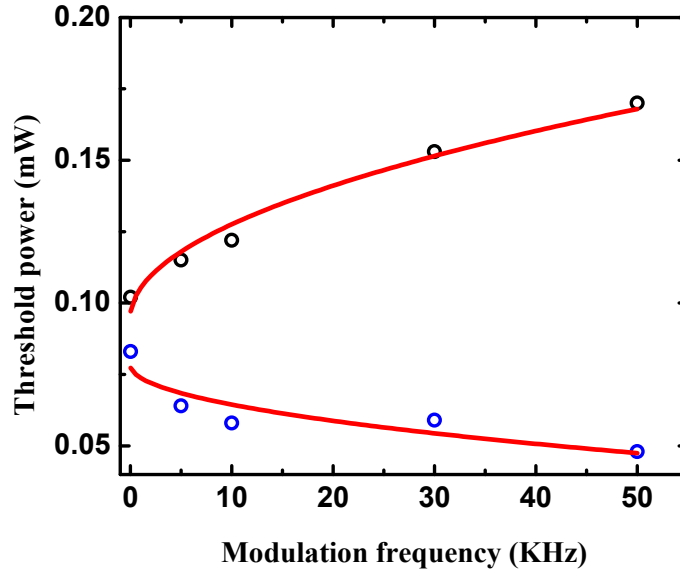


Figure 5.6: Variation of the forward threshold (black circles) and backward threshold (blue circles) as a function of the width with modulation frequency. The solid red line refers to the theoretical fitting.

are presented as the black and blue circles in Fig. 5.6 respectively. The data are indeed found to vary as the square root of f_m as shown by the red solid line in Fig. 5.6. However, in our case, the bistability width is found to be constant below a certain minimum value of the modulation frequency, which is 50 Hz for the given experimental parameters. This suggests that the system has steady-state bistability in addition to the dynamic bistability. Hence, for further experimental investigation, the value of f_m is always kept to be 50 Hz or less.

The matching of the experimental data and the theoretical model is presented in Fig 5.7(a). We also investigate the variation of the forward threshold Rabi frequency with the beam waist of the pump beam. It shows a $\frac{1}{w_0}$ dependence as shown in Fig 5.7(b) satisfying theoretical model (refer to equation 5.24).

We also vary the density of the vapor and investigate its effect on bistable behavior. It is observed that the forward threshold decreases with increasing density of the vapor cell and is minimum for the density corresponding to the cell temperature of 120⁰ C.

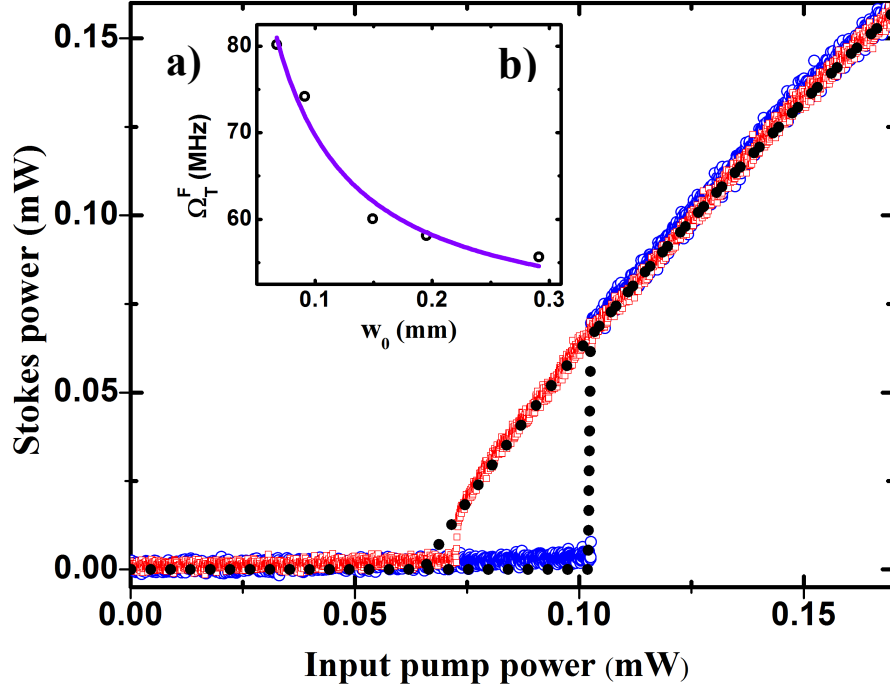


Figure 5.7: a) Variation of Stokes power with input pump power. The blue open circles (red squares) shows experimentally measured variation in the increasing (decreasing) pump power direction and the black points show the theoretical fitting. b) Variation of the forward threshold Rabi frequency with the pump beam waist (w_0).

5.4 Experimental verification of the role of coherence in the optical bistability

To verify the effect of atomic coherence in the system, we perform an experiment by modulating the input pump power following a functional form as shown in the red line of Fig. 5.8. We use two different AOMs, which are modulated with pulses of different widths to derive the desired modulation. As illustrated in Fig. 5.8, the level A refers to the pump power beyond the forward threshold such that level B falls within the bistable region. Then the pump power is switched to zero (level C) for a period of Δt before switching back to power B and A .

The experimental data is shown in Fig 5.9 (a) and (b), where the red line corresponds to the input pump power and the blue line corresponds to the generated Stokes power. We have used Δt to be $\sim 1\mu s$. Initially, the Stokes power is nearly 30% of the pump power at the level A and B as expected. As the pump power is switched to zero in the bistable region (to level C), then the Stokes power goes zero. Now as the pump power is switched back to the level B , which is less than the forward threshold, the Stokes power is not expected to rise. However, we observe

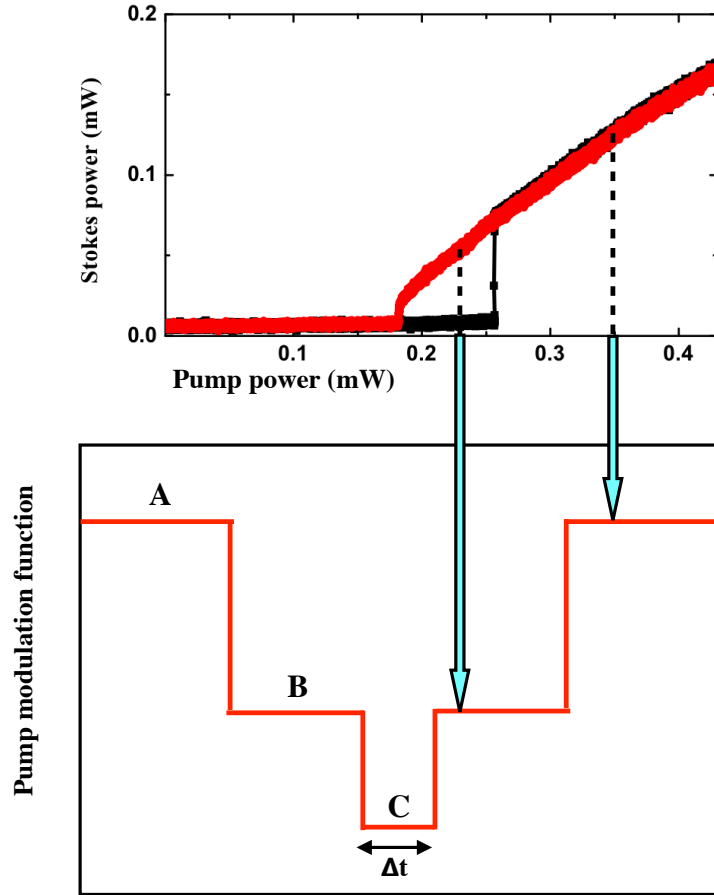


Figure 5.8: Illustration of the pump modulation function.

that the Stokes power switches back to a finite value as shown in the blue line of Fig. 5.9 (a). The Stokes power, in this case, is switched on after a time of $\sim 4\mu\text{s}$ as depicted in Fig. 5.9 (b). This switching back of Stokes power is certainly because of the finite hyperfine coherence in the bistable regime.

To further verify the role of atomic coherence, we conduct another experiment in the same setup. We use the fact that the atomic coherence is limited by the transit time of the atoms through the laser beams. So, we vary the beam waists of the pump beam and measure the coherence time in the bistable region. The coherence time, in this case, is the maximum value of Δt , for which the Stokes beam is switched back to a finite value. The corresponding experimental data is presented in Fig. 5.10, where the coherence time is found to vary linearly with the beam waist.

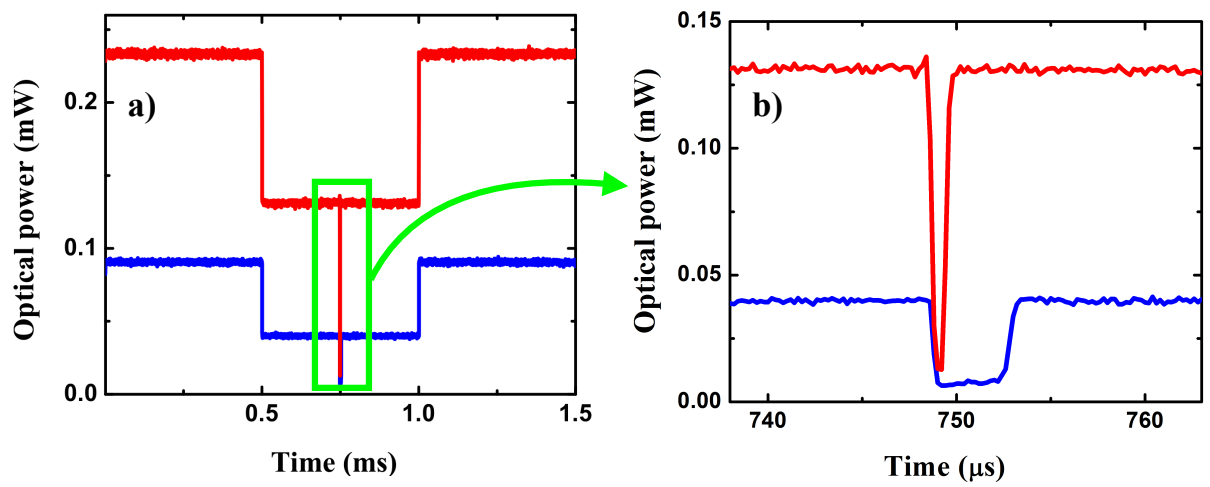


Figure 5.9: Experimental evidence of atomic coherence based bistability. The Red line shows the input pump power variation and the blue line shows the generated Stokes power variation. Highlighted area of a) is expanded and presented in b).

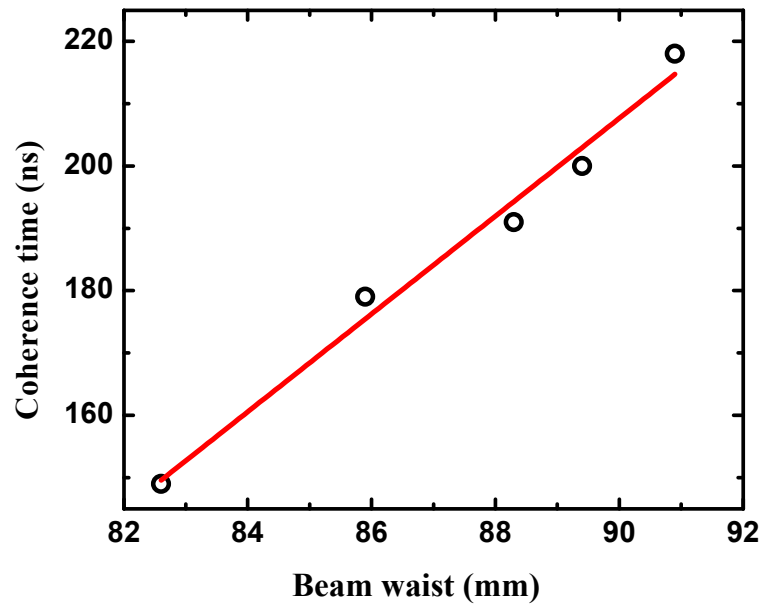


Figure 5.10: Coherence time measured with different beam waists of pump beam. The black circles are experimental data and the red line shows the linear fitting.

5.5 Study of switch-on time of Stokes generation

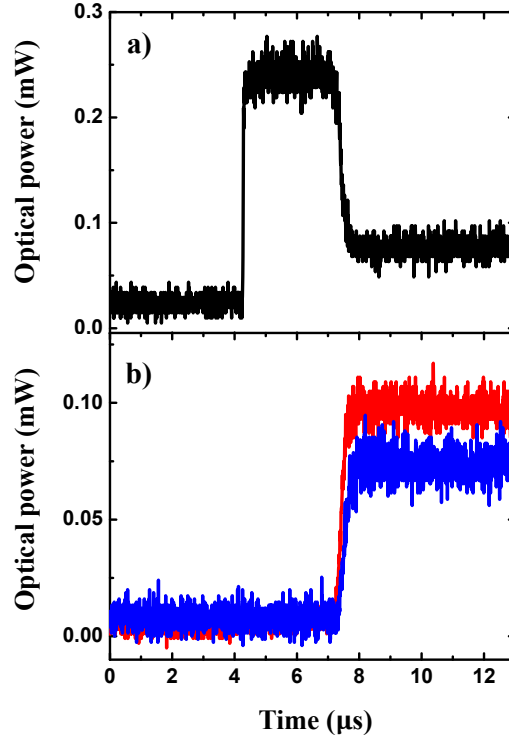


Figure 5.11: a) Output pump power, b) Stokes power (red line) and anti-Stokes power (blue line) in response to a pulsed input pump.

As is well known, the observation of bistability is a characteristic feature of the first-order phase transition [21, 22]. For our case, the experimental observation of a discontinuity in the generated field at the threshold and the bistable behavior implies the presence of a first-order phase transition, where the generated field acts as the order parameter.

We observe that when the input pump power is switched on from zero to a finite value that is more than the forward threshold power, the Stokes beam is generated with a time delay called the switch-on time as shown in Fig. 5.11. The minimum value of switch-on time is found to be of the order of $0.8 - 1 \mu\text{s}$.

As the pump power approaches the threshold value, the switch-on time of Stokes generation diverges (critical slowing down) as shown in Fig. 5.12(a). It is a quantity similar to the order parameter susceptibility for the case of first order phase transition. The experimental data is fitted with a function of the form, $y = A(P - P_T)^c$, where the values of the threshold power (P_T) and the critical exponent (c) are evaluated from the fitting. For a system with dispersive

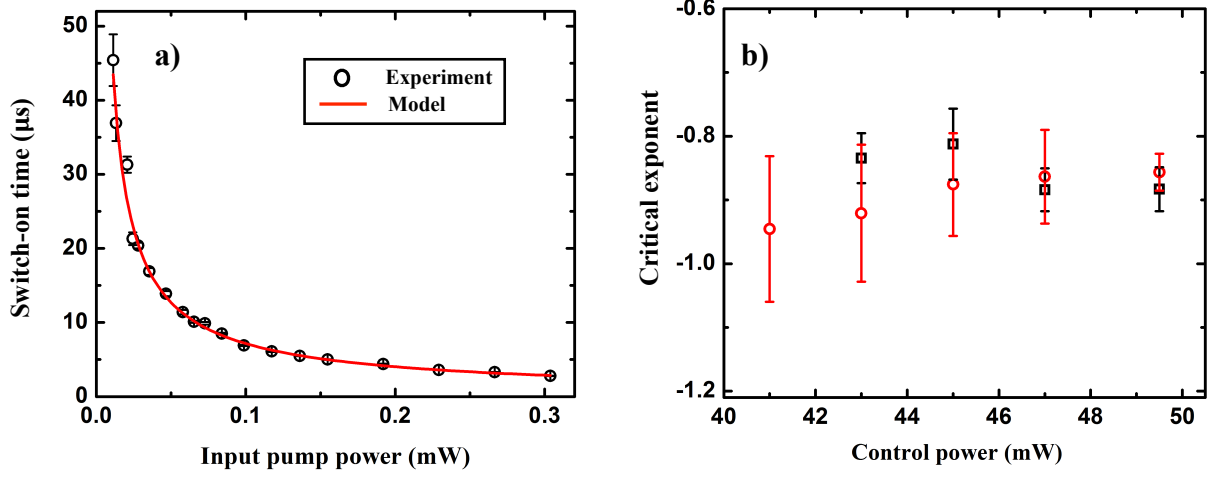


Figure 5.12: a) Variation of switch-on time of Stokes beam generation with input pump power. b) Critical exponent measured with different control powers and different densities of the vapor cell. The red circles (black squares) represent the data corresponding to vapor density of $6 \times 10^{12} \text{ cm}^{-3}$ (10^{13} cm^{-3}).

optical bistability [23], the value of critical exponent (c) is found to be -0.5 . However, for our case, the value of c is found to be around -0.854 ± 0.015 , evaluated for different control powers as well as different densities of the vapor as shown in Fig. 5.12(b).

5.6 Conclusion

We experimentally observe and verify the atomic coherence based optical bistability observed in the threshold of MOPO. We measure the critical exponent associated with the forward threshold, which is found to be different from similar bistable systems. Hence, our system exhibits conventionally different bistability and it is possibly related to interesting effects like self-organized bistability [24] and self-organized criticality (SOC) [25, 26].

Bibliography

- [1] A. Szoke, V. Daneu, J. Goldhar, and N. A. Kurnit, *Appl. Phys. Lett.* **15**, 376 (1969).
- [2] H. M. Gibbs, S. L. McCall, and T. N. C. Venkatesan, *Phys. Rev. Lett.* **36**, 1135 (1976).
- [3] H. M. Gibbs, *Optical Bistability: Controlling Light with Light* (Academic Press, New York, (1985).
- [4] S. Cecchi, G. Giusfredi, E. Petriella, and P. Salieri, *Phys. Rev. Lett.* **49**, 1928 (1982).
- [5] L.A. Orozco, A.T. Rosenberger, and H.J. Kimble, *Phys. Rev. Lett.* **53**, 2547 (1984).
- [6] W. Harshawardhan and G. S. Agarwal *Phys. Rev. A* **53**, 1812 (1996).
- [7] H. Wang, D. J. Goorskey, and M. Xiao, *Phys. Rev. A* **65**, 011801(R) (2001).
- [8] A. Joshi and M. Xiao, *Phys. Rev. Lett.* **91**, 143904 (2003).
- [9] H. G. Winful and J. H. Marburger, *Appl. Phys. Lett.* **36**, 613 (1980).
- [10] D. A. B. Miller, A. C. Gossard, and W. Wiegmann, *Opt. Lett.* **9**, 162 (1981).
- [11] Daniel J. Gauthier, Michelle S. Malcuit, Alexander L. Gaeta, and Robert W. Boyd, *Phys. Rev. Lett.* **64**, 1721 (1990).
- [12] T. Ackemann, A. Heuer, Yu. A. Logvin, and W. Lange, *Phys. Rev. A* **56**, 2321 (1997).
- [13] I. Novikova, A. S. Zibrov, D. F. Phillips, A. Andre, and R. L. Walsworth, *Phys. Rev. A* **69**, 061802(R) (2004).
- [14] N. R. de Melo, C. G. Wade, N. Sibalic, J. M. Kondo, C. S. Adams, and K. J. Weatherill, *Phys. Rev. A* **93**, 063863 (2016).
- [15] H. Wang, D. Goorskey, and M. Xiao, *Phys. Rev. A* **65**, 051802(R) (2002).

- [16] Hong Chang, Haibin Wu, Changde Xie, and Hai Wang, *Phys. Rev. Lett.* **93**, 213901 (2004).
- [17] J. Sheng, U. Khadka, and M. Xiao, *Phys. Rev. Lett.* **109**, 223906 (2012).
- [18] D. A. Braje, V. Balić, S. Goda, G. Y. Yin, and S. E. Harris, *Phys. Rev. Lett.* **93**, 183601 (2004).
- [19] Y. Mei, X. Guo, L. Zhao, and S. Du, *Phys. Rev. Lett.* **119**, 150406 (2017).
- [20] A. Joshi, W. Yang, and M. Xiao, *Opt. Lett.* **30**, 905 (2005).
- [21] C. M. Bowden and C. C. Sung, *Phys. Rev. A* **19**, 2392 (1979).
- [22] J. Binney, N. Dowrick, A. Fisher, and M. Newman, *The Theory of Critical Phenomena* (Oxford University Press, Oxford, 1993).
- [23] G. Grynberg and S. Cribier, *J. Physique Lett.* **44**, 449-453 (1983).
- [24] S. di Santo, R. Burioni, A. o Vezzani, and M. A. Munoz, *Phys. Rev. Lett.* **109**, 223906 (2012).
- [25] P. Bak, C. Tang, and K. Wiesenfeld, *Phys. Rev. Lett.* **59**, 381 (1987).
- [26] P. Bak, *How Nature Works: The Science of Self-Organised Criticality* (Springer, 1999).

Chapter 6

FPGA-based photon counting module

Photon coincidence counting is the simultaneous detection of two or more photons in different detectors within a short interval of time. In quantum optics, the technique plays an essential role to study the non-classical behavior of entangled photons [1, 2]. There are different ways to implement the coincidence counting such as using time-to-amplitude converters (TACs) or using digital integrated circuits chips, but they are either huge and expensive or are not reconfigurable respectively. On the other hand, the field-programmable gate array (FPGA) technology is compact as well as reprogrammable.

An FPGA is a rewritable logic device such that it can be programmed to the desired application after manufacturing. The configuration of FPGA is usually specified using a hardware description language (HDL) like VHDL [3] and Verilog. It features highly flexible circuit design, high-speed operation and relatively low cost leading to applications such as high-performance computing, medical imaging, application-specific integrated circuit (ASIC) prototyping, scientific instruments, wired and wireless communication and many more.

This chapter includes the design of a photon counter/correlator module using the FPGA board [4]. The idea behind this work is to use this reconfigurable module to study polarisation squeezing in Zeeman degenerate two-level system (refer to chapter 3) and MOPO at a single photon level (refer to chapter 4). We describe the principle of operation of various components and present the implementation as well as the performance of the photon counting module.

6.1 Principle of operation

Here we are working on a multi-photon coincidence counting module based on FPGA (DE2-115 Altera Board). The block diagram of the coincidence module is presented in Fig. 6.1.

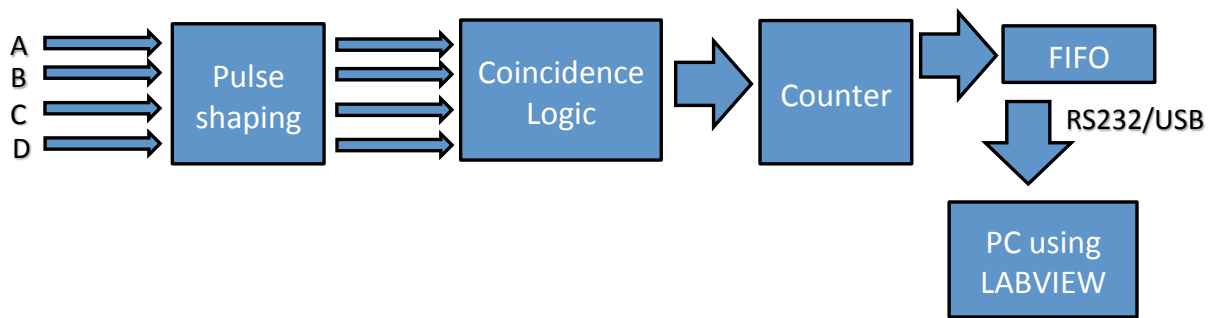


Figure 6.1: Block diagram of the multi-photon coincidence counting module

The input four channels A, B, C, and D are the output of four single-photon detectors and are connected to the FPGA board. The module can register individual channel counts as well as the two-fold, three-fold or four-fold coincidences of the channels with a coincidence window as small as 8 ns. The count data is stored in FIFO and then transferred to a computer via RS232 serial communication using the Labview software, where the data is displayed as well as is saved as a file in the computer.

6.1.1 Pulse shaping

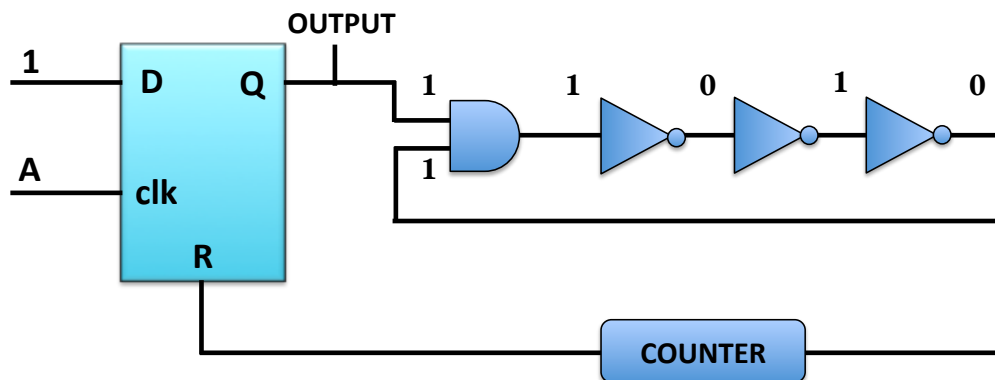


Figure 6.2: Architecture of pulse shaping

The width of the pulse-shaped signals determines the coincidence time window and hence pulse-shaping is an important component for the correlation measurement. The detailed circuit of the pulse shaping is presented in Fig. 6.2. The input from the detector is fed as a clock to a D-flipflop, where the D value always fixed at high such that whenever there is a pulse appearing in the detector signal, the output goes high. Now the output is fed to a ring counter via AND

gate. The ring counter consists of an odd number of NOT gates such that with every round, the signal level after NOT gate changes as shown in Fig. 6.2. In this way, the counter measures an increment at the rising edge of the signal with each round. After a specified counter value, the final 'OUTPUT', which is derived before the AND gate is reset to zero. The width of the 'OUTPUT' so obtained is a multiple of the time delay corresponding to a single NOT gate. In this way, we can have an output pulse of variable widths. The minimum width is achieved when the ring counter consists of a single NOT gate and the counter value is 1.

6.1.2 Coincidence Logic

The coincidence logic is implemented by using a circuit shown in Fig. 6.3. First, each of the pulse-shaped detector signals i.e. A, B, C, D is input to an OR gate, where the other input of the OR gate is connected to 0 or 5 V via a switch. Then all of them are input to an AND gate. The output will be true if and only if all the four detector signals are true i.e. if all the photons arrive at the same time, which will give a four-fold coincidence. With the help of the OR gates, we can select the individual channels as well as the 2-fold, 3-fold or 4-fold coincidences. For example, if the switch of OR gate of signal A is connected to 0 V, then the output will be sensitive to the signal pulse A. Now, if the switches of all other OR gates are high, then the output will not be sensitive to the signals B, C, D and hence, it will be a case of individual channel. Similarly, if all the switches are at 0 V, it will be a 4-fold coincidence.

6.1.3 Counting principle

After the coincidence logic, the individual and coincidence pulses are counted using different counters. We present the counting principle for the circuit in Fig. 6.4. For counting operation, we define an experimental time (T_{exp}), during which the photon pulses will be counted. T_{exp} is divided into time bins of duration T_{cycle} . The counters are active when both T_{exp} and T_{cycle} are high and the counters are reset at the falling edge of T_{cycle} , where the count values are written into a FIFO buffer. Now again the counters are active for the rising edge of the T_{cycle} . Hence the data is collected for every bin for a time period of T_{exp} .

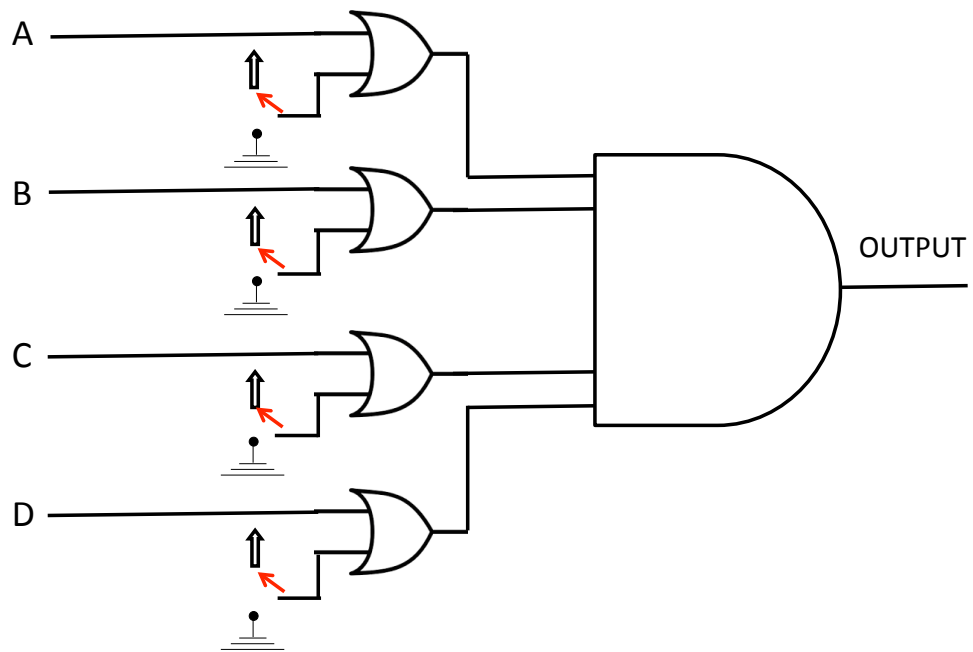


Figure 6.3: Block diagram of Coincidence logic

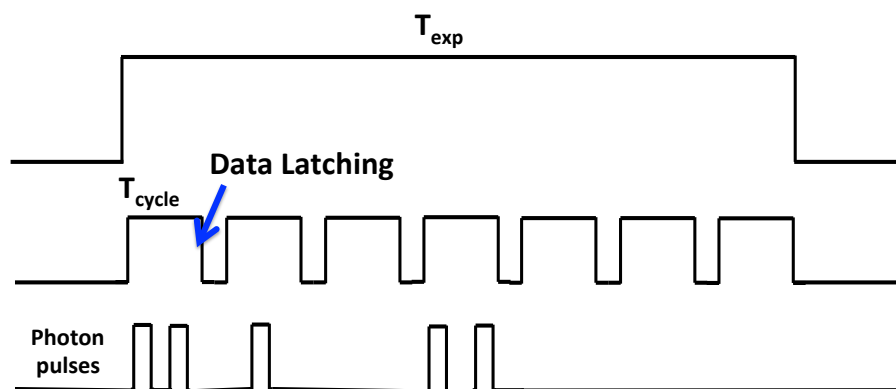


Figure 6.4: Block diagram of counting principle

6.1.4 FIFO

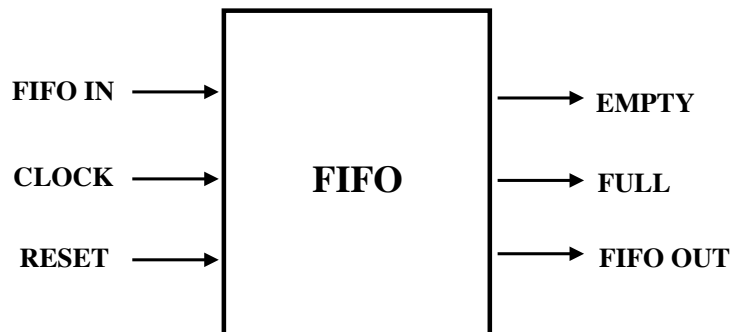


Figure 6.5: Block diagram of FIFO

FIFO stands for first-in first-out and it is used for intermediate storage or buffering. As the name suggests, the first entry to FIFO comes out first and vice versa. It consists of storage in the form of static random access memory (SRAM), flip-flops or latches. A Block diagram of FIFO is shown in Fig. 6.5.

The input and output of the FIFO are associated with electronic systems that write and read the data respectively. When the same clock is used for reading and writing, it is called synchronous FIFO, whereas an asynchronous FIFO uses two different clocks for reading and writing. The status flags like 'EMPTY' and 'FULL' are used for the case of asynchronous FIFO.

For our case, the data collected after the counters are stored in FIFO before transferring to the computer.

6.1.5 Data transfer using Labview

We transfer the count data to the PC via RS232 cable. Since the RS232 involves serial communication transmission of data one bit at a time, it has a relatively slower transmission rate with a maximum transmission rate of 115.2 kbps.

The data are prepared according to the RS232 protocol. The data are split into packets of 8 bits data, each of which is encapsulated by a start bit and a stop bit. The baud rate is used to vary the rate of transmission. we use LABVIEW software for serial data acquisition via RS232. The board uses a ZT3232 transceiver chip and a 9-pin DB9 connector for serial communication.

6.2 Implementation and Performance of the module

We use the DE2-115 FPGA board from ALTERA and the hardware language, VHDL for designing the module. The module features 4 inputs with 15 outputs: 11 coincidences and 4 individual ports. To accommodate all these inputs and outputs, a daughter card is designed is connected to the 40-pin expansion header of DE2-115. The FPGA board along with the daughter card is displayed in Fig. 6.6. To check the performance of the module, we use inputs from a function generator and check all the components of the module individually.

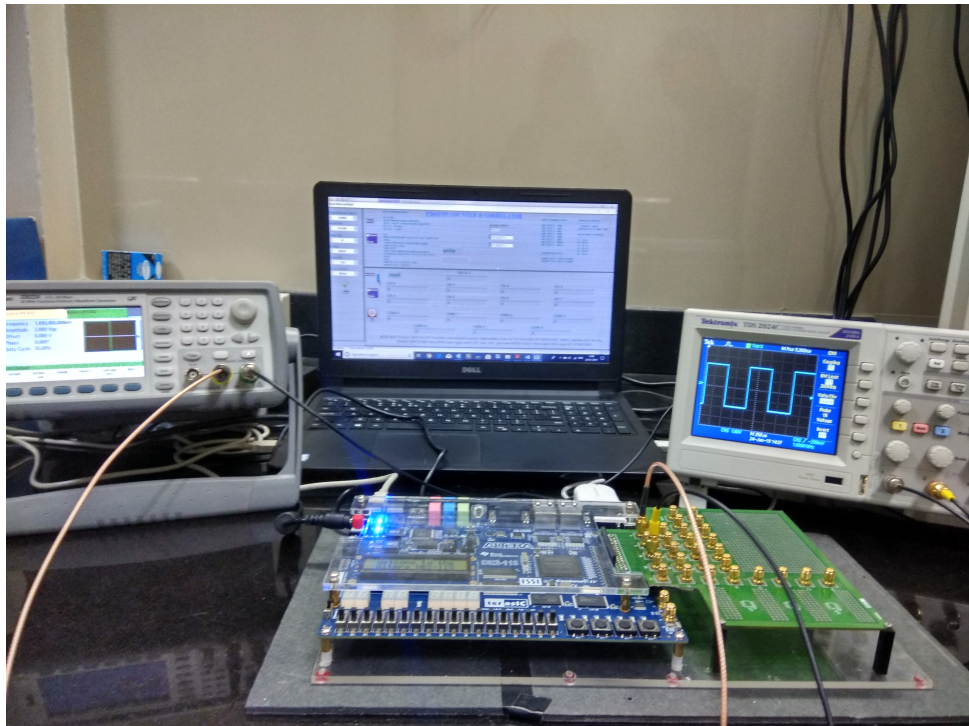


Figure 6.6: Photograph of FPGA board with daughter card

6.2.1 Pulse-shaping

The performance of the pulse shaping circuit is presented in Fig. 6.7. The circuit was tested with a TTL pulse from a function generator. The input pulse presented in Fig. 6.7 (a) is of 100 ns, which has been reduced to 8.2 ns, 17.5 ns, and 45 ns presented in Fig. 6.7 (b), (c) and (d) respectively. In this circuit, the minimum width of the output pulse was found to be 8.2 ns, which is the propagation delay of a single gate.

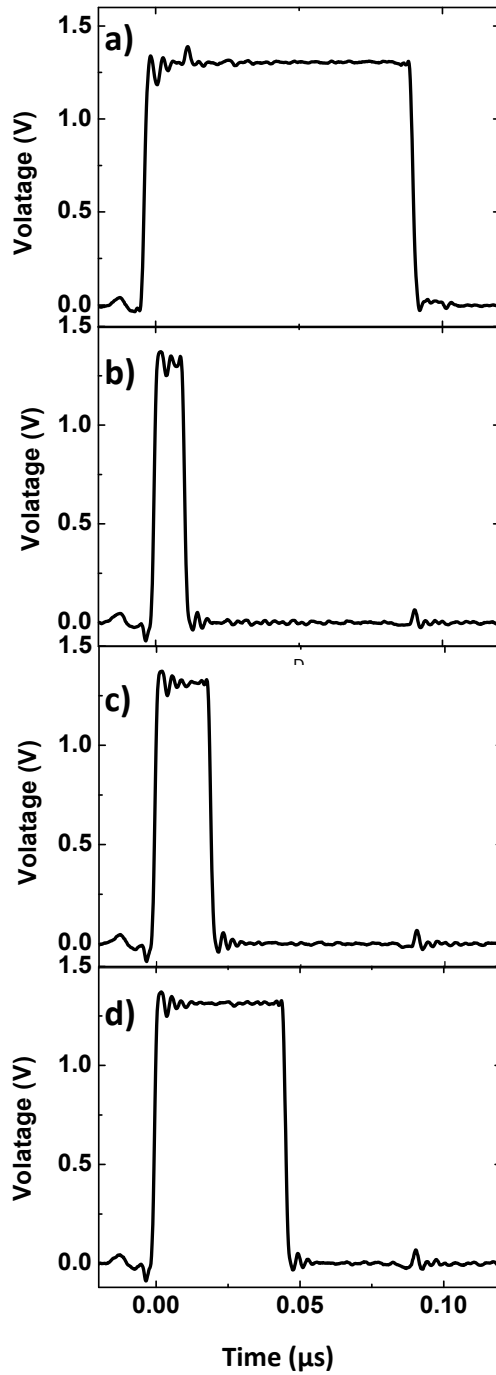


Figure 6.7: a) Input pulse with 100 ns and pulse-shaped output with widths b) 8.2 ns c) 17.5 ns and d) 45 ns respectively.

6.2.2 Periodic and Pseudo-random pulses counting

To verify the performance of the counter module, we use periodic pulses of the same and/or different frequencies to check the individual as well as coincidence counting. Fig. 6.8 represents the screenshot of the Labview program displaying the count data. This is for the case of two input channels with pulse widths 0.2 ns and 0.1992 ns. The corresponding T_{cycle} and T_{exp} are given as $20\mu\text{s}$ and 1ms respectively.

We also use a wave-form with variable width from a function generator as input to the counting module. After pulse-shaping, it serves as a pseudo-random pulse. We take two such pulses and observed the individual counting as well as the random coincidence counting as a verification of the module.

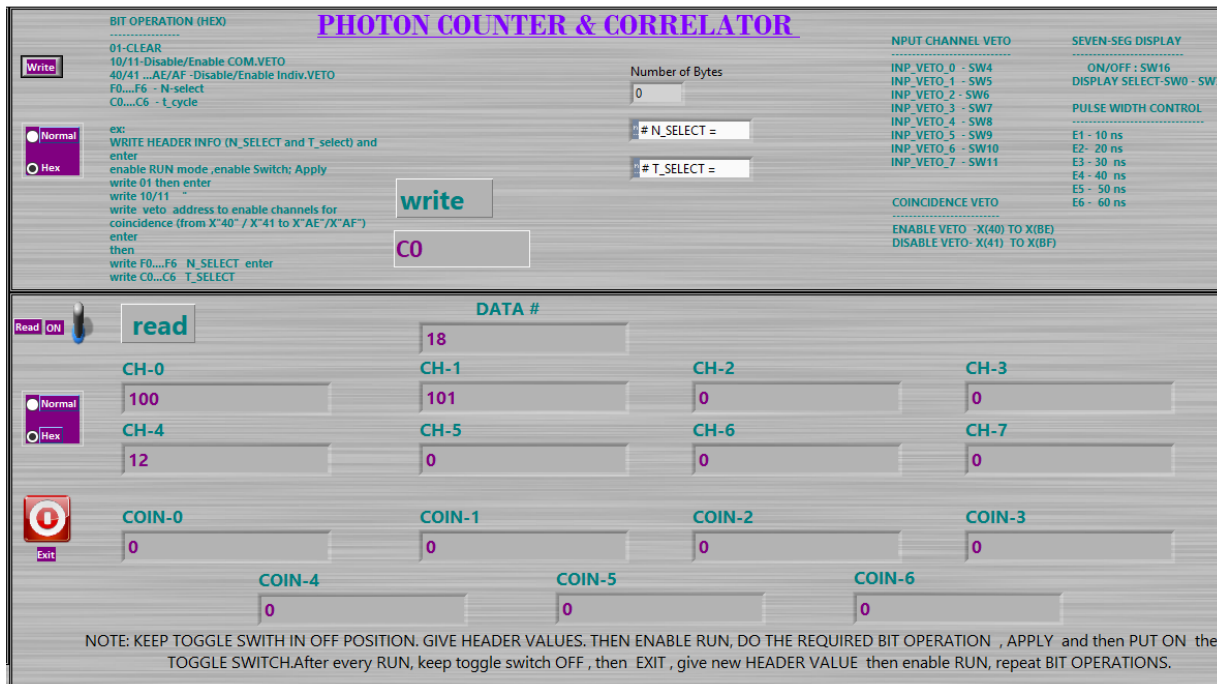


Figure 6.8: Screen shot of the Labview display showing counting and coincidence in different channels

Bibliography

- [1] Jian-Wei Pan, Zeng-Bing Chen, Chao-Yang Lu, Harald Weinfurter, Anton Zeilinger, and Marek Zukowski, *Rev. Mod. Phys.* **84**, 777 (2012).
- [2] L. Mandel, *Rev. Mod. Phys.* **71**, S274 (1999).
- [3] V. A. Pedroni, *Circuit design with VHDL*.
- [4] D. Branning, S. Khanal, Y. H. Shin, B. Clary, and M. Beck, *Rev. of Sci. Inst.* **82**, 016102 (2011).

Chapter 7

Future perspectives

With a Zeeman degenerate two-level atomic system, we have demonstrated polarisation rotation of an elliptically polarised light due to efficient FWM and XPM. The same system can be used to generate a squeezed vacuum state when the vacuum fluctuation in one polarization direction plays the role of the probe beam. This experiment necessitates the ideal filtering of the strong pump beam after the cell. With the current facilities i.e. using a Glan-Thompson polariser of extinction ratio 5000:1, the leakage from the input pump beam of 8-10 mW would be $\sim 2 \mu\text{W}$ in the orthogonal polarization direction. Whereas, the optical power in the single photon regime, would be $\sim 1 \text{ pW}$ with a photon flux of 10^6 s^{-1} for a laser beam of wavelength 780 nm. Therefore, the leakage from the pump requires to be minimized to perform the experiment at the few photon level. The future plan is to apply different filtering techniques to filter out the pump beam for the experiment to generate a vacuum squeezed state of light. One way is to use the polarisation-directed flat lenses in the path of the output light after the cell. These special types of lenses create different focal lengths depending on the polarisation state of the light. In this way, the pump beam can be defocused while the light in the orthogonal direction will be focused. Spatial filtering consisting of an aperture can be used to filter out the pump beam.

The future direction of this research also heads towards a better understanding of the phase transition due to optical bistability in the threshold of the MOPO. The critical exponent of the phase-transition as measured under various experimental parameters is found to be different from that measured for the bistability observed in similar systems. It is necessary to understand the origin of the inconsistency of the system with theoretical evidence to verify the value of the critical exponent associated with the system.

We have also observed optical bistability in the transverse modes of MOPO in our system. It

means that the threshold power for the generation of Laguerre-Gaussian mode in the increasing pump power direction is more than that in the decreasing pump power direction. Understanding this effect comes under the future plan of the research. Furthermore, it would be interesting to study the mechanism of the transition from single-mode to the multimode regime of the MOPO in detail. Another future perspective of the work is to induce various potential in the nonlinear refractive index experienced by the generated fields by using different intensity profile of the pump or control fields such as the random intensity pattern. The FPGA-based photon counting/correlator module can also be used to study the correlated photons generated via MOPO in the few-photon regime. It would be very interesting to study the transverse correlation of the generated biphotons via MOPO.

Appendix A

Fundamental Physical Constants

| Quantity | Symbol | Value |
|------------------------------|--------------|--|
| Speed of light in free space | c | $2.998 \times 10^8 \text{ m s}^{-1}$ |
| Permeability of free space | μ_0 | $4\pi \times 10^{-7} \text{ H m}^{-1}$ |
| Permittivity of free space | ϵ_0 | $8.854 \times 10^{-12} \text{ F m}^{-1}$ |
| Planck's constant | h | $6.626 \times 10^{-34} \text{ J s}$ |
| Boltzmann's constant | k_B | $1.381 \times 10^{-23} \text{ J K}^{-1}$ |
| Elementary charge | e | $1.602 \times 10^{-19} \text{ C}$ |
| Bohr magneton | μ_B | $9.274 \times 10^{-23} \text{ A m}^2$ |
| Electron mass | m_e | $9.109 \times 10^{-31} \text{ K g}$ |

Table A1: Fundamental physical constants. Adapted from:
<https://physics.nist.gov/cuu/Constants>

| Quantity | Symbol | Value |
|--|--|---|
| Atomic Number | Z | 37 |
| Relative Natural Abundance | $\eta(^{85}\text{Rb})$ | 72.17% |
| Atomic Mass | m | $1.41 \times 10^{-25} \text{ Kg}$ |
| Nuclear Spin | I | 5/2 |
| Vapor pressure at 25 ⁰ C | P_V | $3.92 \times 10^{-7} \text{ Torr}$ |
| Electron spin g-factor | g_S | 2.002319 |
| Electron orbital g-factor | g_L | 0.999993 |
| Fine structure Lange g-factor | $g_J(5^2S_{1/2})$ | 2.00233 |
| Nuclear g-factor | g_I | -0.000294 |
| D2 ($5^2S_{1/2} \rightarrow 5^2P_{3/2}$) wavelength (Vacuum) | λ | 780.2414 nm |
| D2 life time | τ | 26.63 ns |
| D2 line natural Line Width (FWHM) | Γ | $2\pi \times 6.07 \text{ MHz}$ |
| D2 line transition Dipole Matrix Element | $\langle J = 1/2 \hat{\mu} J' = 3/2 \rangle$ | $3.58 \times 10^{-29} \text{ C} \cdot \text{m}$ |
| Saturation Intensity (F=3 \rightarrow F'=4) | I_{sat} | 3.89 mW/cm ² |

Table A2: Properties of ⁸⁵Rb. Adapted from: Steck, D. A.
Rubidium 85 d line data, <http://steck.us/alkalidata>

Appendix B

Rubidium cell housing

All the experiments are performed with a 50 mm length anti-reflection coated vapor cell with Rubidium in its natural abundance (Triad Technologies). A schematic of the cell housing is shown in Fig B1. We use two resistive heaters attached to the two interfaces of the cell, which are connected in series to a temperature controller. The controller maintains a stable temperature inside the cell using its PID system and is recorded by a thermistor attached to one face of the cell. With the present configuration, we could heat the cell up to 125°C corresponding to a number density of 10^{13} cm^{-3} . The temperatures used for all the experiments in the thesis are in the range of 95°C - 115°C as measured through the temperature controller. The vapor cell is enclosed with three layers of cylindrical μ -metal in order to shield the stray magnetic field noise. However, the open faces of the μ -metal cylinder can't shield the magnetic field in the axial direction. Hence, a solenoid with 4000 turns/m is used to compensate for the axial magnetic field, which is found to be $\simeq 10\text{ mG}$.

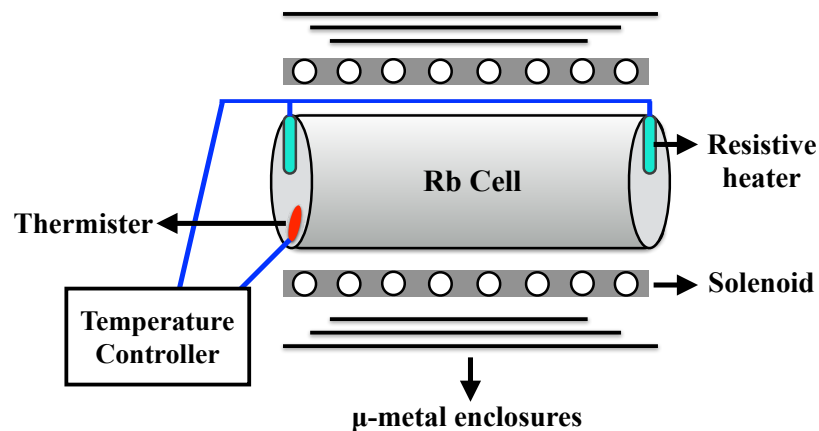


Figure B1: Schematic of Rubidium cell housing.